

Improvement of spectral response using tandem structured dye-sensitized solar cells

Jeongmin Lim

Department of Chemical Engineering

Graduate School of UNIST

2014

Improvement of spectral response using tandem structured dye-sensitized solar cells

Jeongmin Lim

Department of Chemical Engineering

Graduate School of UNIST

2014

Improvement of spectral response using tandem structured dye-sensitized solar cells

A dissertation

submitted to the Graduate School of UNIST

in partial fulfillment of the

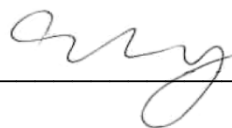
requirements for the degree of

Doctor of Philosophy

Jeongmin Lim

07.07. 2014 of submission

Approved by



Advisor

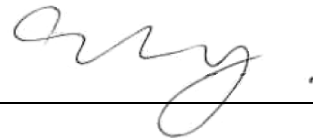
Sung You Hong

Improvement of spectral response using tandem structured dye-sensitized solar cells

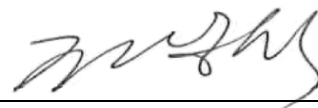
Jeongmin Lim

This certifies that the dissertation of Jeongmin Lim is approved

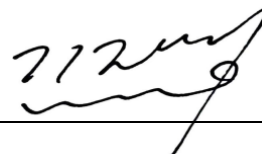
07. 07. 2014 of submission



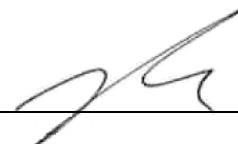
Advisor: Sung You Hong



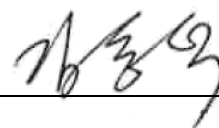
Yongseok Jun: Thesis Committee Member #1



Jin Young Kim: Thesis Committee Member #2



Tae-Hyuk Kwon: Thesis Committee Member #3



Dongsuk Kim: Thesis Committee Member #4

Abstract

Dye-sensitized solar cells (DSSCs) have attracted great attention and one of the strong alternatives to conventional Si-based solar cells because of their advantages such as transparency, comparable efficiency, various colors, and simple processes with low costs, etc. In order to get high solar-to-electrical conversion efficiency, improved the spectral response of the sensitizer is necessary. At the principals of DSSCs, the dye molecules act as a primary active component for the absorption of the solar spectrum and generating electrons. If the dye molecules should absorb the sun's spectrum as wide as possible, the number of generated electrons should be increased and higher conversion efficiency can be achieved with increased spectral response. However, the individual sensitizer can only absorb its own particular range of wavelength. To maximize energy harvesting of DSSCs, many researchers approaching to make a panchromatic system, which could absorb the photons over the entire range of wavelength. Here, I present the prominent way to fabricating panchromatic structured dye-sensitized solar cells. In order to fabricate working electrodes, newly method of pre-dye coating (PDC) of TiO₂ nanoparticles (NPs) and an approach of a dip coating have been adopted for the panchromatic DSSCs. A bi-layer photoanode with two distinct TiO₂ layer, which were individually sensitized with N719 and N749 dyes were coated on a transparent conducting oxide (TCO) in a sequenced manner. The improvement of spectral response and efficiency of panchromatic DSSCs has been checked with the absorption characteristics of each dye. Furthermore, by using intensity modulated photovoltaic spectroscopy (IMVS), I could check the dynamic electron kinetic and calculate lifetime in ambient conditions with $\tau_n = 1/(2\pi f_{\min}(\text{IMVS}))$. In addition, here I report a novel structure of DSSCs with reversely form by constructing all the components together as one substrate. With this new structure, comparable cell properties was achieved to the conventional structure. The electrochemical properties and photochemical properties were checked by electrochemical impedance spectroscopy. Moreover, the present approach could be an encouraging new direction in research while facilitating the fabrication of hybrid-tandem solar cells. Furthermore, I also present a systematic approach of carbon black in order to optimize the catalytic ability of iodide/tri-iodide electrolyte. Replacement of the Pt counter electrode with an inexpensive but electro-chemically stable alternative is one key technological challenge that must be overcome to make DSSCs more economical. Based on the electrochemical analysis, the charge-transfer resistance and photo-electrochemical properties were characterized.

Keywords: Dye-sensitized solar cells, panchromatic structure, dip-coating process, reversely fabricated structure.

Table of Contents

Abstract	i
Table of Contents	ii
List of Figures	v
List of Tables	ix
Chapter 1. Introduction	1
1.1 History of dye-sensitized solar cells (DSSCs)	1
1.2 Overview of DSSCs.....	1
1.2.1 Structure of DSSCs.....	1
1.2.2 Principles of DSSCs	5
Chapter 2. Characterization and modeling of dye-sensitized solar cells	11
2.1 Characterization of dye-sensitized solar cells (DSSCs)	11
2.1.1 Efficient measurement with J-V curve	11
2.1.2 Incident photon to current conversion efficiency (IPCE)	12
2.1.3 Electrochemical method: CV, EIS	13
2.2 Development of DSSCs.....	15
2.2.1 Improvement of spectral response.....	16
2.2.2 Cost-effective counter electrodes	21
Chapter 3. Fabrication of panchromatic dye-sensitized solar cells using pre-dye coated TiO₂ nanoparticles by a simple dip coating technique	24
3.1 Research overview	24
3.2 Background and introduction	25
3.3 Experimental.....	26
3.4 Result and discussion.....	28
3.5 Conclusion	34
Chapter 4. Reversely fabricated dye-sensitized solar cells	36
4.1 Research overview	36

4.2 Background and introduction	36
4.3 Experimental.....	37
4.4 Result and discussion.....	39
4.5 Conclusion	53
Chapter 5. A study of TiO₂/carbon black composition as counter electrode materials for dye-sensitized solar cells.....	54
5.1 Background and introduction	54
5.2 Experimental.....	55
5.3 Result and discussion.....	56
5.4 Conclusion	62
Chapter 6. Cost-effective counter electrode of dye-sensitized solar cells with carbon-coated silicon nanowires	64
6.1 Background and introduction	64
6.2 Experimental.....	64
6.3 Result and discussion.....	66
6.4 Conclusion	73
Chapter 7. Quasi-solid state electrolytes with silica nanomaterial for high efficiency dye-sensitized solar cells	75
7.1 Background and introduction	75
7.2 Result and discussion.....	75
7.3 Conclusion	80
Chapter 8. Polymer hole transport materials for recombination in perovskite sensitizer solar cell	81
8.1 Research overview	81
8.2 Background and introduction.....	81
8.3 Experimental	82
8.4 Result and discussion	83
8.5 Conclusion.....	90
Chapter 9. Summary	91

Chapter 10. References..... 92

Acknowledgement..... 109

List of Figures

Figure 1.1 Schematic of the typical structure of dye-sensitized solar cells.

Figure 1.2 The crystal structures of (a) tetragonal rutile, (b) tetragonal anatase, and (c) orthorhombic brookite. (white sphere : Ti, red dot : O).

Figure 1.3 Integration of transparent semiconductor materials architecture into DSSCs with (a) nanotube, (b) nanorod (nanowire), and (c) nanobranched.

Figure 1.4 An energetic scheme of electron transfer processes taking place after charge injection from.

Figure 1.5 Schematic illustration of kinetics in the DSSCs with electron dynamic time scales.

Figure 2.1.1 Photocurrent-voltage curve with short/open points (V_{oc} , I_{sc}) and max points (V_{max} , I_{max}) of solar cells.

Figure 2.1.2 The quantum efficiency of a conventional silicon solar cell.

Figure 2.1.3 An equivalent circuit of the DSSCs.

Figure 2.1.4 Nyquist plot of conventional DSSC.

Figure 2.1.5 Bode plot of conventional DSSC.

Figure 2.2.1 IPCE spectra of various type of solar cells.

Figure 2.2.2 Schematic structure of series- connected tandem DSSC (a), $I-V$ curves for the best performance of tandem DSSC and individual cells (b), and IPCE spectra of the tandem DSSC and individual cell.

Figure 2.2.3 Structure of dyes used in previous work by other groups. B1 (a), G2 (b), G6 (c), G7 (d), R4 (e), and R5 (f).

Figure 2.2.4 Schematic of a bilayered working electrode with low transfer method (a), Schematic representation and reaction scheme of the bi-layered working electrode fabrication process (b), Schematic representation of a multilayered working electrode prepared via sintering followed by the transfer method (c), and Schematic representation of a double dye layer sensitized electrode prepared by the stamping method with mixed dye-sensitized electrode prepared by the cocktail method (d).

Figure 2.2.5 Chemical structure of conducting polymers as alternative cathodes in DSSC (a) PEDOT, (b) PANI, (c) PProDOT, and (d) PPy.

Figure 3.1 A schematic preparation of the panchromatic electrode using the pre-dye coating method.

Figure 3.2 SEM images of TiO₂ layer made by the pre-dye coated method. The inset is the cross section view of the electrode.

Figure 3.3 Photocurrent-voltage curves of the pre-dye coated samples. Single N719 (blue, squares), single N749 (green, dots), and panchromatic (brown, triangles) cells.

Figure 3.4 Incident photon to current conversion efficiency of the pre-dye coated samples. N719 single cell (blue, squares), N749 single cell (green, dots) and panchromatic cell (brown, triangles).

Figure 3.5 Intensity modulated photovoltaic spectroscopy of the pre-pressed cell (black, squares) and PDC TiO₂ NPs cell (red, dots).

Figure 3.6 Long term stabilities of panchromatic PDC TiO₂ NPs sample. (a) Efficiency, FF change curves and (b) J_{sc} , V_{oc} change curves.

Figure 3.7 A schematic preparation of the triple layered panchromatic electrode using the pre-dye coating method.

Figure 4.1 Schematic diagrams of conventional and reversed structure of dye-sensitized solar cells.

Figure 4.2 Thermogravimetric analysis (TGA) curve of supporting layer with PVA binder.

Figure 4.3 (a) Surface morphology of supporting layer using scanning electron microscopy, (b) photocurrent-voltage curve of the reverse structured cell with ZrO₂, and (c) electrochemical impedance spectroscopy (EIS) of symmetric cell.

Figure 4.4 SEM images of synthesized BaSnO₃ with (a) sphere, (b) nanorod, and (c) nanopillar. (d) Picture of BaSnO₃ paste for supporting layer. The paste were mixed (a), (b), and (c) with wt% of 50, 1, and 1 respectively.

Figure 4.5 photocurrent-voltage curve of the reverse structured cell with BaSnO₃.

Figure 4.6 Schematic diagram of the fabrication process of AAO templates.

Figure 4.7 a and b represents the morphology of the AAO surface by scanning electron microscopy. c, d, and e show the pictures of AAO film and its application to the DSSC with TiO₂ photoanode.

Figure 4.8 photocurrent-voltage curve of the reverse structured cell with anodic aluminum oxide (AAO).

Figure 4.9 Field emission scanning electron microscopy (FE-SEM) images of supporting layer with sintering temperature of (a) 450°C and (b) 500°C.

Figure 4.10 Cross-section FE-SEM images of reversed structure of dye-sensitized solar cell.

Figure 4.11 Surface profilometer measurement of RS-DSSC.

Figure 4.12 Photocurrent-voltage curve of the reverse structured cell.

Figure 4.13 (a) Nyquist plot and (b) Bode phase plot of the electrochemical impedance spectroscopy of reverse structured DSSC. The equivalent circuit of the device is shown in the inset of (a).

Figure 4.14 Schematic structure of the series connected tandem solar cell (a) and picture of the cell (b).

Figure 4.15 Photocurrent-voltage curves of the inverted OSC (single cell, blue triangle), RS-DSSC (single cell, red circle), and series tandem cell (black square).

Figure 5.1 X-ray diffraction (XRD) patterns of synthesized TiO₂ particles. Autoclave temperature of (a) 200 °C, (b) 220°C, and (c) 240 °C.

Figure 5.2 FE-SEM image of the (a) carbon black powder and (b) hydrothermally synthesized TiO₂ nanoparticles.

Figure 5.3 TGA in air and argon with the carbon black at a heating rate of 10°C/min.

Figure 5.4 Photocurrent-voltage curves of the devices.

Figure 5.5 Nyquist plot of Pt reference cell and four different ratios of T/CB symmetrical cells.

Figure 5.6 Cyclic voltammograms of Pt reference cell and optimized T/CB cell.

Scheme 6.1 Schematic diagram of silicon nanowire fabrication and carbon shell deposition.

Figure 6.1 SEM images of vertically aligned as-prepared silicon nanowire array (a), tilted silicon nanowires (b), and carbon coated-silicon nanowires (c).

Figure 6.2 Low magnification TEM image of a single carbon coated-silicon nanowire (a), HRTEM images of carbon shells deposited on silicon nanowire surface under different reaction times: 1, 3, 5, 7, and 11 min, respectively (b-f). The interdistance of the carbon shell is about 0.34 nm.

Figure 6.3 (a) Cross sectional compositional line profile of carbon coated-silicon nanowire in STEM and (b) Raman spectra of the carbon coated-silicon nanowires obtained under different reaction times.

D and G peaks of the carbon shells were plotted with respect to the silicon peak (inset).

Figure 6.4 Nyquist plot of the electrochemical impedance spectroscopy with symmetrical counter electrodes (a) and zoomed view of Nyquist plot with well performed counter electrodes.

Figure 6.5 Cyclic voltammogram of symmetrical cell with Pt coated and carbon deposited silicon nanowire counter electrodes; scan rate 100mV/s.

Figure 6.6 Photocurrent-voltage curves of the devices.

Figure 7.1 Scheme of synthetic route for silica nanomaterials (a) and process table (b).

Figure 7.2 Liquid electrolyte and silica-added gel type electrolytes.

Figure 7.3 Photocurrent-voltage curves of the liquid electrolyte and silica electrolytes.

Figure 8.1 (a) X-ray diffraction of $\text{CH}_3\text{NH}_3\text{PbI}_3$ perovskite materials prepared as powder form and inset shows tetragonal structure of materials. (b) UV-visible spectrum prepared from γ -butyrolactone (GBL) and dimethylformamide (DMF).

Figure 8.2 Molecular structure of hole conductor materials of (a) spiro-OMeTAD, (b) P3HT, and (c) PTB7. (d) Energy diagram of materials which was used in this study.

Figure 8.3 (a) Schematic of energy alignment of the different components. (b) Structure of the device architecture and (c) SEM image of the architecture.

Figure 8.4 Photocurrent-voltage curves of the without HTM sample (black, circle), spiro-OMeTAD sample (red, circle), P3HT sample (blue, triangle), and PTB7 sample (cyan, triangle).

Figure 8.5 Incident photon to current conversion efficiency (IPCE) of the perovskite solar cells. Perovskite with spiro-OMeTAD (black, square), and perovskite with PTB7 (red, circle).

List of Tables

Table 2.2.1 Performances and references with various conductive material counter electrode.

Table 3.1 Photovoltaic performance of the single cells and the panchromatic cell.

Table 4.1 Current-voltage parameters with electrochemical parameters of reverse structured cell using ZrO₂ supporting layer.

Table 4.2 Photovoltaic performance of the RS-DSSC using BaSnO₃ supporting layer.

Table 4.3 Photovoltaic performance of the RS-DSSC using anodic aluminum oxide (AAO) supporting layer.

Table 4.4 Electrochemical impedance parameters of reverse structured cell.

Table 4.5 Photovoltaic performances of the single cells and series connected tandem cell.

Table 5.1 Synthesized TiO₂ size difference between autoclaving temperature with 200°C, 220 °C, and 240 °C.

Table 5.2 Photovoltaic performance of Pt and TiO₂/carbon black composites as counter electrode.

Table 6.1 Peak position of the G and D bands and their I_D/I_G Ratios.

Table 6.2 Photovoltaic performance of the Pt and carbon deposited silicon nanowire counter electrodes.

Table 7.1 Silane reagent with their chemical structure.

Table 7.2 Photovoltaic performance of the liquid electrolyte and silica electrolytes.

Table 8.1 The levels of HOMO, LUMO, and hole mobility of HTM materials.

Table 8.2 Photovoltaic performance of the cells with various HTM.

Chapter 1. Introduction

1.1 History of dye-sensitized solar cells (DSSCs)

A solar cell is a photonic device that converts photons with specific wavelengths to electricity. After Becquerel discovered the photo-electrochemical (photovoltaic) effect in 1839,^{1,2} the scientific interest as well as the commercial potential led to increased research into photovoltaic and related subjects. In the early of 1970s, after the oil crisis, a tremendous effort was devoted to the development of photovoltaic cells and on the 1980s, the industry began to grown-up, as emphasis on manufacturing and cost grew. Therefore, manufacturing facilities for producing photovoltaic modules from silicon-based p-n junction solar cells were built in many countries.

The history of dye-sensitized solar cells (DSSCs) began in 1972 by Memming.³ In the following years, Matsumura et al. observed photovoltaic properties by using ZnO and natural dyes.⁴ However, the photovoltaic properties and conversion efficiency were too poor with unmodified materials and/or structure. Innovatively, the research by O'Regan and Gratzel in 1991 spurred researchers to take on the challenge.⁵ With the development of the DSSCs, conventional solid-state photovoltaic technologies are now challenging with devices at a molecular and nano-level. The prospect of low-cost and easy fabrication method could be key features. DSSCs show relatively better efficiency with other solar cell technologies under diffuse light and at high temperatures. Moreover, it offers the possibilities to make solar cells with a large flexibility in shape, color, and transparency.

1.2 Overview of DSSCs

1.2.1 Structure of DSSCs

Solar cells, which is a device that generates electricity form sun light. The main parts of single junction dye-sensitized solar cells are shown in figure 1.1. The cell involves a set of different layers of components, namely, the transparent conducting oxide (TCO) coated electrodes, nanostructured wide band-gap semiconductor, the dye molecules as photosensitizer, and the electrolytes with redox mediator.

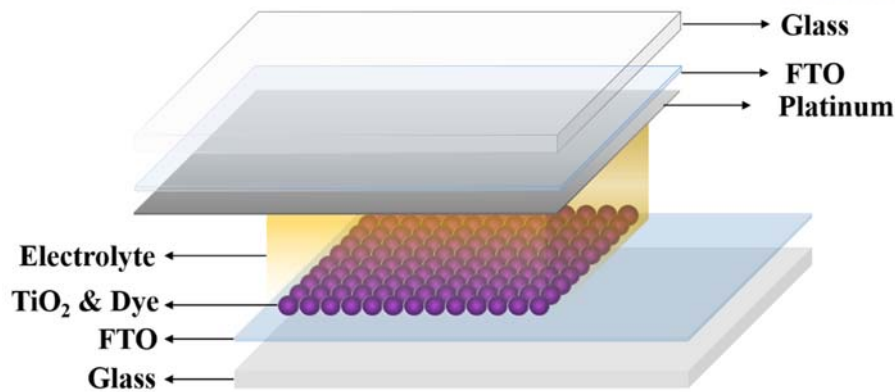


Figure 1.1 Schematic of the typical structure of dye-sensitized solar cells

Transparent conducting glass

For the substrate of DSSCs, clean glass are commonly used due to its high optical transparency in the visible and near infrared region for the penetration of sunlight. For the conductive layer, commonly fluorine-doped tin oxide (FTO) is deposited onto the substrate because of their high conductivity and thermal stability.

Nanostructured wide band gap semiconductor

Until Gratzel group employs porous TiO₂ as the nanoporous materials, DSSCs have shown less than 1% efficiency. After employed the porous material, the wide band gap semiconductors such as TiO₂, or ZnO₂ were widely used owing to their high chemical stability with high resistance to corrosion, structure stability under solar irradiation, and low cost. Furthermore, it can be easily synthesized as nanoparticle shape with various size. In general, TiO₂ is widely used for the working electrode for DSSCs. The three different crystalline structure of TiO₂ such as anatase, rutile and brookite structure have their own electrical properties (see figure 1.2). Among these, rutile and anatase crystalline structure were considered as semiconducting materials with their tetragonal structure. Even though the both anatase and rutile have tetragonal structure, they has different distortion value with different contact method. Furthermore, the anatase has octahedron structure that share four edges forming the four-fold axis. For this reason, these different form of TiO₂ has different electrical properties and porosity. Park et al. reported that the anatase TiO₂ material can adsorbs more photo sensitizer molecules, and shows higher electron mobility than rutile form because of the packing density.^{2, 6-9}

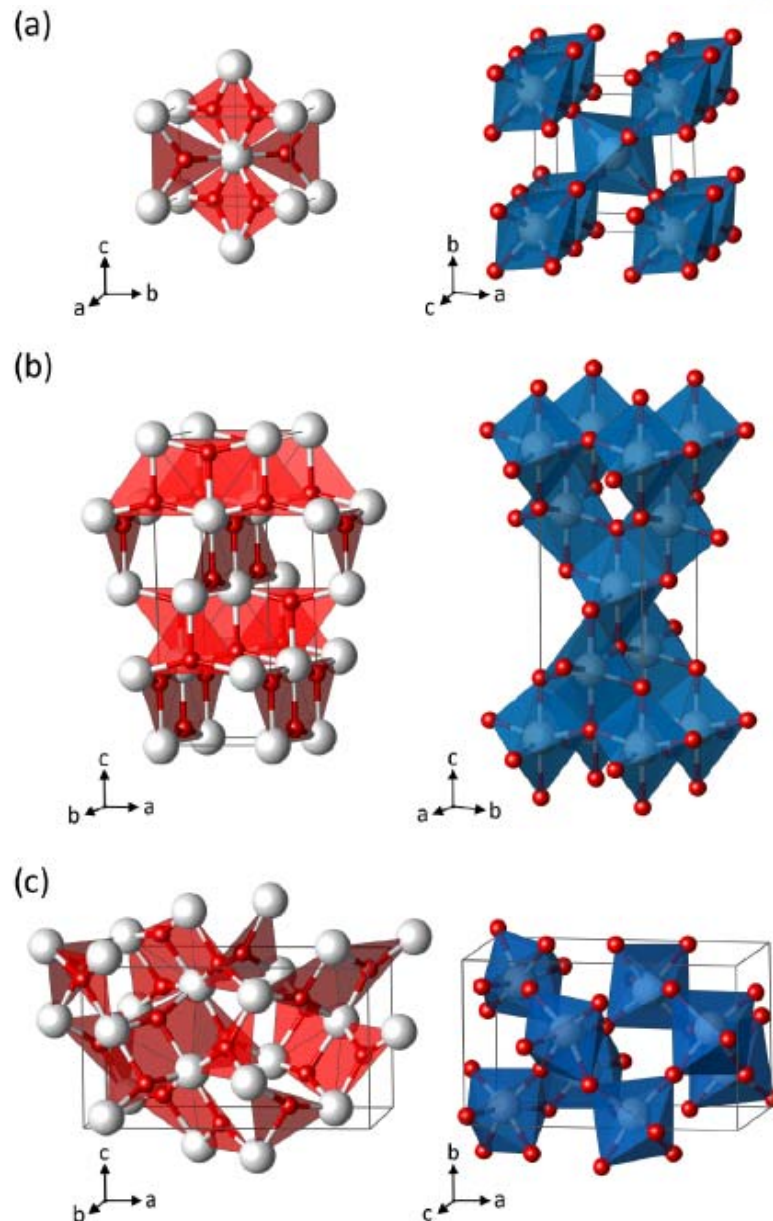


Figure 1.2 The crystal structures of (a) tetragonal rutile, (b) tetragonal anatase, and (c) orthorhombic brookite. (white sphere : Ti, red dot : O)¹⁰

Moreover, these candidate materials can be modified and also to be tuned from nanoparticles to nanotube,¹¹⁻¹⁵ nanorod/wire,¹⁶⁻²⁰ and nanobranched.²¹⁻²³ Figure 1.3 illustrates the DSSCs geometry in various structures of semiconductor.

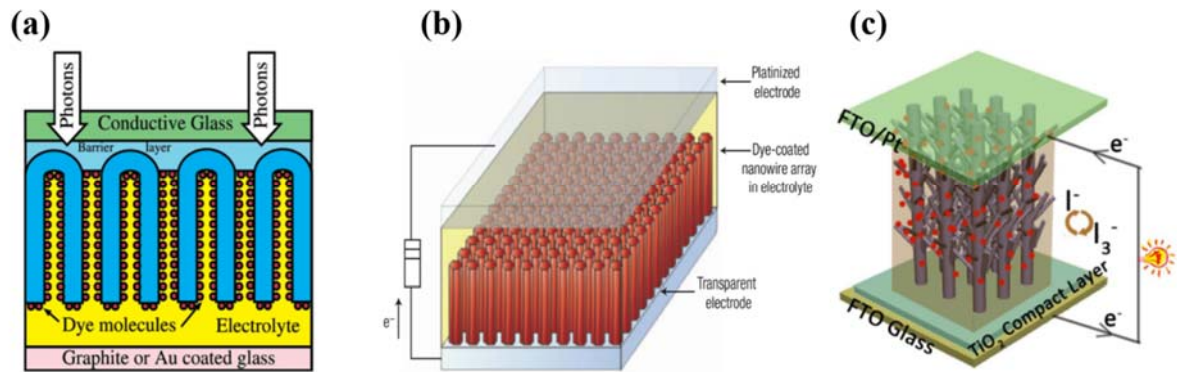


Figure 1.3 Integration of transparent semiconductor materials architecture into DSSCs with (a) nanotube, (b) nanorod (nanowire), and (c) nanobranch. Reproduced in part with permission from ref.¹² 16, 22

Photosensitizer

Dye molecules with proper molecular structure are used as photosensitizer of DSSCs. Dye molecule were adsorbed on the surface of nanostructured semiconductor such as TiO_2 or ZnO_2 and generating electrons by absorbing photons. To harvest solar light efficiently, a lot of ruthenium complexes and organic dyes have been designed and synthesized for light absorber.²⁴⁻³² Dye molecules, which is involves transition metal coordinated compounds (e.g., ruthenium complex) is most widely used because of visible absorption, excitation lifetime and efficient charge transfer. Not only transition metal complex, organic dyes which include natural pigments and synthetic organic dyes have a donor-acceptor structure called as push-pull architecture.

Redox electrolyte

To introduce the electrolyte into the system, two electrodes was subsequently placed. At the middle of two electrodes, room for electrolytes were filled with redox mediator and completing the electric circuit containing I^-/I_3^- redox ions. The redox mediator could get the electrons from counter electrode and regenerate the oxidized dye molecules. The redox mediator moved by diffusion, cell performance is highly affected by ion conductivity in the electrolyte which is directly affected by the viscosity of the solvent. The 3I^- gives 2 electrons to the oxidized sensitizer and the I_3^- moves to the counter electrode. I_3^- regains electrons from the counter electrode and it turned to 3I^- ions. By this continues reaction, full circuit of the electrochemical photovoltaic cell was completed.

Counter electrode

For the counter electrode, thin layer of platinum coated FTO glass substrate was widely used due to its catalytic properties and stabilities. On the back of the DSSCs there presents Pt coated counter electrode as a catalyst to regenerate I⁻ and as the cathode. However, there are researches reporting that Pt corrodes in an electrolyte containing iodide to generate PtI₄ slowly.^{33, 34} Besides, considering high expenses, a great deal of effort has been taken to develop alternative materials for counter electrodes.

1.2.2 Principles of DSSCs

Overview of the processes

In dye-sensitized solar cells (DSSCs), dynamics of interfacial and surface electron transfer is based on the ultrafast electron injection from molecular excited state into the conduction band of a semiconductor. Consequently, produced dye cations have to be intercepted prior to recombination with electrons of conduction band. This charge transfer between the oxidized dye at the surface of semiconductor and the hole transport mediator establishes the photon-to-current conversion efficiency. As a result, electron percolation among semiconductor nanoparticles, as well as hole transport within the pore to the cathode, has to get sufficient rate to prevent indirect recombination. A schematic of the photo-physical electron transfer processes taking place at the semiconductor/dye/electrolyte interface for state-of-the-art DSSCs are summarized in figure 1.4 and equation 1.1.

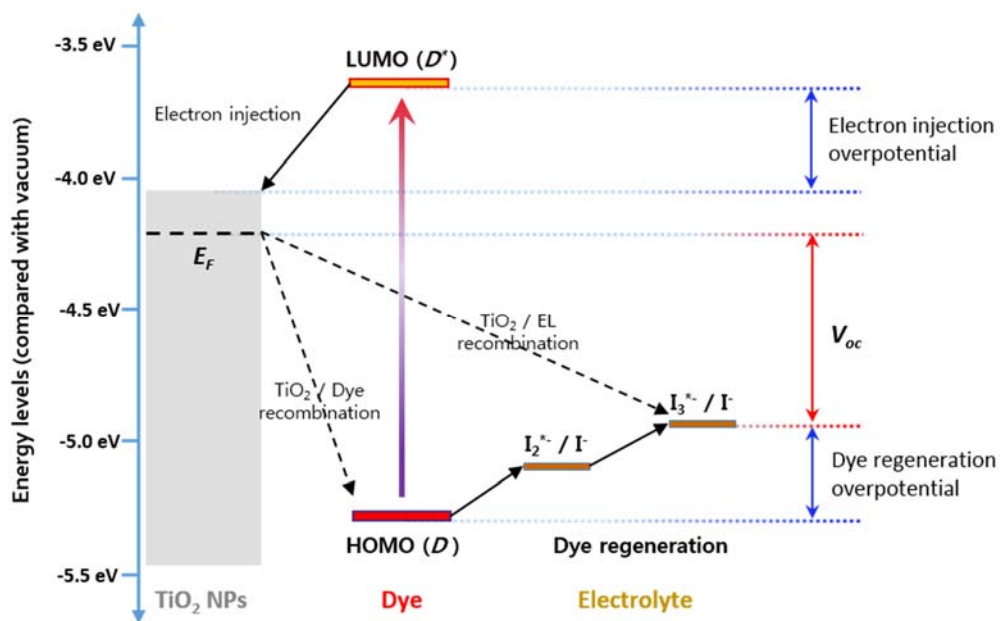
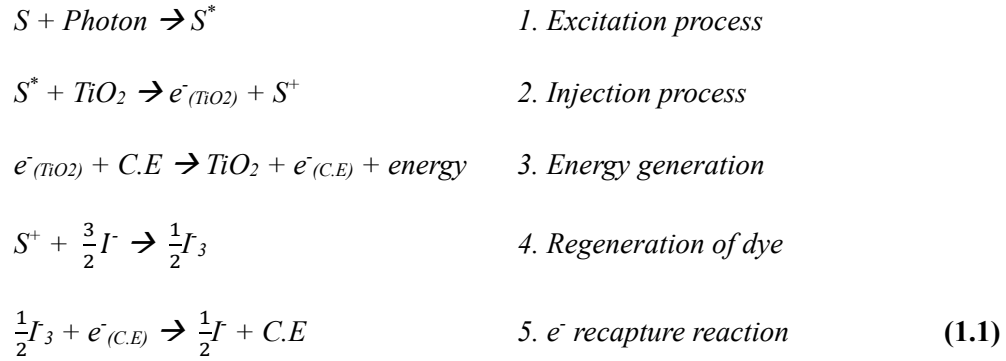


Figure 1.4 An energetic scheme of electron transfer processes taking place after charge injection from an excited state S^* to the TiO_2 nanoparticles. Recombination processes are indicated by dashed arrow.



$$\varphi_{inj} = \frac{k_{inj}}{k_{inj} + k_1} \tag{1.2}$$

DSSCs are characterized by excited state lifetimes typically in the range of $\tau = 10\sim 100$ ps. Although the detailed mechanism of the injection process is still under debate, it is widely accepted that an efficient charge injection should take place within a sub-picosecond time frame. The lifetime of excited state of Ru complexes dye are usually longer lived with $\tau = 10\sim 100$ ns. The electron injection efficiency can be determined by equation 1.2. The rate constants for electron injection (k_{inj}) and decay (k_1) were used for the equation. For efficient injection, k_{inj} should be about 100times much larger than k_1 . The oxidized dye were intercepted by in the presence of electron donor, normally I^- , typically in the μs time domain. Besides, the charge transport mechanism in nanoparticles are still under debate with inherent conductivity, low built-in electrical potential, and a lots of phase boundary with relatively slow diffusion (ms domain) at the interface of TiO_2 , in the bulk of the particles, and/or at grain boundaries can occurred electron traps.

To complete the electrical circuit of DSSCs, Pt coated counter electrode with I_3^-/I^- electrolytes should be used for the reduction of electron acceptors in the electrolyte. At the surface of counter electrode, tri-iodide is reduced to iodide:



Dynamics in DSSCs; Charge injection, transport, and recombination

A benefits of DSSCs are the imitation of natural photo-synthesis in which it separates the light absorption from electron collection processes. In the DSSCs, the driving force for the transport of electrons or ions is the gradient of free energy or electrochemical potential. Consequently, kinetics and the relative positions of the energy levels at the oxide/dye/electrolyte interface are important to understand the electron transfer dynamics in DSSCs.

The configuration of the sensitizer, the energy separation gap and the highly occupied molecular orbital (HOMO) / lowest unoccupied molecular orbital (LUMO) level are greatly affecting the electron flow. Figure 1.5 shows a schematic illustration of kinetics in the DSSCs. Hagfeldt and Gratzel (2000) reported time scales of each components that relaxation of the excited level with 60ns, electron injection from the dye (LUMO level) to the TiO₂ (Conduction band, CB) with 50fs ~ 1.7 ps time scale, recombination of the electrons with the hole on the dye (HOMO level) with ns ~ ms scale, the regeneration of the oxidized dye by electrolytes (I⁻) with 10ns scale, and the recombination of the electrons in the TiO₂ (CB) with a hole in the electrolyte (I₃⁻) with 10ms scale.³⁵

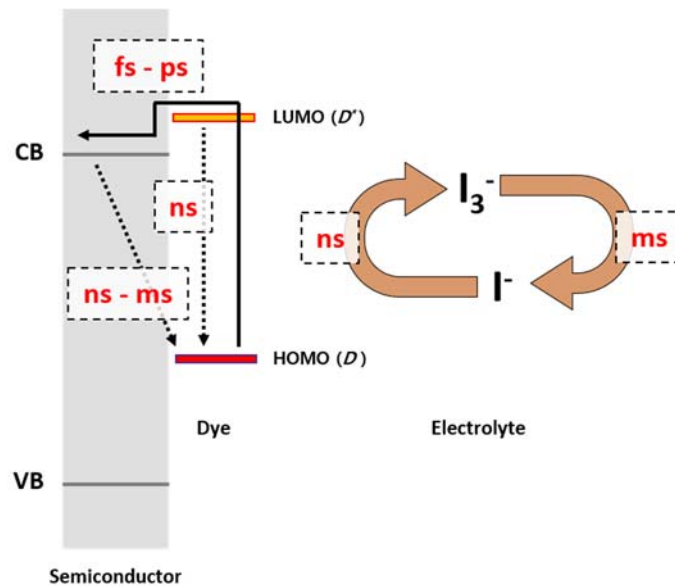


Figure 1.5 Schematic illustration of kinetics in the DSSCs with electron dynamic time scales.

Injected electrons from the photo-excited dye into TiO₂ will go through the interconnected

nanoparticle networks to reach the anode. In TiO₂ nanoparticle, the electrons diffuse to the anode by hopping 103-106 times between particles (Baxter et al., 2006).³⁶ With each hop, there is a considerable probability of recombination of the photo-excited electron with the electrolyte since both the diffusion and recombination rates are on the order of milliseconds. Hence, this allows recombination to limit the cell efficiency. The excess electronic charge of the oxide nanoparticles arising from injected electron (from sensitizer) is balanced by a net ionic charge in the electrolyte. For an efficient DSSCs, the high quantum efficiency for injection is more important. The electron injection efficiency is defined as follows:

$$\varphi_{inj} = \frac{k_{inj}}{k_{inj} + k_1} \quad (1.5)$$

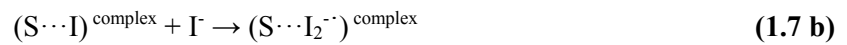
Where φ_{inj} , k_{inj} and k_1 are the electron injection efficiency, rate constant for electron injection and rate constant for electron decay of the photo-excited dye, respectively. In order to get efficient injection, k_{inj} should be about 100 times larger than k_1 for “kinetic redundancy” for the system. The kinetics of electron is related to the performances. If slow down the electron injection of the device by increasing energy of conduction band (E_c), it should lead to an increase of V_{oc} . However, driving force for electron injection (E_{inj}) will be decreased with result in a decreased φ_{inj} and J_{sc} .

The positive ionic charge in the electrolyte is delivered from the regeneration of the dye by electron transfer from iodide ions. Due to the high density of ionic charge in the electrolyte, the excess charges in the oxide nanoparticles can be efficiently blocked and electric fields can be formed. However, the diffusion of electrons is also complicated by trapping and de-trapping method processes influencing the time response.

At open circuit condition under illumination, the total rate of electron transfer to I₃⁻ ions in electrolyte and to oxidized sensitizer must be balanced by the net rate of electron injection. After photo-excited electron injection from the dye into the conduction band of nanoparticles, the dye molecules is in its oxidized state and should be reduced by electrolyte (regeneration). A limit for the regeneration time depends on diffusion limited kinetics. The diffusion rate constant (k_{diff}) in non-viscous electrolyte is in the range of 10⁹ ~ 10¹⁰ m⁻¹s⁻¹. With the k_{diff} , the regeneration efficiency, φ_{reg} , should be considered.

$$\varphi_{reg} = \frac{k_{reg}}{k_{reg} + k_{rec}} \quad (1.6)$$

This equation gives the probability that an oxidized dye can be regenerated by an electrolyte rather than by recombination. The k_{reg} and k_{rec} are the rate constant for regeneration and first oxidized dye recombination respectively. At the DSSCs system, the standard electron donor in electrolyte is iodide. After photo-induced electron injection from the dye to the conduction band of TiO_2 , the oxidized sensitizer (S^+) should be reduced by iodide as follow:

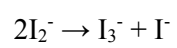


At first, one-electron transfer from I^- to S^+ is occur for reducing the oxidized dye. The oxidation of iodide to free iodine radical bound to the dye, and a $(S \cdots I)$ complex was made. Subsequently, second iodide leads to the formation of a $(S \cdots I_2^{\cdot-})$ complex and dissociate into reduced dye S and $I_2^{\cdot-}$. Finally, two $I_2^{\cdot-}$ turned to triiodide (I_3^-) and iodide (I^-). Suppose, the electron recombination was not occurred, the steady state electron density under illumination at open circuit is determined by the equation 1.8 with v_{inj} and v_{br} are rates for electron injection and for electron recombination with I_3^- respectively.

$$\frac{dn}{dt} = v_{inj} - v_{br} = 0 \quad (1.8)$$

The rate of back reaction (1.3) depends on the concentration of reactant. This back reaction can be explained by several steps. An electron at the surface of counter electrode was captured by I_3^- ions to form the iodine radical ion (1.9a). Subsequently, two possible steps with $I_2^{\cdot-}$ can occur by one or two way (1.9 b, 1.9 c).



**(1.9 c)**

Chapter 2. Characterization and modeling of dye-sensitized solar cells

2.1 Characterization of dye-sensitized solar cells (DSSCs)

2.1.1 Efficiency measurement with J-V curve

The current-voltage (J - V) characteristics of DSSCs under illumination are used to determine the power-conversion efficiency, η . From such characteristics, open circuit voltage, V_{oc} , is determined at the $I = 0$ intercept, while the short circuit current, I_{sc} (or short circuit current density, J_{sc}), is found at the $V = 0$. A DSSCs have a relatively slow electrical response with high interfacial capacity. Therefore, the scan rate of voltage should be sufficiently slow in the current measurement. The maximum power could be achieved when the $I \times V$ reaches a maximum point. The power conversion efficiency is defined as:

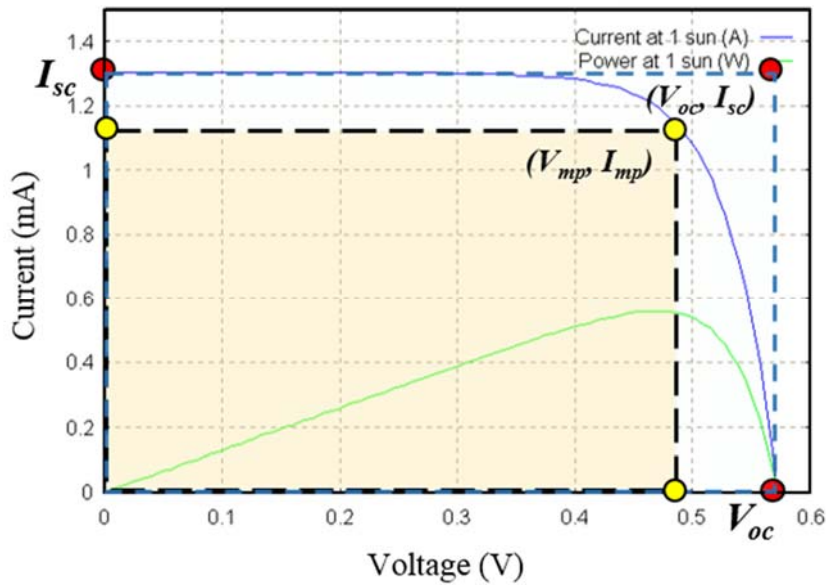


Figure 2.1.1 Photocurrent-voltage curve with short/open points (V_{oc} , I_{sc}) and max points (V_{max} , I_{max}) of solar cells.

$$\eta = \frac{J_{mp} \times V_{mp}}{P_{in}} = \frac{J_{sc} V_{oc} FF}{P_{in}} \quad (2.1)$$

where P_{in} is the power density with photon flux: P_{in} 100mW/cm² (Air mass 1.5) and FF is the fill factor of the device which a value between 0 to 1 that describe the shape of the J - V curve. It is calculated by multiplying both the photocurrent and voltage resulting in maximum electric power, therefore if it indicates high value, the shape became more preferable rectangular with high efficiency.

2.1.2 Incident photon to current conversion efficiency (IPCE)

Solar spectral response of the DSSCs depend on the absorption properties of sensitizer. The spectral response is determined by measuring the monochromatic incident photon to current conversion efficiency (IPCE). Since the DSSCs have a relatively slow relaxation time, it is important to ensure that the measurement duration for a given wavelength is sufficient for the current to be stabilized. Besides, DSSCs have slow response times compared with solid-state photovoltaic, so that a low chopping frequency should be chosen. In order to check the IPCE spectra, two kind measuring methods can be used: AC and DC method. In the AC method, the monochromatic light is mechanically chopped by chopper and the current response is measured by lock-in-amplifier. Moreover, white bias light can be added at AC condition. In the DC method, monochromatic light is obtained by passing white light through a monochromator and the photocurrent is measured. The J_{sc} in full sun light is integrated sum of IPCE spectrum by the following expression:

$$J_{sc} = \int IPCE(\lambda) e\Phi_{ph}(\lambda) d\lambda \quad (2.2)$$

where e is the elementary charge, Φ_{ph} is the photon flux, and λ is the wave length. Thus IPCE can be expressed as follows:

$$IPCE(\lambda) = LHE(\lambda) \eta_{inj}(\lambda) \eta_{cc}(\lambda) \quad (2.3)$$

At the equation of 2.3, each parameter such as LHE, η_{inj} , and η_{cc} are the light harvesting efficiency, efficiency of the electron injection, and charge collection respectively. From a fundamental view point, IPCE value which is also called EQE, is the ratio of the observed photocurrent divided by the incident photon flux, uncorrected for reflective losses during optical excitation through the conducting glass electrode and shows how efficient the numbers of photons are converted into current.

$$\begin{aligned}
 \text{IPCE} &= \frac{\text{number of electrons through the external circuit}}{\text{number of incident photon}} \\
 &= \frac{[1240 \text{ (eV nm)}][\text{photocurrent density } (\mu\text{Acm}^{-2})]}{[\text{wavelength}(\text{nm})][\text{irradiation}(\text{mWcm}^{-2})]} \quad (2.4)
 \end{aligned}$$

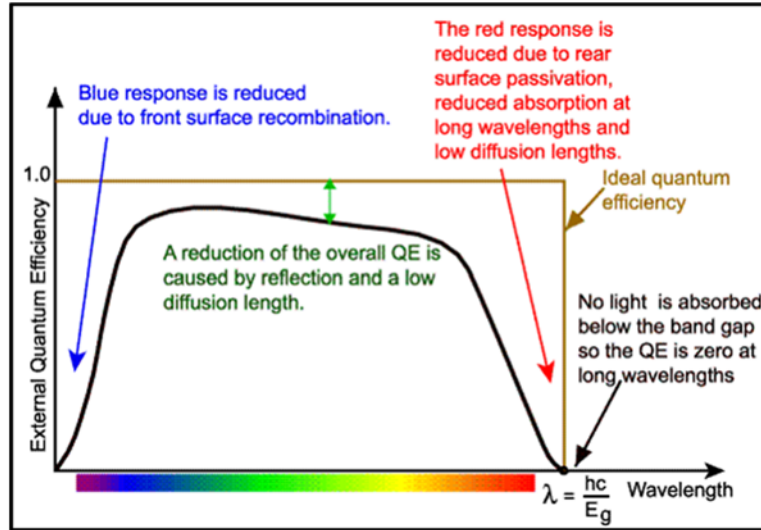


Figure 2.1.2 The quantum efficiency of a conventional silicon solar cell.

2.1.3 Electrochemical method: cyclic voltammetry, electrochemical impedance spectroscopy

Electrochemical methods such as cyclic voltammetry (CV) and electrochemical impedance spectroscopy (EIS) are powerful techniques for characterize the DSSCs. By using the potentiostat which connected with three electrode cells: working electrode, counter electrode, and reference electrode, the most widespread electrochemical CV technique can be performed. At the CV, the potential is swept at a constant rate and reversed at a certain point, while the current is monitored continuously. The measured current occurred from faradaic and non-faradaic reaction. From CV, the formal potentials of redox can be determined and information on the reversibility of the electron transfer process is obtained.

Electrochemical impedance spectroscopy (EIS) is widely used to study whole DSSC system or components such as counter / working electrode or diffusion of electrolyte. EIS can be performed with a sinusoidal modulated voltage. In this system, the applied potential is perturbed by a sine wave modulation and the resulting current is measured as a function of modulated frequency. The impedance response of a DSSC is related to the response of the various components of the device. For a resistor, the impedance shown real value, independent of modulated frequency, while capacitor and inductors

shown an imaginary value which was varied with frequency. Moreover, the impedance associated with transport of ions in the electrolyte by a finite Warburg element (W) which appears in series with the charge transfer resistance associated with electron transfer at the cathode. The remaining elements are the double layer capacitance of the cathode and the series resistance of the DSSC. Using EIS technique, the following parameter can be obtained: series resistance, charge transfer resistance, diffusion resistance, the resistance of electron transport and recombination in the working electrode, and the chemical capacitance of the working electrode. The equivalent circuit of the DSSC is shown in figure 2.1.3.

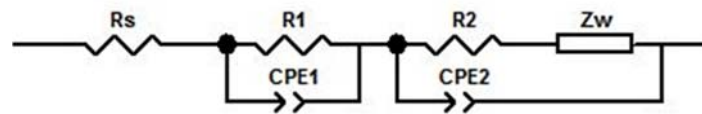


Figure 2.1.3 An equivalent circuit of the DSSCs.

In this circuit, R_s , CPE, R_1 and R_2 represent series (sheet) resistance in high frequency region, constant phase element which was equivalent electrical circuit component, and resistances respectively. Nyquist plot with a commonly suggested circuit was employed to investigate the interfacial properties of DSSC and figure 2.1.4 shows the Nyquist plot of general DSSC.

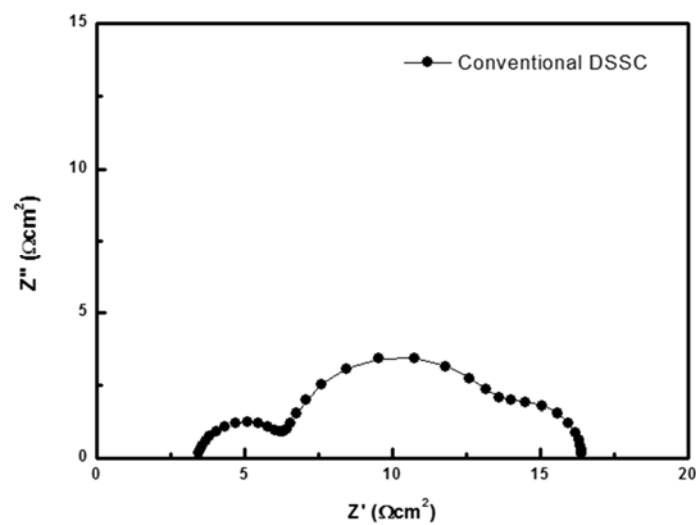


Figure 2.1.4 Nyquist plot of conventional DSSC.

At the figure 2.1.4, the first semicircle at the high frequency is ascribed to the charge transfer at the interface between the counter electrode and electrolyte (R_{ct1}), and the second semicircle at the middle frequency is associated with the charge transfer across the dye/ TiO_2 /electrolyte (R_{ct2}). The additional third semicircle is attributed mainly to the Nernst diffusion of I_3^- ions within the electrolyte (R_{diff}). In order to analyze more detail, the Bode phase plot can be measured.

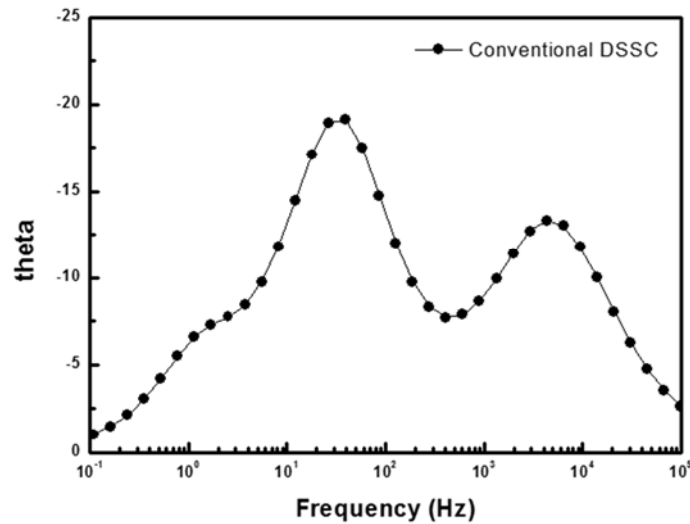


Figure 2.1.5 Bode plot of conventional DSSC.

The fitted Bode plot in figure 2.1.5 displays the frequency peaks of the various charge transfer at different interfaces. The electron recombination time could be calculated by $\tau = 1/(2\pi f_{max})$ equation, where f_{max} corresponds to the highest frequency value of the peak in the bode plot. From this figure, the cell gave the f_{max} value of 39.26 Hz and the corresponding τ value was calculated as 4.05 ms.

2.2 Development of dye-sensitized solar cells (DSSCs)

DSSC is the device that absorbs photon and converts them to electric charge without the need of intermolecular transport of electronic excitation. In conventional solar cells both light absorption and

charge carrier transport were performed simultaneously, whereas in DSSC the two operations are performed separately. It also can be introduced many applications from flexible solar modules, semitransparent solar cells in windows, and stacked tandem solar cells. Various approaches, such as new materials or/and structures to improve spectral response and new materials for the electrodes have led to the improvement of power conversion efficiency and cost-effective device for the commercialization.

2.2.1 Improvement of spectral response

Among the approaches for harnessing solar energy and converting it into electricity, the DSSC is one of the most promising device. However, the absorption spectra of DSSC is not competitive with silicon solar cells yet, (see figure 2.2.1) neither many attempts have been carried out to increase the energy conversion efficiency using broaden the absorption spectra of the cells, including tandem DSSC, co-sensitization, and hybrid DSSC.

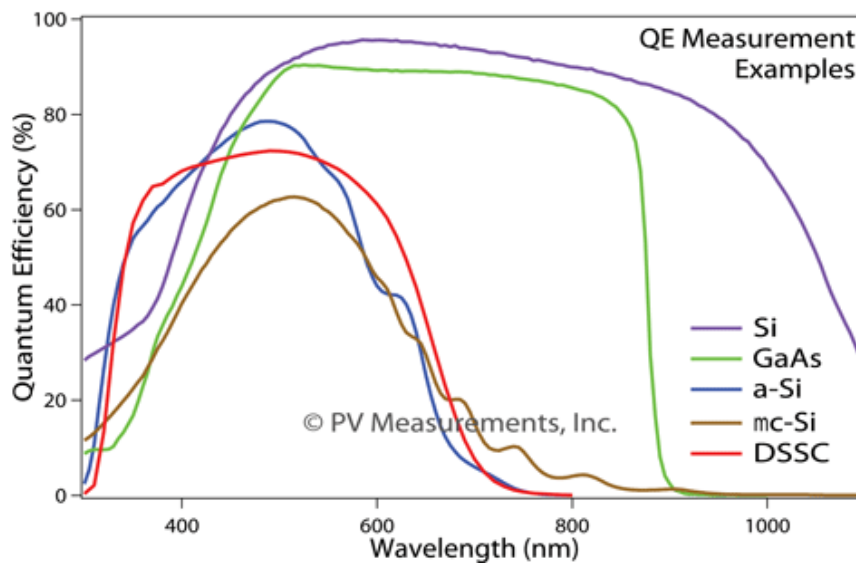


Figure 2.2.1 IPCE spectra of various type of solar cells

In order to achieve an extended light spectral in DSSCs, the most advancing challenge is to choose light absorber. The light absorber is the primary active materials with the specific color for the cell. The first dye as a light absorber is N3 sensitizer, which responds to visible light range. However, the spectra of sun has down to infrared with longer wavelength. By using Ru complex dye, the band gap of light absorber can be established around 2eV, and theoretically maximum efficiency can be calculated around

33%.³⁷ However, this 2eV is quite large to cover the whole range of light spectrum. To harvest a broader spectrum of the sun light, various dyes such as many Ru complex and organic dyes are designed and applied to the DSSCs. Furthermore, the panchromatic system was introduced with extended spectral response.

The new dye for panchromatic application was introduced at 1997 by Nazeeruddin et al.³⁸ A black trithiocyanato-ruthenium(II) terpyridyl complex were used for the photo sensitizer, N749, so called black dye was synthesized. This panchromatic sensitization was efficiently extended the whole visible range up to 900nm. By Islam et al, similar spectral response was obtained using b-diketonato Ru(II)-polypyridyl complexes, Ru(4,4,4-tricarboxy-2,2':6,2''-terpyridine)(1,1,1-trifluoropentane-2,4-dionato)(NCS) and Ru(4,4,4-tricarboxy-2,2':6,2''-terpyridine)(1,1,1-trifluoroicosane-2,4-dionato)(NCS) at 2002.³⁹ Arakawa group reported tandem DSSCs with efficiencies of over 10% using cis-dithiocyanate-N,N'-bis-(4-carboxylate-4-tetrabutylammoniumcarboxylate-2,2'-bipyridine) ruthenium(II) (N719) and tri(isothiocyanato)(2,2':6',2''-terpyridyl-4,4',4''-tricarboxylic acid)ruthenium(II) (Black dye).^{40,41} (see figure 2.2.2 and 2.2.3) Furthermore, employing more than one dye is considered as a broadening of light response. At the very beginning, different dyes are mixed in a solvent as so called 'cocktailing dye' successfully utilized broad sunlight absorption and researchers using similar concept of mixing dyes with various porphyrins.⁴²⁻⁴⁴ (see figure 2.2.3) However, simply mixing of dyes in a one batch is not considered as a best way to making the multiple coated working electrode. The mixed dyes do not show an ordered self-assembled monolayer, neither negative interactions between the molecules.

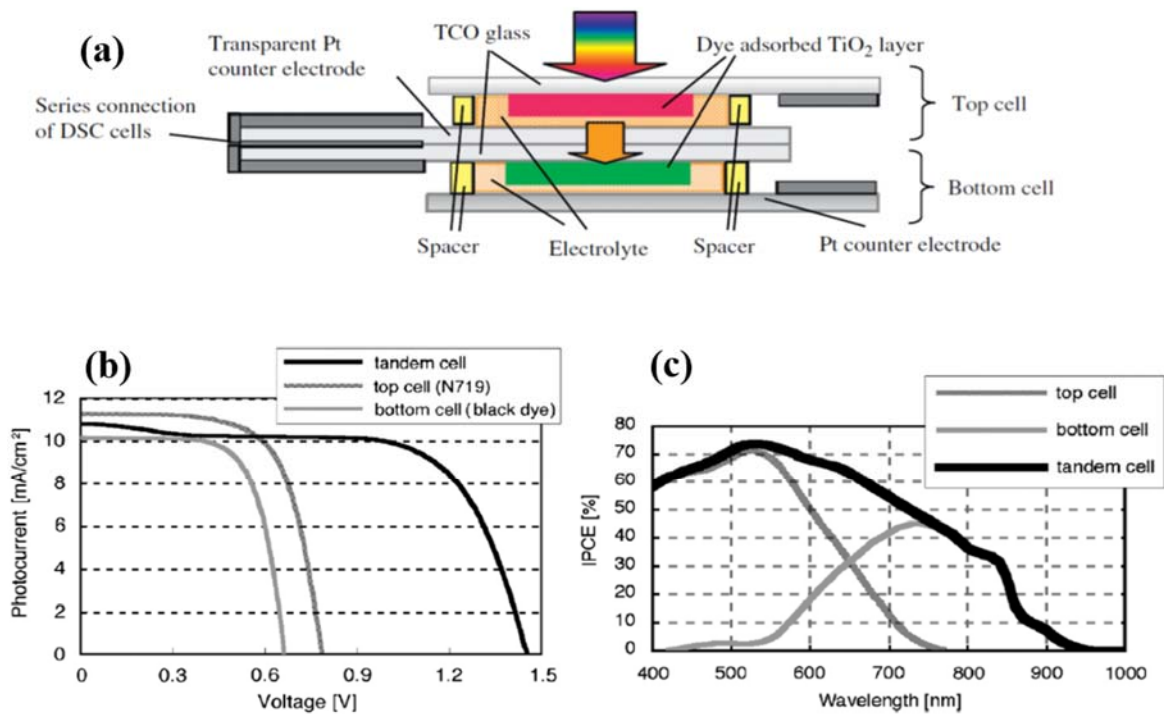


Figure 2.2.2 Schematic structure of series- connected tandem DSSC (a), $I-V$ curves for the best performance of tandem DSSC and individual cells (b), and IPCE spectra of the tandem DSSC and individual cell. Reproduced in part with permission from ref.⁴⁰

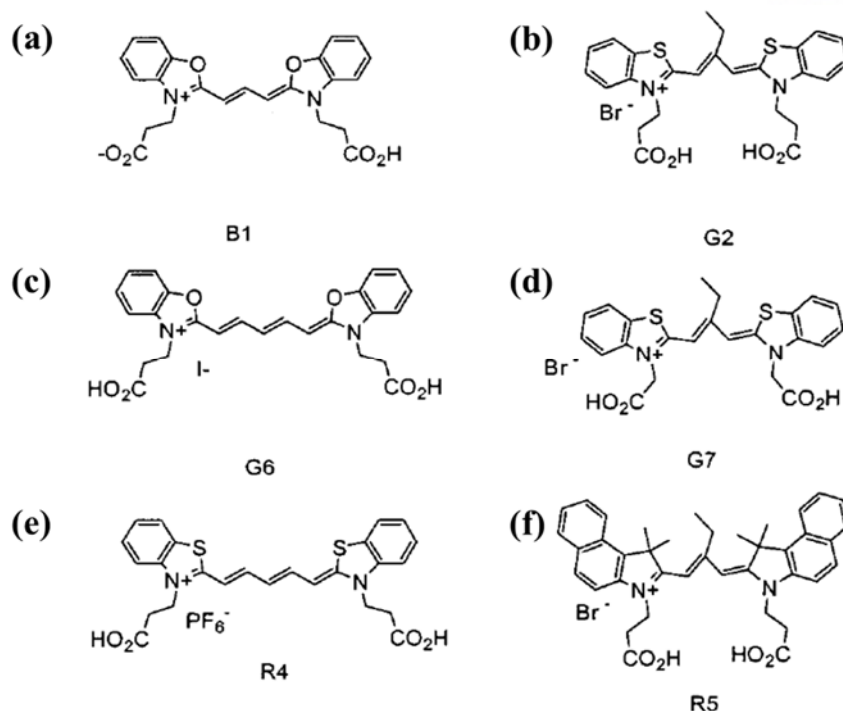


Figure 2.2.3 Structure of dyes used in previous work by other groups. B1 (a), G2 (b), G6 (c), G7 (d), R4 (e), and R5 (f). Reproduced in part with permission from ref.⁴²

In order to extend the light response excepting the cocktailing dye method, Hayase et al. reported the multi layered dyes by pressure-supported dye coating at 2008.⁴⁵ By applying pressure, first layer of dye was coated with precise thickness of TiO_2 at 40-60°C. Once the coating was stopped at a certain time, the rest of the TiO_2 layer was coated by dipping it in the second dye solution and the device successfully represented the sum of each single layered cell. For the double layer formation, dye-replacing method was suggested with NK3705 and Z907.⁴⁶ At 2004, Clifford et al. suggested the multiple electron transfer with Al_2O_3 layer inserted electrode.⁴⁷ At 2005, Nelles et al. reported low temperature fabricating method using transfer technique (figure 2.2.4 (a))⁴⁸ and Choi et al provided stepwise co-sensitization of working electrode with organic dyes in 2008.⁴⁹ After one year, Lee et al. applied three different dyes with highly selective positioning method.⁵⁰ The electrode was coated with N719 dye. After that, styrene oligomer was filled in the dye coated electrode, and polymerized. Using an aqueous NaOH solution, coated N719 dye molecule were detached from the TiO_2 surface. Finally, selective etching removed polystyrene and the naked TiO_2 layer can be prepared for the next dye layer (figure 2.2.4 (b)). Three dye layers can be obtained in a similar way. When we employ more than two dyes in a working electrode, the final current densities are obviously expected to increase. However, the open circuit voltage is more complicated.

Using high temperature sintering for each layer, Miao et al. reported multilayered working electrode prepared via transfer method.⁵¹ They prepared the first layer using the conventional method on FTO glass by the high temperature sintering process. However, the second layer was prepared on the ceramic tile which has low adhesion with TiO₂. This second layer was easily transferred to the first layer by a friction action. (figure 2.2.4 (c)) Instead of using the transferring method, Huang et al. introduced stamping method to fabricating multi layered electrode.⁵² TiO₂ NPs were dispersed in ethanol, and coated on an ITO-PEN substrate using a doctor blade method. The film was attached on the substrate using a cold isostatic press at a pressure of 100 MPa for 3 minutes. The same process was completed with another kind of dye on a non-conductive PEN substrate without pressing. The un-pressed film was transferred onto a previously pressed ITO-PEN substrate working electrode. This method utilizes the transfer of the un-pressed layer onto the already pressed working electrode. (figure 2.2.4 (d)) Yang et al. prepared the multiple dye coated electrode using a layer by layer fabrication in 2011⁵³ and Lan et al. reported enhanced photovoltaic performance with co-sensitization of porphyrin and an organic dye.⁵⁴

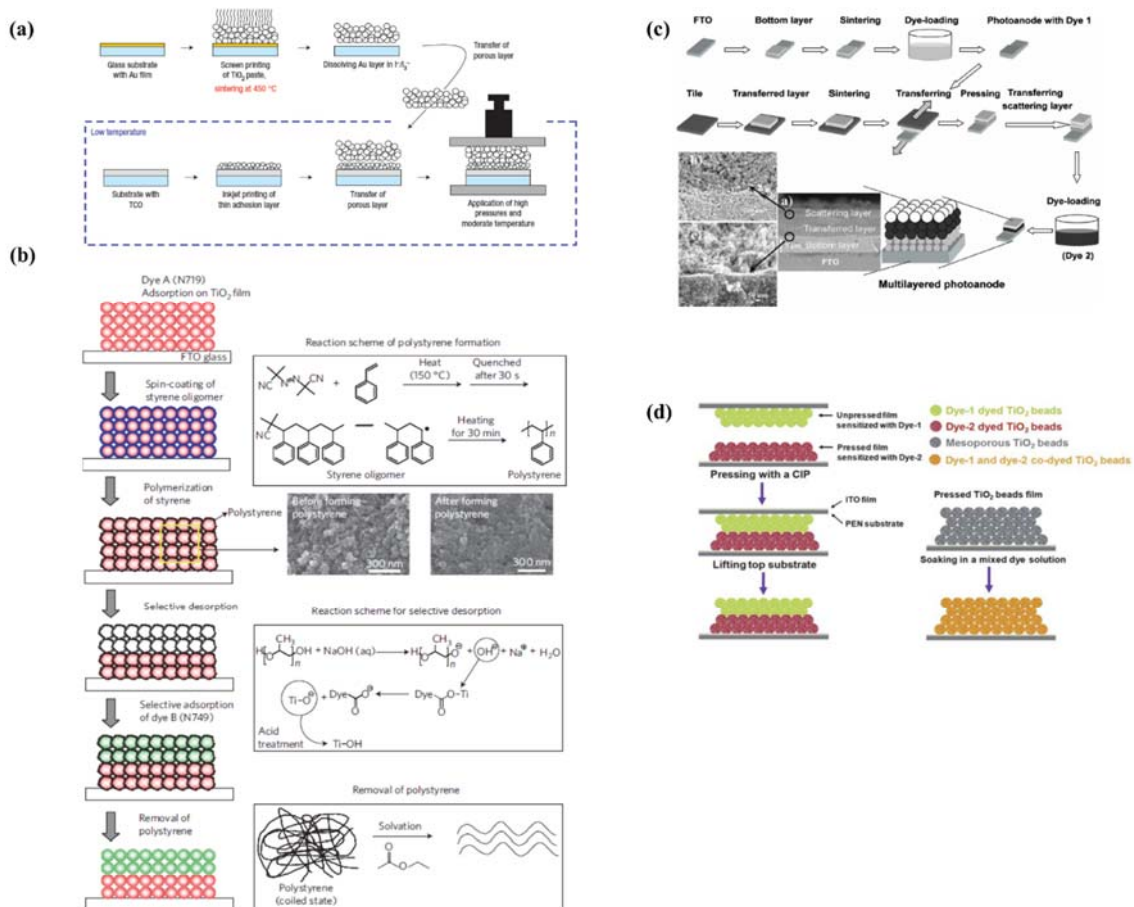


Figure 2.2.4 Schematic of a bi-layered working electrode with low transfer method (a), Schematic representation and reaction scheme of the bi-layered working electrode fabrication process (b), Schematic representation of a multilayered working electrode prepared via sintering followed by the transfer method (c), and Schematic representation of a double dye layer sensitized electrode prepared by the stamping method with mixed dye-sensitized electrode prepared by the cocktail method. (d) Reproduced in part with permission from ref.^{48, 50, 51, 55}

In addition, other attempts have been carried out to broaden the absorption spectra. Several groups reported the co-sensitizing method using a mixture of two dyes in order to improve the efficiencies by broadening the absorption spectra of DSSCs.^{42, 56, 57} Durrant et al. proposed a co-sensitization method with an under-layer of TiO₂ /dye 1, using an Al₂O₃ layer as the separating layer from dye 2.⁴⁷ Ko et al. also obtained an extended spectra by using two complementary organic dyes, JK-2 and SQ1, and they achieved higher efficiency than that of a single dye device.⁴⁹ However, the problem is that either series tandem (S-tandem) or parallel connection of tandem (P-tandem) DSSCs should be adjusted of the transmittance of the top cells. Furthermore, the short circuit current density (J_{sc}) and open circuit voltage (V_{oc}) of the two cells must be tuned for series and parallel tandem DSSCs, respectively.⁴⁰ In the parallel connection, the current density is the sum of the current densities of the top and bottom cells, but the photovoltage is supplied by the low-voltage cell or middle of them. In the series-connected tandem DSSCs, the photovoltage becomes the sum of photovoltage of the top and bottom cells, but the current density of both the top and bottom cells should be tuned to be identical. Furthermore, the top cell is required to have a high voltage and the bottom cell should have a longer-wavelength absorption area as compared to the top cell.

2.2.2 Cost-effective counter electrode

A counter electrode: an electrode with good catalytic activity for electron transfer to the redox electrolyte. The most common counter electrode in DSCs is platinum-coated FTO-glass. This electrode has the advantage that it can be transparent, as a very low loading of Pt is needed. Thermally platinized electrode has high electro-catalytic activity with high stability. However, the cost and limited supplies of Pt have brought a great deal of seeking alternatives for Pt. Thus far, only a limited number of materials have been successfully used as counter electrodes due to the corrosion of metals by the iodine electrolyte. So far, nitrides,⁵⁸⁻⁶³ carbides,⁶⁴⁻⁶⁹ and metal sulfides⁷⁰⁻⁷⁹ have been utilized as counter electrodes.

As more cost-effective materials for CEs, a variety of carbonaceous materials have been used. One

of the carbonaceous, graphene, which has thick and two-dimensional carbon lattice arranged in hexagonal is a hot issue in research.⁸⁰ High carrier mobility of monolayer graphene,^{81, 82} high optical transparency,⁸³ and surface area⁸⁴ properties lead exploration of graphene for use as field emission,⁸⁵ transparent electrode,^{86, 87} Li-ion battery⁸⁸ and super capacitor.⁸⁹ Graphene also been used be a promising counter electrode for DSSCs because of its high conductivity, corrosion resistance, transparency, and high electro-catalytic activity.⁹⁰⁻⁹⁷ Carbon nanotubes (CNT) also attracted numerous attention as practical alternatives for Pt-free counter electrode in DSSCs with its advantages such as large surface area, chemical stability, and electrical conductivity⁹⁸⁻¹⁰³ Especially, MWCNT have been widely used to replace Pt in counter electrode with the aim of higher efficiency than conventional one.^{99, 104-106} Beside graphene and CNT, other forms of carbonaceous materials have also been used as alternative counter electrode in DSSCs. On account of their excellent electrical conductivity, high thermal stability, high corrosion resistance, low cost, and good catalytic activity, carbon materials are extensively employed in DSSCs. Inverse opal carbons, mesocellular carbon foam, amorphous carbon, carbon black, and mesoporous carbon are widely applied with traditional I/I_3^- redox couple electrolyte.¹⁰⁷⁻¹¹²

Recently, extensive studies have been performed using conducting polymers as alternative cathodes in DSSCs due to their excellent catalytic activities, low cost, high transparency, good conductivity, easy preparation and good environmental stability. As indicated in figure 2.2.5, various organic materials, such as PEDOT,¹¹³⁻¹¹⁵ polyaniline (PANI),¹¹⁶⁻¹²⁰ porous poly(3,4-propylenedioxythiophene) (PProDOT),^{121, 122} and polypyrrole(PPy)^{123, 124} were commonly applied to iodine electrolyte with a comparable catalytic activity and PCE with prevalent Pt cathode. Furthermore, table 2.2.1 shows several conductive polymer counter electrode with different electrolytes.

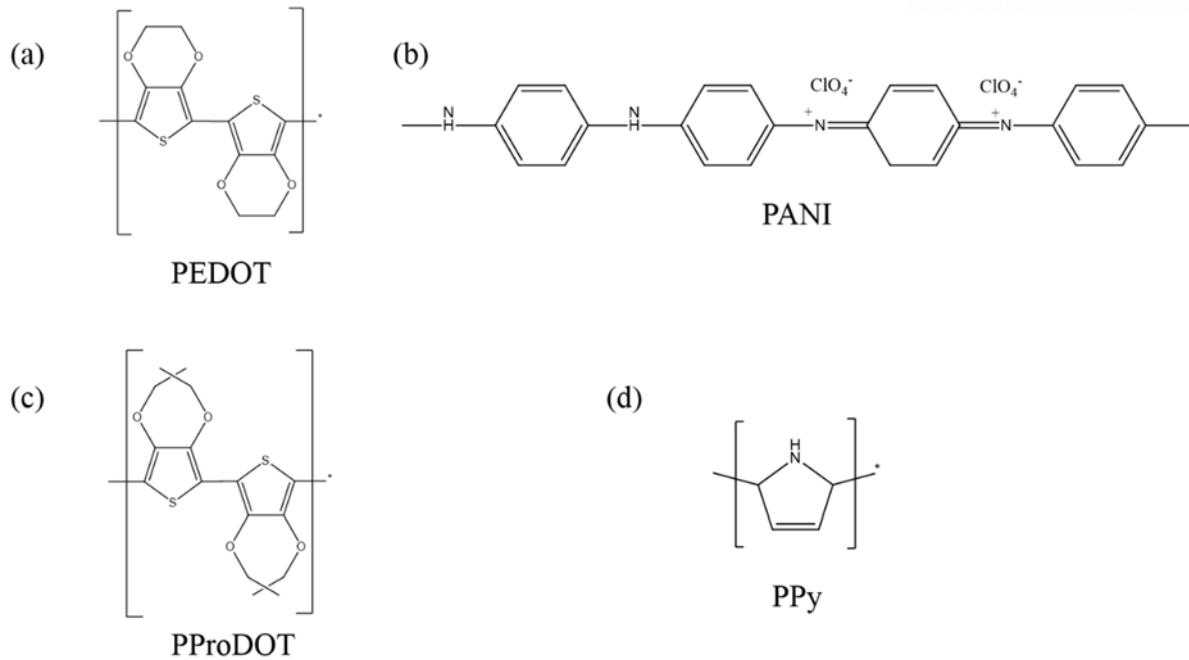


Figure 2.2.5 Chemical structure of conducting polymers as alternative cathodes in DSSC (a) PEDOT, (b) PANI, (c) PProDOT, and (d) PPy.

Table 2.2.1 Performances and references with various conductive material counter electrode.

Counter	Sensitizer	Redox couple	V _{oc}	J _{sc}	FF	Eff	Ref
PEDOT	TH305	T ₂ /T ⁻	0.745	12.5	0.65	6.0	¹²⁵
PEDOT	Z907	T ₂ /T ⁻	0.687	15.9	0.72	7.9	¹²⁶
PProDOT	N719	I ⁻ /I ₃ ⁻	0.761	17	0.71	9.25	¹²⁷
PProDOT	Y123	Co ₃ ^{+/2+}	1	13.06	0.77	10.08	¹²⁸
PEDOT/ITO/PET	Z907	T ₂ /T ⁻	0.639	14.2	0.65	5.9	¹²⁶

Moreover, some transition metal nitrides has been reported with metal like behavior.^{129, 130} It shows similar electronic structure of metal nitrides and it may replace Pt as counter electrode in DSSCs. Generally, anodized Ti nanotubes with simple nitridation, TiN, show an excellent performance¹³¹ and nitridated Ti nanoparticles with carbon nanotubes provided high catalytic performance.¹³² Furthermore, VN, Mo₂N,^{59, 133} surface nitride nickel foil,¹³⁴ micro-nano TiN sphere,⁶¹ TiN conductive carbon black composite.¹³⁵ and ordered mesoporous TiN-carbon¹³⁶ was developed.

Chapter 3. Fabrication of panchromatic dye-sensitized solar cells using pre-dye coated TiO₂ nanoparticles by a simple dip coating technique

This chapter reproduced with permission from J. Lim, et al, RSC Advances, 2013, 3, 4801,

Copyright 2014 Royal Society of Chemistry.

3.1 Research overview

Theoretical efficiency of dye sensitized solar cell is estimated to be around 25-30%, but the practical efficiency reported until now in literature, did not cross a half of its theoretical value. Many research attempts have been carried out to improve this efficiency by improving the nanostructure of materials, developing efficient electrolyte and sensitizers. Since the individual sensitizer has its own absorbance limitation to harvest the broad range of the solar spectrum, the concept of tandem structure and panchromatic engineering has been developed. Co-sensitization of TiO₂ with multiple dyes using cocktailing of a mixed dye solution is a simple approach and has a disadvantage of negative interaction between dye molecules, which leads to poor cell performance. Sequential positioning of multilayer TiO₂ sensitized with different dyes is a promising method but the so far reported literature focuses on the complex fabrication procedures. Here in this article, I have developed a more prominent way of dye coating known as pre-dye coating of TiO₂ NPs, which has been applied to fabricate the multilayer panchromatic DSSCs using the facile dip coating technique. Unlike the conventional method, this approach does not involve any high temperature calcination processes, so it could be implemented for the fabrication of flexible panchromatic DSSCs.

An appropriate method of pre-dye coating of TiO₂ nanoparticles (NPs) and a facile approach of a dip coating technique have been adopted for the fabrication of panchromatic dye-sensitized solar cells (DSSCs). A bi-layer photoanode consists of two distinct layers of TiO₂ films, which were individually sensitized with N719 and N749 dyes and then coated on a TCO substrate in a sequenced manner. The spectral response of panchromatic DSSCs has been investigated using monochromatic incident photon to current conversion efficiency (IPCE) spectroscopy. The IPCE spectrum of panchromatic DSSC revealed the absorption characteristics of each single dye cell. The broader absorption spectra were obtained up to 850 nm of near IR region and the higher quantum efficiency than those of single cells were recorded. The higher value of IPCE is correlated with the higher short circuit current density value of panchromatic cell ($J_{sc} = 13.4 \text{ mA cm}^{-2}$). The tandem cell showed an average open circuit voltage (V_{oc}

= 0.79 V) of the single dye cells with an overall conversion efficiency of 7.1%. Moreover, the present approach does not require any high temperature sintering process; therefore it could be suitable for the fabrication of flexible panchromatic DSSCs.

3.2 Background and Introduction

Due to the limitations of fossil fuels, various energy conversion devices utilizing the renewable energy have been developed. Among those, photovoltaic cells are an ideal choice which can directly convert the solar energy into electricity. As a result of advantages such as variety of colors, high energy conversion efficiency, ease of fabrication and low cost, dye-sensitized solar cells (DSSCs) have been intensively studied for the past two decades.⁵ The working electrode of DSSC consists of dye sensitized TiO₂ nanoparticles in which dye molecules act as a primary active component for the absorption of the solar spectrum. One way of achieving high solar-to-electrical conversion efficiency is to improve the spectral response of the sensitizers i.e. the dye molecules should absorb the sun's spectrum at as a wide range of wavelength as possible. On account of absorbance limitation, however, the individual sensitizer can only absorb its own particular range of wavelength. For the maximum energy harvesting of DSSCs, a panchromatic approach, which could absorb the photons over the entire range of visible spectrum has been proposed.

The co-sensitization of a TiO₂ film, using different dyes, was the first approach in making a panchromatic DSSC.^{43, 44, 137-141} In this case, dyes with different absorption properties were mixed together and a TiO₂ film, supported with TCO glass substrate, was immersed into the cocktail-dye solution for a definite period of time. The IPCE spectra showed a combined effect of different dyes and a broader light harvesting spectrum. However, the mixing of different dyes in a single pot results in a negative interaction between the dye molecules, which may not show an ordered self-assembled monolayer on the TiO₂ surface. This phenomenon leads to a poor performance of panchromatic DSSCs. An adsorption of multiple dyes in the discrete multi-layer of TiO₂ is an ultimate option for extending the absorption range of the solar spectrum without any adverse effects. However, the conventional method of TiO₂ working electrode fabrication involves high temperature calcination, followed by a dye adsorption process. This high temperature sintering process is one of the main drawbacks for the multi-layer adsorption of different dyes. Since the dye molecules adsorbed on the first layer of TiO₂ could be decomposed during the calcination of subsequent TiO₂ layers. To overcome this issue, the following attempts have been carried out by researchers: a stepwise co-sensitization,^{47, 142, 143} highly selective positioning method,⁵⁰ a dye replacing technique,^{45, 46} layer by layer fabrication of different dye layers⁵³

and a film transfer technique.⁵¹ Although a sequential positioning of various dyes on a mesoporous TiO₂ electrode enhances the absorption spectrum, the so far reported studies involve complex fabrication procedures. Recently, Huang et al. reported a flexible panchromatic DSSC using a thermal free ‘stamping’ method.⁵⁵ The authors made TiO₂ films using a press method and then films were individually sensitized with the N719 dye for 18 h and GD3 dyes for 2 h in a separate container. GD3 sensitized film was then transferred onto the N719 sensitized TiO₂ layer using the stamping method. Soaking of the TiO₂ film into the N719 dye for a prolonged time could be suitable for the films made by conventional method because of the strong adhesion force between the film and the substrate. But, in the case of the pressing method, the adhesion is not as strong as the conventional method and the film may be peeled off from the substrate due to the action of the solvent. Therefore, better methods of dye coating need to be developed. Although, Huang et al. reported a bi-layer structure using the stamping method, the multi-layer fabrication would be questionable owing to the different adhesion properties between the films. In this work, I have adopted a more prominent way of dye coating and simple dip coating methods for the fabrication of multi-layer panchromatic cells. Initially, TiO₂ NPs are soaked in a dye solution for a prolonged time. The pre-dye coated (PDC) TiO₂ NPs were dispersed in a solvent, dip coated on the substrate and then pressed with hydraulic press for a better interconnection between the NPs and a strong adhesion with the TCO substrate. The panchromatic cell, which consists of a bi-layer working electrode, was also fabricated using N719 and N749 dyes. This process could be extended to the fabrication of a multi-layer. From a commercial point of view, this simple dip coating process and thermal free fabrication procedure, will reduce the manufacturing cost and increase the productivity of flexible panchromatic DSSCs.

3.3 Experimental

A 12 wt% of TiO₂ powder (P25 Degussa) was dispersed in an absolute ethanol solution for 1 h under ultra-sonication. A 0.5 mM dye solution was prepared by dissolving cis-bis (isothiocyanato) bis (2,29-bipyridyl-4,49-dicarboxylic acid) ruthenium(II) (referred to as N719) dye in a mixture of acetonitrile and tert-butanol solvent (v/v = 1/1). To prepare pre-dye coated TiO₂ particles, these two solutions were mixed together and stirred overnight at room temperature in order to adsorb the dye molecules onto the TiO₂ surface. The mixed solution was centrifuged (Combi 514R) at 1000 rpm for 10 min for the separation of solvent and dye coated particles. The excess dye molecules were washed with ethanol and then PDC-TiO₂ particles were separated using a method of centrifugation. The slurry with an optimum viscosity was made by the dispersion of PDC-TiO₂ particles in ethanol solvent.

Fluorine-doped tin oxide (FTO) glasses were washed with a detergent solution and DI water. They were then cleaned in an ultrasonic bath for 5 min using an ethanol–acetone solution ($v/v = 1/1$) and 2-propanol. Finally a treatment of UV-O3 was administered for the duration of 15 min. The TiO_2 layer was made by dip coating the FTO substrate into PDC- TiO_2 slurry for 30 cycles. The thickness of the layer was controlled by the number of dipping cycles. Rough drying and pressing process were carried out every 5 cycles to avoid detachment of previously adsorbed TiO_2 layer. After that, the selective active area (0.25 cm^2) was cut off using the glass slide and then pressed at 200 MPa using a hydraulic press to increase the interconnectivity between the nanoparticles. Another dye solution was prepared by mixing 0.4 mM tri(isothiocyanato)(2,29;69299-terpyridyl-4,49,499-tricarboxylic acid) ruthenium(II) (referred to as N749, black dye, dyesol Timo) contained deoxycholic acid 40mM in ethanol. The same procedure was repeated to make a N749 dye coated PDC- TiO_2 electrode. In order to fabricate the panchromatic photoanode, a dip coating of 15 cycles was carried out for each dye solution. For the effective utilization of sunlight, the dyes which could absorb the shorter wavelength of light were placed first on the FTO and then dyes having the absorption properties of longer wavelength of light were placed in a subsequent manner as shown in the following order: FTO/N719 PDC- TiO_2 /N749 PDCTiO₂.

To prepare a Pt counter electrode, 10 M H_2PtCl_6 solution in ethanol was coated on a clean FTO glass followed by annealing at 450°C for 30 min. A 25 μm -thick Surlyn film (DuPont) was placed in between the photoanode and the counter electrode and then sealed to form a sandwich cell. The electrolyte solution containing a mixture of 0.6 M 1-hexyl-2,3-dimethylimidazolium iodide, 0.1 M guanidine thiocyanate, 0.03 M iodine, and 0.5 M 4-tert-butylpyridine in acetonitrile was introduced into the system. Finally, the samples were kept for a few hours with edge masking by black tape.

The photovoltaic properties of the prepared DSSCs were measured using a Keithley 2400 digital source meter under the irradiation of a solar simulator (AM 1.5 G, 100 mW/cm^2 , Sol3A, class AAA, Oriel) as a light source. The intensity of the light was calibrated to 1 sun using a standard single crystalline Si-reference cell (PV Measurements, Inc.). The photovoltaic performance has been characterized by the V_{oc} , J_{sc} , fill factor (FF), and overall efficiency (η) values obtained from the J–V curve. The IPCE spectra were measured by PV measurement (PV Measurements, Inc., QEX7 series). Surface morphology was carried using a field emission-scanning electron microscopy, FE-SEM (Nano230, FEI co.). Thickness of the film was measured using the surface profilometer (P-6, KLA-Tencor, USA).

Pre-dye coated TiO₂ Method

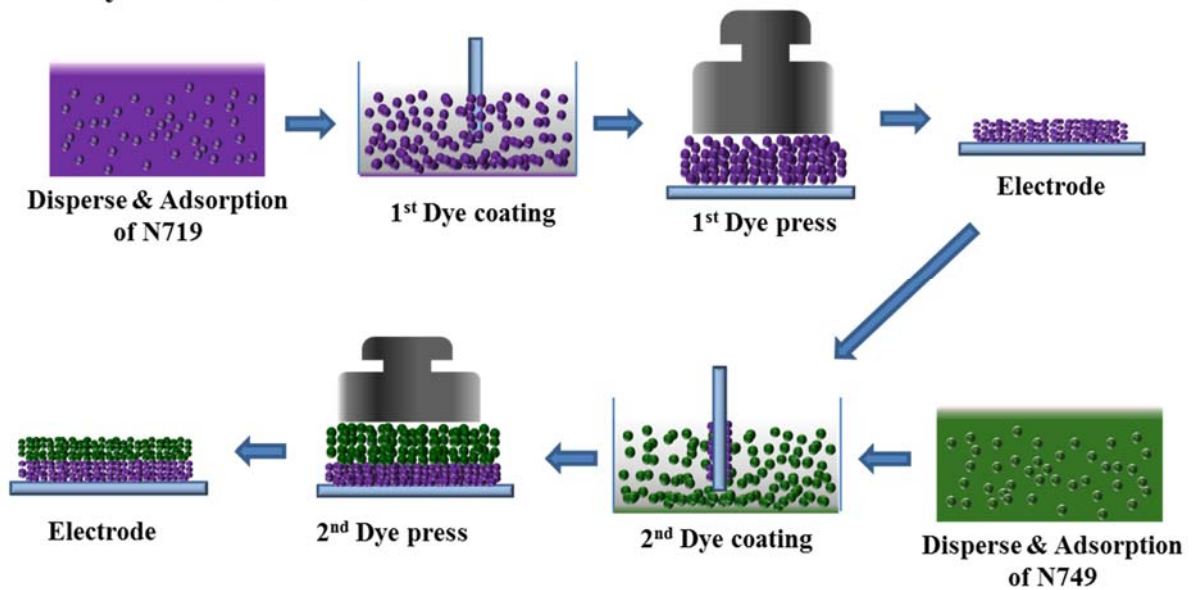


Figure 3.1 A schematic preparation of the panchromatic electrode using the pre-dye coating method.

3.4 Result and Discussion

The schematic preparation of PDC-TiO₂ electrodes is presented in figure 3.1, while the detailed experimental procedures are described in the previous section. For the DSSC system, the microstructure of the TiO₂ film plays an important role in the efficiency of DSSCs. A better contact between particles enhances the charge transport phenomenon. In the meantime, the optimum pore distribution is essential for an efficient percolation of electrolyte into the TiO₂ electrode surface in order to complete the redox cycle. The surface morphology and microstructure of the films were investigated using scanning electron microscopy. Figure 3.2 represents the surface morphology of the dye sensitized TiO₂ film prepared with the PDC method. After compression, PDC particles are firmly interconnected through a uniform pore distribution with inferior aggregation. This could lead to a higher surface area of the electrode and in turn absorption of more photons from the solar spectrum.

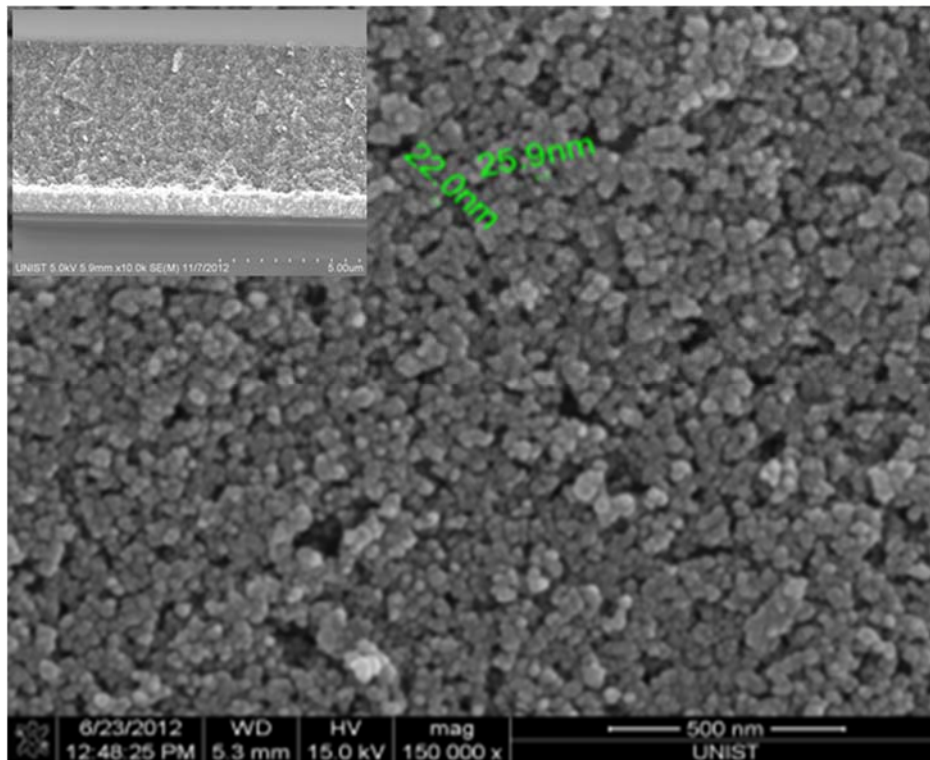


Figure 3.2 SEM images of TiO_2 layer made by the pre-dye coated method. The inset is the cross section view of the electrode.

In order to estimate the possibility of broadening the absorption spectra, I made a new type of panchromatic DSSC with a bi-layered photoanode prepared using a PDC method. The thicknesses of the layers were measured using the surface profilometer. About $3.5 \mu\text{m}$ thickness of each layer with a total thickness of $7 \mu\text{m}$ was obtained by controlling the number of dip coating cycles. For comparison purposes, the individual devices (N719/PDC-TiO_2 , N749/PDC-TiO_2) with a $3.5 \mu\text{m}$ thickness of PDC- TiO_2 films were fabricated separately. Photovoltaic parameters for all three devices were extracted from the J–V curves (see figure 3.3). The values are listed in Table 3.1.

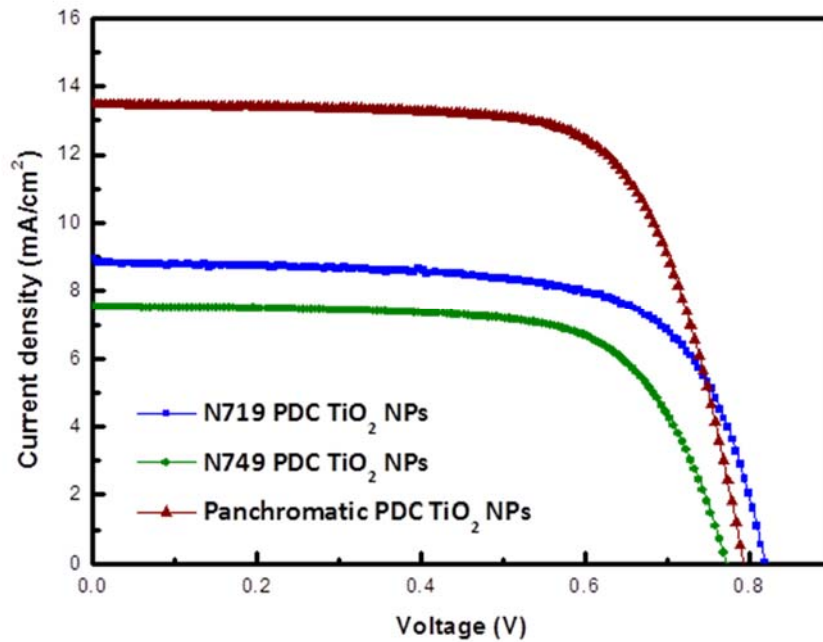


Figure 3.3 Photocurrent-voltage curves of the pre-dye coated samples. Single N719 (blue, squares), single N749 (green, dots), and panchromatic (brown, triangles) cells.

Table 3.1 Photovoltaic performance of the single cells and the panchromatic cell

Samples	J_{sc} (mA/cm ²)	V_{oc} (V)	FF (%)	Eff (%)
N719 / PDC-TiO ₂	8.9	0.81	67.9	4.9
N749 / PDC-TiO ₂	7.5	0.77	68.3	3.9
PAN / PDC-TiO ₂	13.4	0.79	68.1	7.1

A complete cell sensitized with single N719 dye (N719/PDCTiO₂) shows J_{sc} of 8.9 mA/cm², V_{oc} of 0.81 V, FF of 0.679 with Eff of 4.9%. Another single cell sensitized with only black dye (N749/PDC-TiO₂) shows J_{sc} , V_{oc} , FF and Eff values of 7.5 mA/cm², 0.77 V, 0.683 and 3.9% respectively. The panchromatic cell (PAN/PDC-TiO₂) shows a higher photocurrent density of 13.4 mA/cm². The V_{oc} of the panchromatic cell is close to the average value of single cells and is equal to 0.79 V. This average value of V_{oc} is observed and explained in a previous report by Lee et al. The difference of V_{oc} is related to the different degree of back reaction at the TiO₂/dye/electrolyte interfaces and indicates that the V_{oc} of the panchromatic is not likely relying on those of single cells.^{50, 51, 144} This observation confirms the

parallel tandem effect in panchromatic DSSCs. Apparently, the efficiency of the PAN/PDC-TiO₂ cell is higher than those of single cells and the value is around 7.1%.

Figure 3.4 shows the monochromatic IPCE spectra for three devices. The N719/PDC-TiO₂ single cell shows the maximum photoresponse in 400 nm and 530 nm wavelength regions. The N749/PDC-TiO₂ cell shows the maximum response in 425 nm and the broad peak extended up to infra-red region of around 850 nm, in which N719 dye does not show any spectral response. Hence the combination of both dyes in a panchromatic cell (PAN/PDC-TiO₂) shows a higher quantum efficiency value, around 400–420 nm and another maximum photoresponse peak at 530 nm, which extended up to 850 nm corresponding to the high and narrow region of N719 and the broad feature of N749. The higher value of quantum efficiency is further confirmed with the higher J_{sc} value of the panchromatic cell (13.4 mA/cm²) which can be compared to the values of single cells (8.9 mA/cm² and 7.5 mA/cm²). A sequential positioning of multi layers sensitized with the dyes having different spectral response, leads to higher quantum efficiency with a broader spectrum.

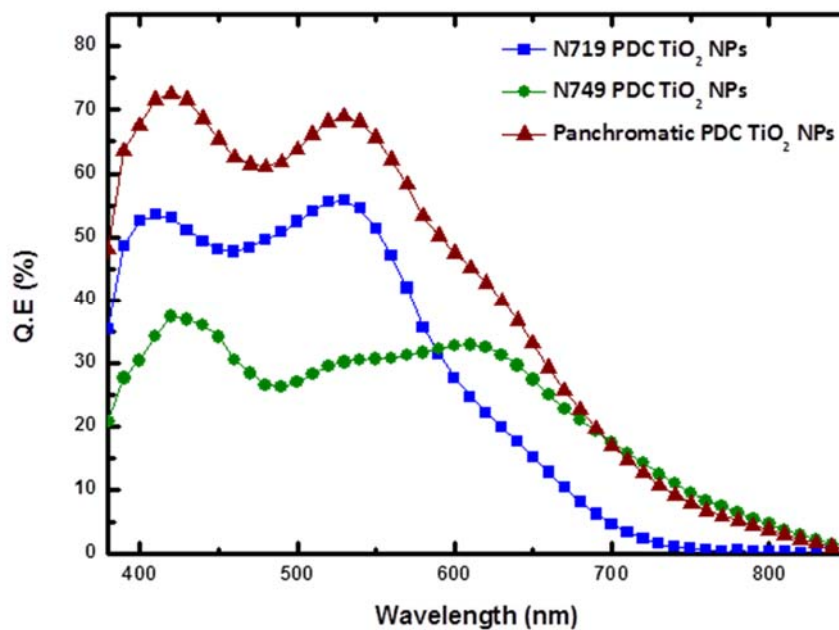


Figure 3.4 Incident photon to current conversion efficiency of the pre-dye coated samples. N719 single cell (blue, squares), N749 single cell (green, dots) and panchromatic cell (brown, triangles).

In order to check the electron kinetic, we compared the prepressed and the dye coating cell (pre-pressed cell, 7 μm + N719) and the PDC TiO₂ NPs cell by using intensity modulated photovoltaic spectroscopy (IMVS). IMVS gives the dynamic electron lifetime in ambient conditions. For the measurement, sinusoidal modulated light of different frequencies (f) illuminated the samples and amplitude is measured under open circuit condition. The electron lifetime can be calculated by $\tau_n = 1/(2\pi f_{\min}(\text{IMVS}))$, where f_{\min} is the frequency giving the lowest imaginary components in IMVS plot.^{145, 146} The IMVS plots of pre-pressed and PDC TiO₂ NPs are presented in figure 3.5. Pre-pressed cell and PDC TiO₂ NPs cell exhibit the f_{\min} as 1.4 Hz and 1.2 Hz respectively and τ_n was calculated to 0.113 and 0.132 s. The τ_n values in PDC TiO₂ NPs cell is quite competitive to pre-pressed cell, which means that pre-coated dyes does not hinder electron flow in PDC cells.

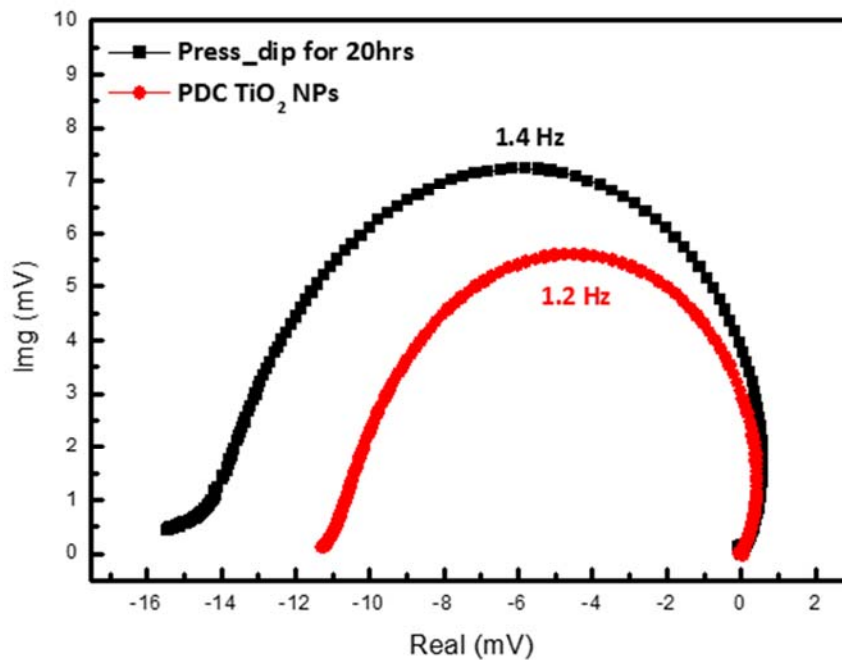


Figure 3.5 Intensity modulated photovoltaic spectroscopy of the pre-pressed cell (black, squares) and PDC TiO₂ NPs cell (red, dots).

Furthermore, the interfacial adherence result in the peeling of two layers, the stability issue will arise to the system. However, I have not observed any peeling off from the working electrode once pressing is completed. At this system, I added pressing process in order to stabilize the layers. Pressing method is already well proved for DSSC system applications from other groups. They successfully

demonstrated many DSSC system with pressing method. Layers adhesion by pressing is also demonstrated at many papers.^{51, 52, 147} I also had been testing long term stabilities to confirm the stability issue, and figure 3.6 represents the stability issue for 5 weeks.

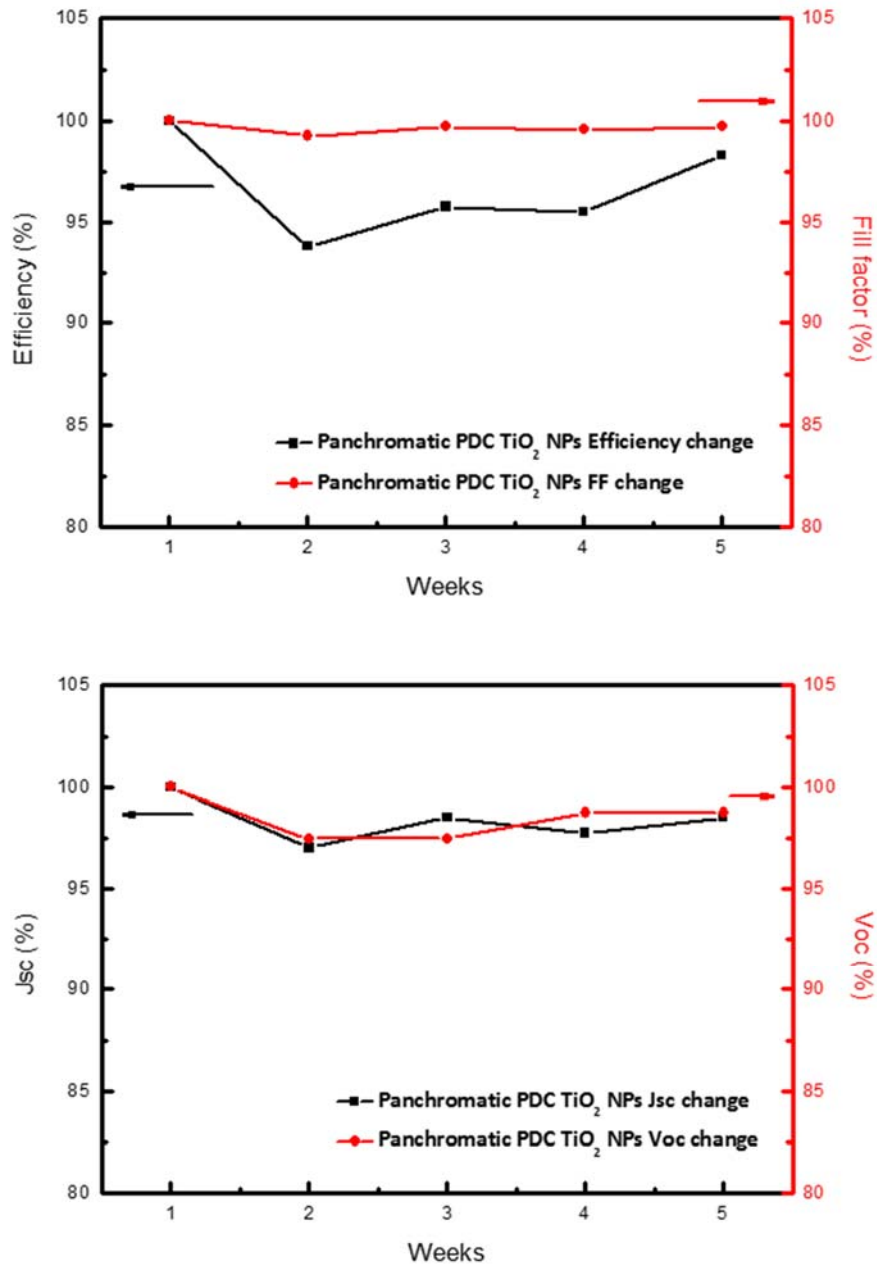


Figure 3.6 Long term stabilities of panchromatic PDC TiO₂ NPs sample. (a) Efficiency, FF change curves and (b) J_{sc}, V_{oc} change curves.

Moreover, within our knowledge, the pre-dye coated TiO₂ nanoparticle pressing method is the first approach of multi-stackable fabricating method without using any organic binder or thermal process. This technique could be extended to produce devices in research, including a triple or more photoanode layer at one substrate, flexible or a tandem solar cell. (figure 3.7)

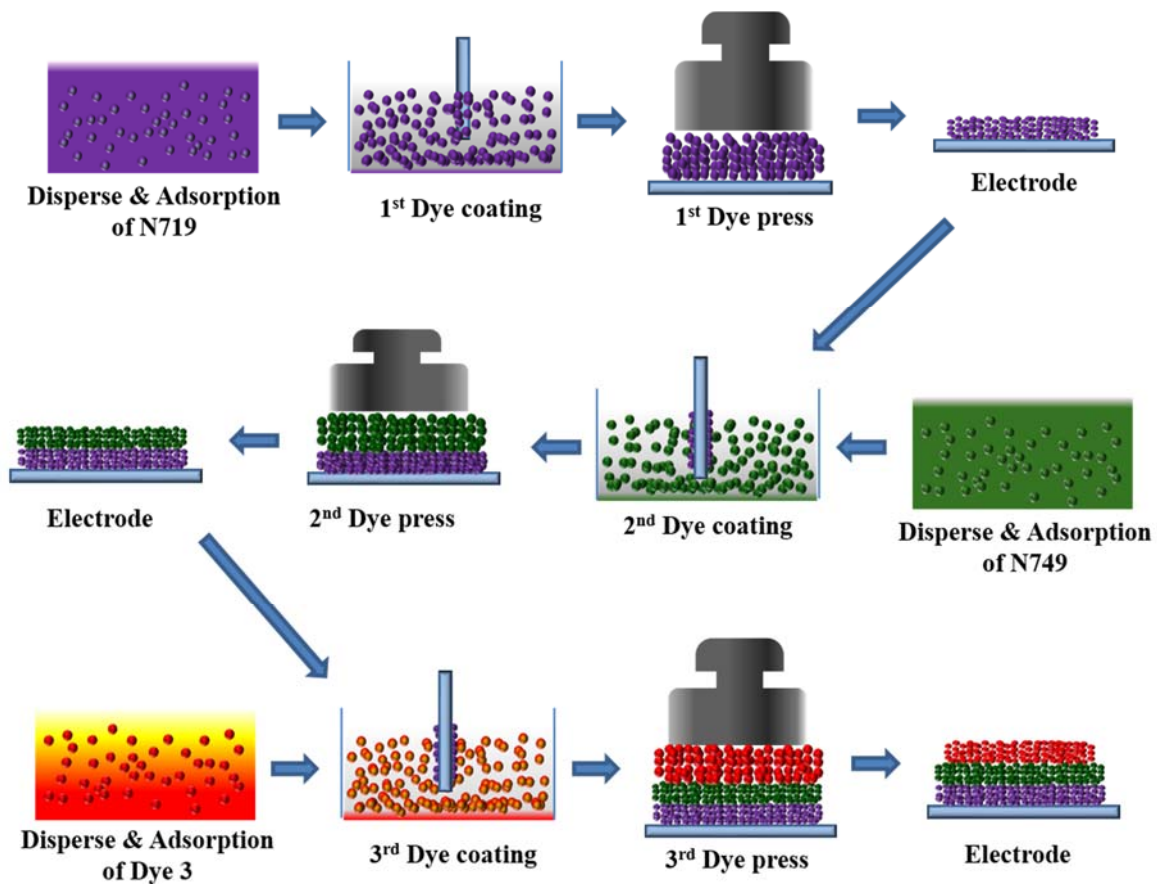


Figure 3.7 A schematic preparation of the triple layered panchromatic electrode using the pre-dye coating method.

3.5 Conclusion

Panchromatic DSSCs have been successfully fabricated using PDC TiO₂ NPs by a simple dip coating technique. The quantum efficiency of panchromatic cells is higher than those of single cells and the IPCE spectra, which revealed the characteristics of N719 and N749 sensitizers. The higher value of J_{sc} of the panchromatic cell confirms the parallel tandem effect. Due to the difference between the dyes, the V_{oc} value of panchromatic cell is slightly affected by the different back reaction of electrons with

the interfaces. This method involves a pre-dye coating of TiO₂ NPs, which could be more suitable for the fabrication of multilayer TiO₂ films using a dip coating assisted pressing method. Further, the whole process involves a thermal free approach, so the flexible substrates could be used instead of traditional glass substrates. In addition to this, the simple dip coating technique and the thermal free approach will reduce the fabrication cost.

Chapter 4. Reversely fabricated dye-sensitized solar cells

This chapter reproduced with permission from J. Lim, et al, RSC Advances, 2014, 4, 243,

Copyright 2014 Royal Society of Chemistry.

4.1 Research overview

Increasing carbon emission and global energy crisis based on fossil fuels urge the development of energy conversion devices utilizing the renewable energy resources. Photovoltaic devices are one of the most promising technologies where in abundance of solar energy could be directly converted to electrical energy. Dye-sensitized solar cells are considered to be the low cost alternative to the commercially available silicon solar cells. But the conversion efficiency of DSSC has been limited to 12.3 % for the laboratory scale devices. One of the ways to increase their efficiency is the combination of DSSCs with the other thin film solar cells such as CIGS, organic solar cells, etc. But the presence of liquid electrolyte and the structural restriction of conventional DSSCs prohibited their application to the tandem devices. Here, I report a novel structure of dye sensitized solar cells (DSSC) with reversed form. This was done by constructing all the components together as one substrate in the following order: platinum, supporting layer, titanium dioxide layer, and indium-doped tin oxide layer. To separate the photoanode from the photocathode and to make room for electrolytes, a layer of nanoparticle was introduced. With this new structure, a power conversion efficiency of 5.4% was achieved with comparable current density and open circuit voltage values to the conventional structure. The electrochemical properties and photochemical properties were checked by electrochemical impedance spectroscopy. Moreover, the present approach could be an encouraging new direction in research while facilitating the fabrication of hybrid tandem solar cells.

4.2 Background and introduction

Dye-sensitized solar cells (DSSCs) are promising alternatives to conventional silicon solar cells and have been studied for the past two decades because of their advantages including color variety, a simple fabrication process, and a relatively high efficiency.⁵ Typical DSSCs consist of a TiO₂ working electrode with dye molecules on transparent conductive oxide (TCO) glass, platinum coated counter electrode, and an electrolyte with a I⁻/I₃⁻ redox system between the electrodes. Extensive research has been

conducted in order that each component achieves highly efficient DSSCs, including alternative materials,^{16, 148-152} new structures of photoanodes,^{51, 138, 153, 154} and modifying fabrication methods.^{155, 156} Currently, fluorine-doped tin oxide (FTO) glass is widely used as TCO for DSSC.¹⁵⁷

Even though the indium-doped tin oxide (ITO) was expected to be a better TCO material than FTO due to higher transparencies and conductivities, the fabrication step for TiO₂ generally requires a 500 °C annealing process and so the ITO substrate is not suitable for DSSC application since its conductivity decreases remarkably during the thermal process.¹⁵⁸⁻¹⁶⁰ Several research papers have proposed to fabricate ITO based DSSCs using poly(ethylene terephthalate) (PET)/ITO,⁴⁸ PET/ITO/titanium dioxide (TiO₂),¹⁶¹ ITO/antimony-doped tin oxide (ATO)/TiO₂,¹⁶²20 and StSt/SiO_x/ITO.¹⁶³ However, these studies are limited to flexible substrates with low temperature process which may show not only poor adhesion between substrates and TiO₂ particles but also poor contact between particles. Here, I introduce a novel structure of DSSCs that utilizes the ITO layer and supporting layer without a high temperature treatment barrier. Since the ITO layer is placed after TiO₂ calcination, the high temperature process does not affect the ITO layer. Moreover, after optimization on the fabricating processes and electrochemical matching, ITO coated reversely form of dye sensitized solar cell can be fabricated one substrate and shows comparable values of current density and open circuit voltage with 5.4% of power conversion efficiency. Moreover, this structure consists of only one glass substrate (FTO coated glass) at the very first at this field and the rear side is covered with the thin transparent ITO layer by sputtering method which enables the stacking of other thin film solar cells to form Tandem structure.

4.3 Experimental

Fluorine-doped tin oxide (FTO) substrates (Pilkington TEC Glass-TEC 8) were cleaned with a detergent solution and DI water. They were then cleaned in an ultrasonic bath for 15 minutes using an ethanol–acetone solution (v/v ¼ 1/1) and 2-propanol. Finally a treatment of oxygen plasma was administered for a hydrophilic surface. The platinum coated counter electrode was made using a drop-wise method with 20 mM of H₂PtCl₆ solution in isopropanol on a cleaned FTO glass followed by annealing at 450 °C for 1 hour 30 min. In order to inject the electrolyte, a hole was made at the glass substrate of counter electrode side. To introduce an electrolytes spacer for preventing direct contact of electrodes, supporting layer was prepared by mixing dissolved poly vinyl alcohol (PVA) in water (15 wt%) and nanoparticles. At this research, I used ZrO₂, BaSnO₃, Anodic aluminum oxides, and SiO₂ as supporting materials. Subsequently, the mixed paste was coated on the counter electrode using the doctor blade process and annealed at 400 °C for 2 hours to remove the PVA.

To synthesizing the BaSnO₃ nanoparticles, all chemicals were purchased with reagent grade. 0.01mol of SnCl₄·5H₂O and BaCl₂·2H₂O were mixed in H₂O₂ (30wt%) under vigorous stirring. After 2 hours,

introducing citric acid at the batch and 120mL of aqueous NH_4OH was added into the transparent mixing solution. Precipitation was occurred immediately with white powder, and the solution was stirring overnight. After the stirring process, the powder was cleaned by D.I water using centrifuge and dried thoroughly. The precipitated particles were annealed at 900°C for 2 hours in furnace.

In order to fabricating anodic aluminum oxide (AAO), a high purity (99.997%) aluminium foil supplied from Alfa Aesar (USA) was used as the substrate material. The foil was cleaned in acetone and then electrochemically polished in a 1:4 volume mixture of HClO_4 and $\text{CH}_3\text{CH}_2\text{OH}$ by a constant voltage of 20V for 2 min to achieve a mirror finished surface. Two-step anodization was performed using an electrochemical cell equipped with a cooling stage at a temperature of -1°C . The first anodization step was performed under 40V for 6–8 h in 0.3M $\text{H}_2\text{C}_2\text{O}_4$. Afterwards, the formed porous oxide film was chemically removed by a mixture of 6 wt% of H_3PO_4 and 1.8% chromic acid for a minimum of 3–6 h at 75°C . Second anodization is then performed on these samples using the same conditions (0.3M $\text{H}_2\text{C}_2\text{O}_4$) with an anodization time to achieve AAO thickness from 10 to $30\mu\text{m}$.¹⁶⁴⁻¹⁷²

Other supporting materials such as ZrO_3 and SiO_2 was purchased and using without further purification.

Not only to increase the adhesion of the photoanode and supporting layer but also to get a scattering effect, the mixed TiO_2 paste (20 nm/500 nm TiO_2 paste, 1 : 1 vol each CCIC and ENB Korea) was coated onto the supporting layer coated substrate using a doctor blade. The TiO_2 -coated glass was aged at 60°C for 1 hour and annealed at 500°C for 1 hour to create a TiO_2 film with a thickness of 4 μm .

The nanocrystalline TiO_2 paste (20 nm, CCIC) was coated onto the TiO_2 film, aged at 60°C for 1 hour, and annealed at 500°C for 1 hour to create a TiO_2 film with a total thickness of 15 μm . To prepare the conductive oxide layer, indium-doped tin oxide (ITO) layer was sputtered with a thickness of 300 nm (SORONA, SRN-120D, Korea) and annealed at 300°C for 1 hour to increase conductivity and transparency. The stacked up cell was immersed in 0.3 mM $(\text{Bu}_4\text{N})_2[\text{Ru}(\text{dcbpyH})_2(\text{NCS})_2]$ (referred to as N719) dye in a mixture of acetonitrile and tert-butanol solvent (v/v = 1/1) for overnight at room temperature. The dye molecules penetrated along the sides of the device where the porous TiO_2 and supporting layer pave the way for dye molecules. The dye molecules adsorbed on the TiO_2 surface, and the device was sealed with the liquid sealant Amosil 4 (Solaronix). In the conventional DSSCs, the sealant was placed in between the working and counter electrodes and they were sealed with heat and pressure, but in the case of the reverse structure, a thin ITO layer was sputtered on the TiO_2 working electrode; hence the liquid sealant was placed at the edge of the active cell area and completed the sealing process. An electrolyte solution containing a mixture of 0.6 M 1-hexyl-2,3-dimethylimidazolium iodide, 0.1 M Guanidine thiocyanate, 0.03 M iodine, and 0.5 M 4-tert-butylpyridine in acetonitrile was introduced through a drilled hole at the counter electrode, which upon completion was

followed by a sealing process with cover-glass and surlyn.

Fluorine-doped tin oxide substrate was purchased from Pilkington. H_2PtCl_6 , 1-hexyl-2,3-dimethylimidazolium iodide, Guanidine thiocyanate, iodine, 4-tert-butylpyridine, PVA, and SiO_2 were purchased from Sigma-Aldrich. For the photoanode, 20 nm TiO_2 powder and 500 nm TiO_2 powder were from CCIC and ENB Korea respectively. To make the photo-sensitizer, cis-bis(isothiocyanato) bis(2,2',9,9'-bipyridyl-4,4',9,9'-dicarboxylic acid) ruthenium(II) (referred to as N719) were purchased from O'yang industry. All of the reagents were used without further purification. Morphologies and components change as a function of temperature were characterized by thermogravimetric analysis (TGA, TA Instruments) and scanning electron microscopy (Nano230, FEI). The total thickness of reverse structured DSSC (RS-DSSC) was measured using a surface profiler (KLA_Tencor). Atomic force microscope (AFM) images were obtained using a Dimension AFM (Veeco) instrument. The photovoltaic properties of the cell were measured using a Keithley 2400 digital source meter and a solar simulator (AM 1.5G, 100 mW/cm^2 , Sol3A, class AAA, Oriol) as a light source. Impedance spectra were obtained using an electrochemical impedance spectroscopy (EIS) (Solartron 1260 impedance/gain-phase analyzer).

4.4 Result and Discussion

The schematic structures of reversed (RS-DSSC) and conventional DSSCs are presented in figure 4.1. Most of the DSSCs conventionally employ sandwich structures with two electrodes facing each other (Figure 4.1a). Unlike the conventional structures, a RS-DSSC can be fabricated on a Pt-coated counter electrode as substrate from the bottom. Thin supporting layer and TiO_2 photo anode were positioned on the substrate in turn, and the ITO layer was applied as TCO on the top of structures. Not only to prevent direct contact of the electrodes but also electrolyte penetration, porous supporting layer was inserted between the two electrodes.

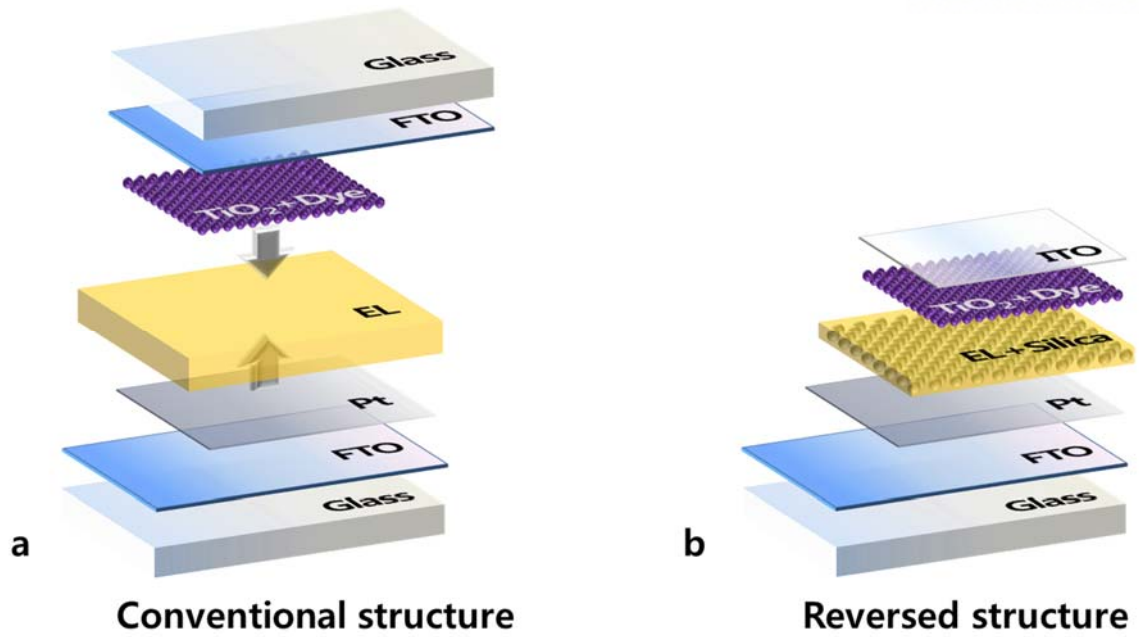


Figure 4.1 Schematic diagrams of conventional and reversed structure of dye-sensitized solar cells.

Figure 4.2 shows the thermogravimetric analysis (TGA) curves of prepared supporting layer paste. Up to 300°C, the TGA shows a gradual curve which indicates that the residues still exist. However, it also shows drastic weight loss starting at 350°C, possibly due to the combustion of PVA. In order to facilitate dye adsorption and electrolyte penetration, the inner pore size should be sufficiently big to avoid the inferior aggregation.

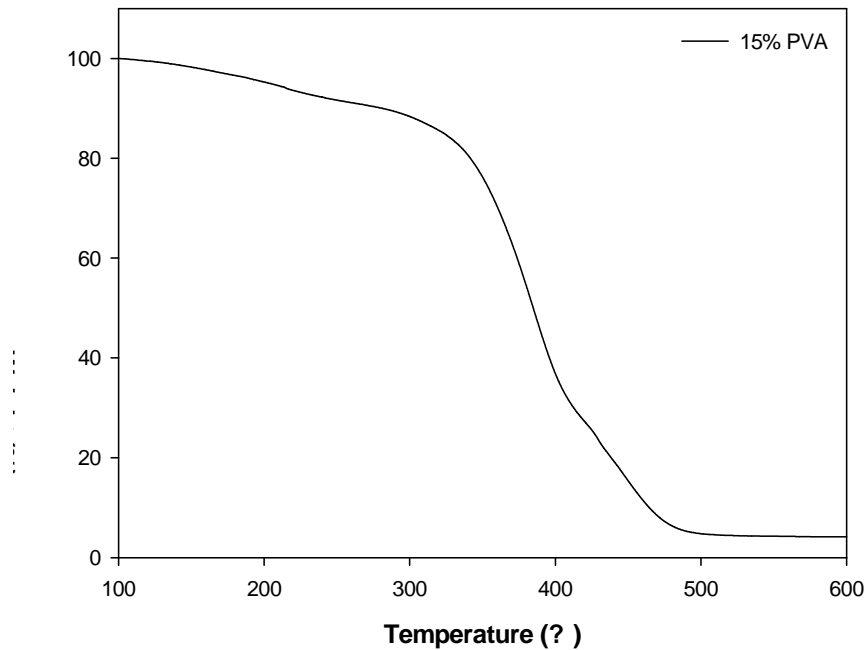


Figure 4.2 Thermogravimetric analysis (TGA) curve of supporting layer with PVA binder.

At this aspect, ZrO_2 was used as the first supporting materials. When using the ZrO_2 as supporting layer, the film morphology and surface flatness was good enough. However the particles are connected too close each other that dye molecules and electrolyte penetration was blocked. ZrO_2 used RS-DSSC shows a short circuit current (J_{sc}) of 16.4 mA/cm^2 , open circuit voltage (V_{oc}) of 0.7 V , fill factor (FF) of 36.6% with power conversion efficiency (η) of 4.1% as shown in figure 4.3 and table 4.1. Even though the high shunt resistance (R_{shunt} , $1.37 \text{ k}\Omega$) and low series resistance (R_{series} , $207.73 \text{ }\Omega$), the electrolyte diffusion process was hindered by densely packed nanoparticles and consequentially the FF of the cell were low.

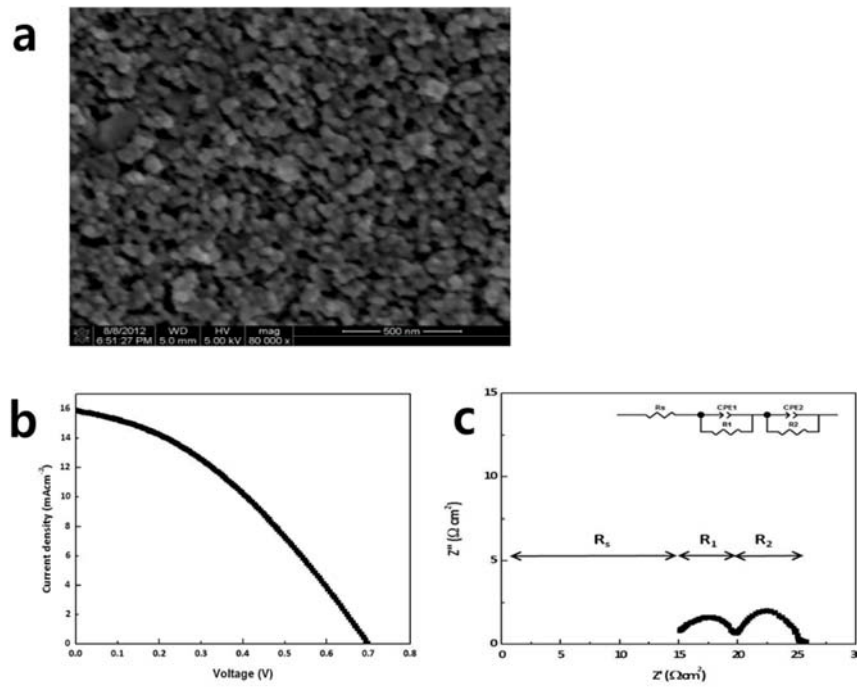


Figure 4.3 (a) Surface morphology of supporting layer using scanning electron microscopy, (b) photocurrent-voltage curve of the reverse structured cell with ZrO_2 , and (c) electrochemical impedance spectroscopy (EIS) of symmetric cell.

Table 4.1 Current-voltage parameters with electrochemical parameters of reverse structured cell using ZrO_2 supporting layer.

	J_{sc} (mA/cm ²)	V_{oc} (V)	FF (%)	Eff (%)	R_{shunt} (Ω)	R_{series} (Ω)
RS-DSSC	16.1	0.70	36.6	4.1	1.37k	207.73

When the ZrO_2 was used as supporting materials, due to the low porosity, electrolyte diffusion was hindered and the efficiency was not comparable. In order to increase an inner pore, synthesized $BaSnO_3$ is investigated as a supporting layer.^{173, 174} The $BaSnO_3$ materials were easily synthesizable and morphological controllable by controlling the temperature and processing time.

Figure 4.4 represents the surface morphology of the synthesized $BaSnO_3$ nanoparticles with various shapes and photographs of its paste form. For sufficient size of inner pore, all the shapes of nanoparticle, nanorod, and nanopillar of $BaSnO_3$ were mixed at one container and using as supporting layer.

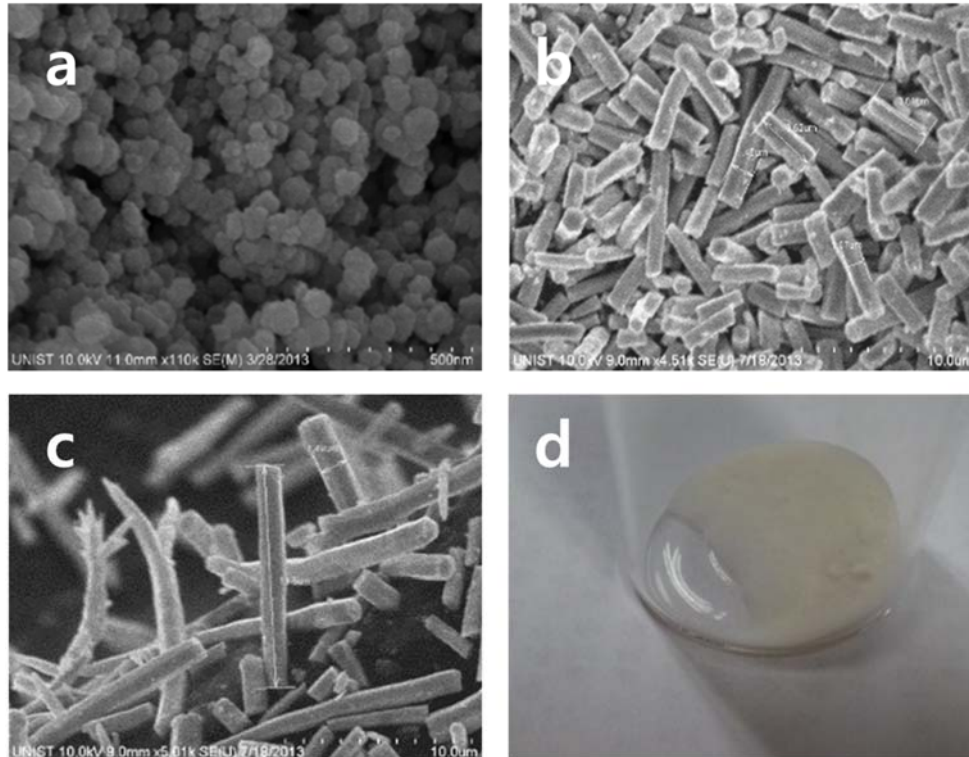


Figure 4.4 SEM images of synthesized BaSnO₃ with (a) sphere, (b) nanorod, and (c) nanopillar. (d) Picture of BaSnO₃ paste for supporting layer. The paste were mixed (a), (b), and (c) with wt% of 50, 1, and 1 respectively.

By using BaSnO₃ as supporting layer, the inner pore was big enough for the dye molecules and electrolytes penetration. However, as can be seen in figure 4.5 and table 4.2, total efficiency and FF of the cell was low. One of the reason for the low parameters can be expected to the conductivity. The BaSnO₃ has a semiconducting properties with perovskite structure and it has somewhat conductivity, thus the electrons could be leaked toward the counter electrode with low shunt resistance. Second assumption of this result is surface flatness. According to the new structure, ITO should be coated on the top layer. However, the mixed BaSnO₃ paste contains nanorod-pillar structure and it should be obstacle of surface flatness at the ITO layer.

Table 4.2 Photovoltaic performance of the RS-DSSC using BaSnO₃ supporting layer

	J_{sc} (mA/cm ²)	V_{oc} (V)	FF (%)	Eff (%)
RS-DSSC	8.1	0.65	30.7	1.4

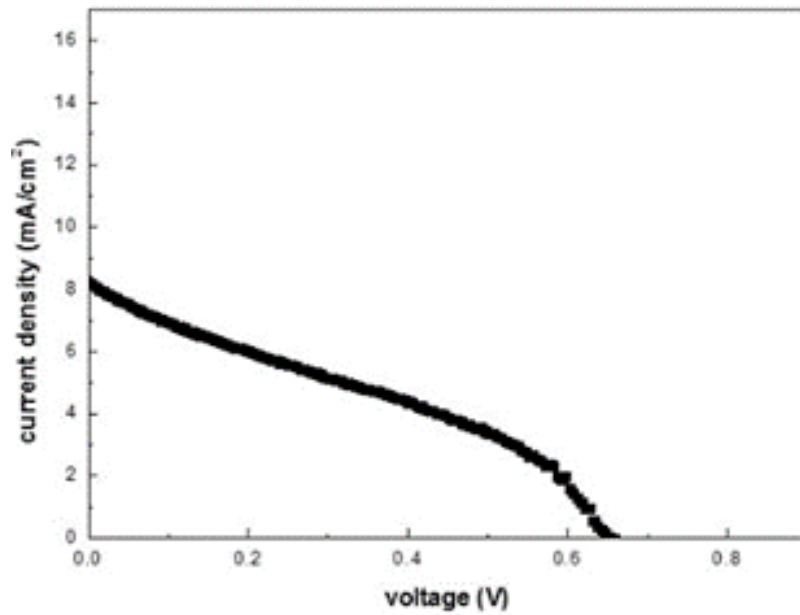


Figure 4.5 photocurrent-voltage curve of the reverse structured cell with BaSnO₃

On that account, the supporting layer should have high inner porosity, low conductivity, and flat surface. Nanostructure materials as anodic aluminum oxide (AAO), a self-ordered nanopore material has been typically used as filters and as templates for fabrication nanowire arrays including DC electrochemical deposition of metallic, magnetic or semiconductor ordered nanowire arrays for application such as field emission devices. At this research, AAO was applied at the system as a supporting layer owing to the nanopore structure, low conductivity and flat-surface. The fabrication of AAO supporting layer is presented in figure 4.6.

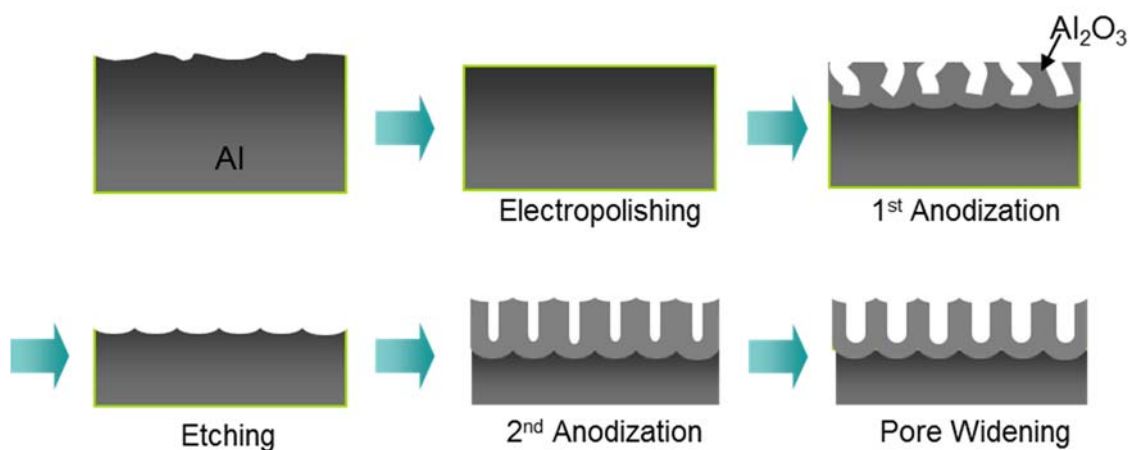


Figure 4.6 Schematic diagram of the fabrication process of AAO templates.

In order to fabricating the AAO membrane, Al film were electro-polished to achieve a flat and clean surface. The polished Al film were electrochemically anodized under specific conditions for the tubular structure. At the first step of anodization, the tubular structure were made with random direction due to the absence of uniformity or direction. After the first anodization, the inner tube were formed irregular direction. However, because of the properties of oxide layer, none-oxidized Al film could get the foot print at the surface of Al-AAO. After the first anodization, the randomly porous oxide layer were chemically removed and second anodization can be performed on the sample. The pore diameter of fabricated AAO membrane could be widened by chemical batch reaction. Figure 4.7a and b shows surface morphologies of the fabricated AAO. a and b show well-ordered nanopore on the flat surface. The AAO membrane could endure high temperature, thus the TiO₂ paste were bladed on the fabricated membrane and heat-treated under 500°C (see figure 4.7.c, d, and e).

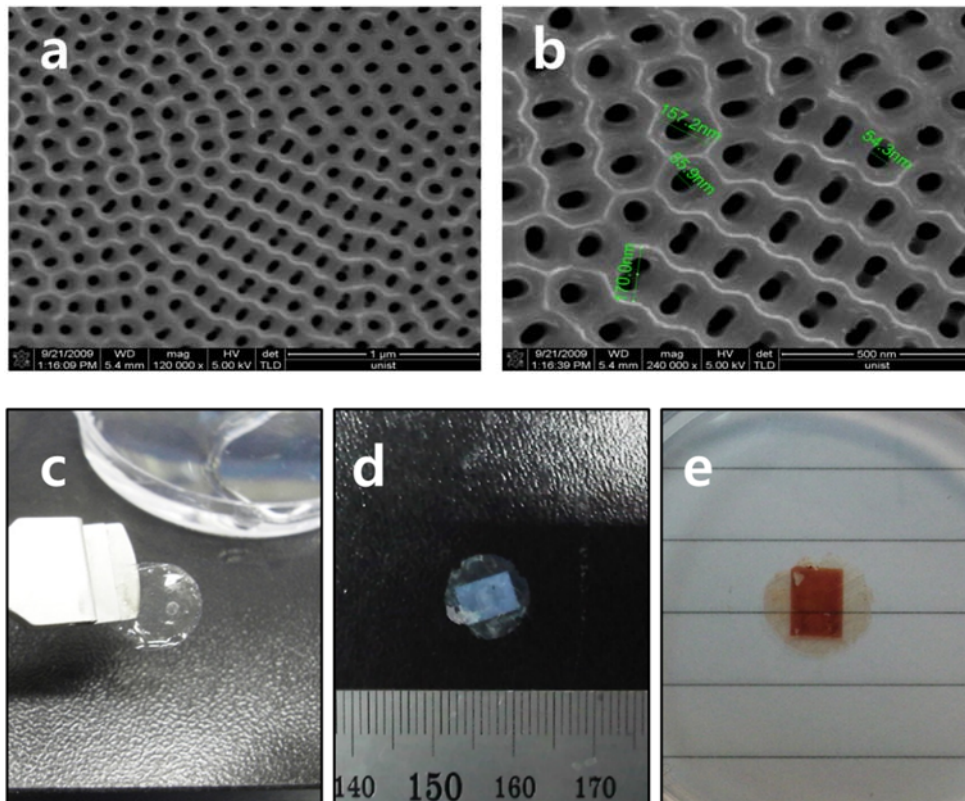


Figure 4.7 a and b represents the morphology of the AAO surface by scanning electron microscopy. c, d, and e show the pictures of AAO film and its application to the DSSC with TiO₂ photoanode.

AAO membrane used RS-DSSC shows a short circuit current (J_{sc}) of 3.9 mA/cm², open circuit voltage (V_{oc}) of 0.67 V, fill factor (FF) of 54.8% with power conversion efficiency (η) of 1.4% as shown in figure 4.8 and table 4.3. Even though the nanopored AAO membrane supporting layer has high surface

flatness and pored structure with low conductivity, the adhesion force with FTO substrate were weak.

Table 4.3 Photovoltaic performance of the RS-DSSC using anodic aluminum oxide (AAO) supporting layer.

	J_{sc} (mA/cm ²)	V_{oc} (V)	FF (%)	Eff (%)
RS-DSSC	3.9	0.67	54.8	1.4

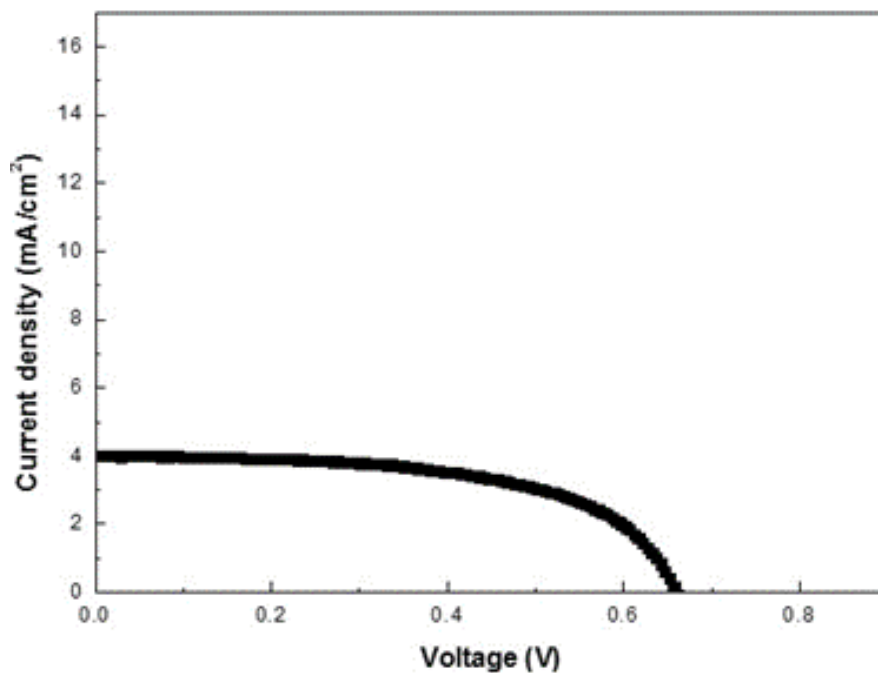


Figure 4.8 photocurrent-voltage curve of the reverse structured cell with anodic aluminum oxide (AAO).

As the last candidate for the supporting layer, 100nm size silica nanoparticles were purchased as powder form and using it without any further purification. The SiO₂ nanoparticles were easily dispersed in the PVA. Figure 4.9 a and b show the morphology of supporting layer investigated using scanning electron microscopy after sintering at 450 °C and 500 °C, respectively. 450 °C sintering shows better surface morphology than 500 °C with inferior aggregation.

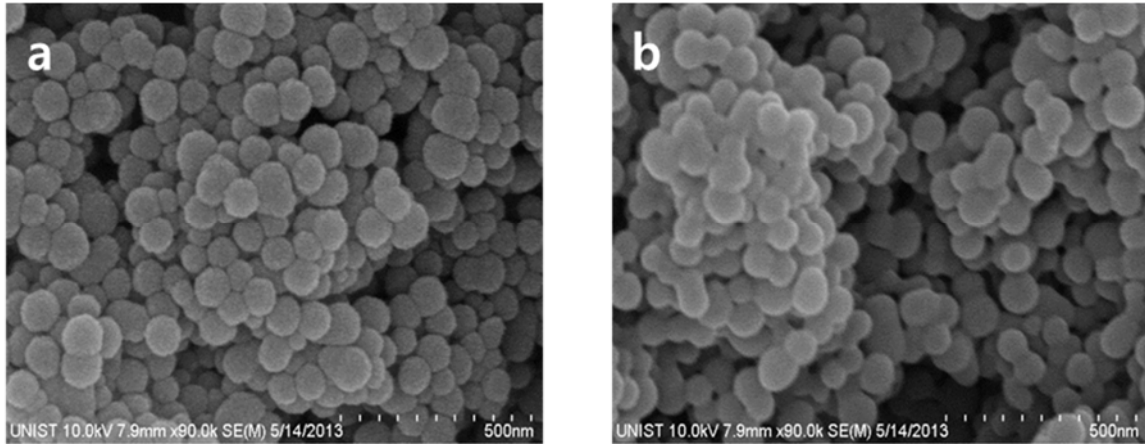


Figure 4.9 Field emission scanning electron microscopy (FE-SEM) images of supporting layer with sintering temperature of (a) 450°C and (b) 500°C.

Figure 4.10 represents the cross sectional morphology of the supporting layer, TiO₂ and ITO layer which were formed in sequence. The supporting layer was made on a Pt coated FTO with an average thickness of 6 μm and 2 different compositions of TiO₂ nanoparticles were pasted. The top part of 20 nm sized TiO₂ nanoparticles with a thickness of 5 μm is the main active layer, while the bottom part of TiO₂ which was mixed 20 nm and 500 nm nanoparticles 4 μm thick improved the adhesion between the supporting and active layer. Not only does the bottom TiO₂ act as an adhesion layer but also as a scattering layer. Even though the bottom part of TiO₂ shows a photosynthesis properties, the surface should be secured the flatness for the sputtered TCO. Figure 4.10.b shows a zoomed view of the ITO. The evaporated ITO formed a continuous thin layer on top of the TiO₂ nanoparticles with a thickness of 200 nm.

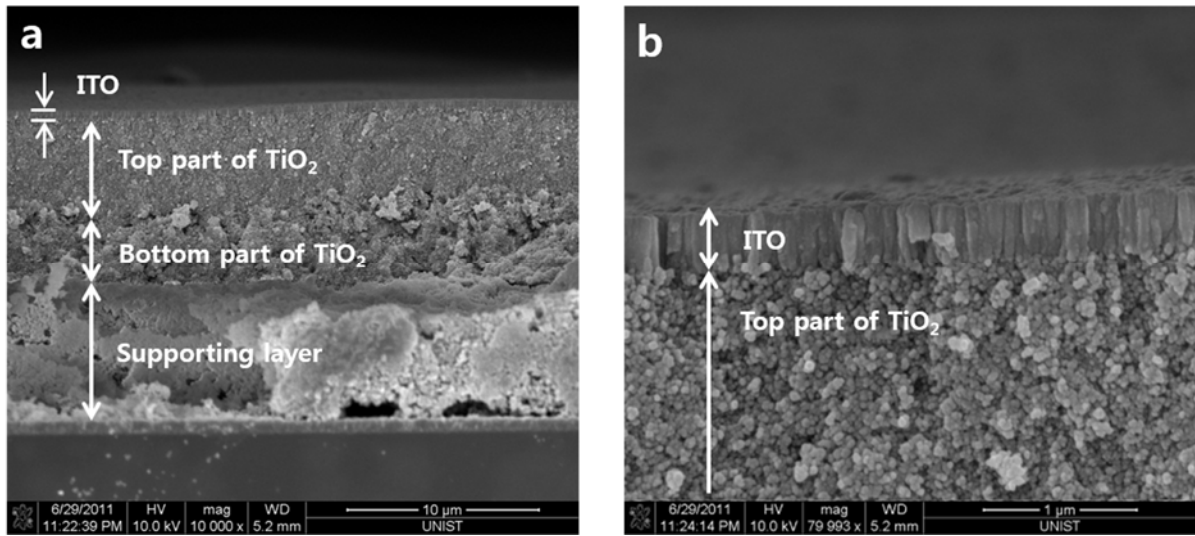


Figure 4.10 Cross-section FE-SEM images of reversed structure of dye-sensitized solar cell.

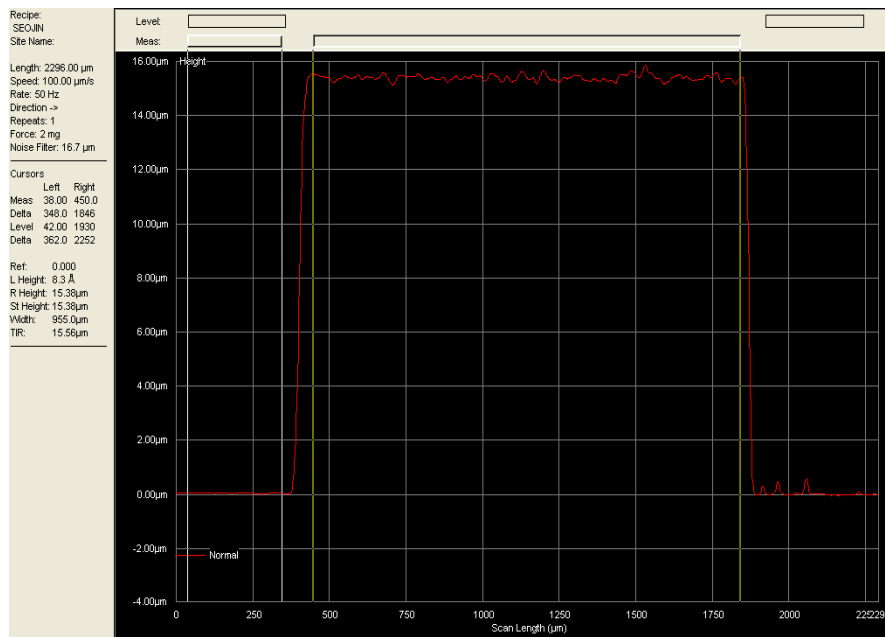


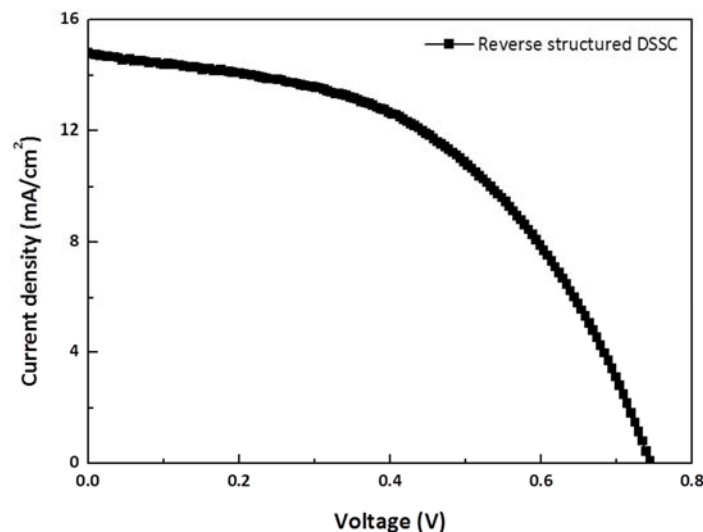
Figure 4.11 Surface profilometer measurement of RS-DSSC.

In order to check the film thickness and surface flatness, surface profilometer (P-6, KLA-Tencor) were used. At the figure 4.11, surface profilometer (Alpha step) measurement shows that the total thickness of RS-DSSCs from TCO glass to ITO layer is about 15 µm.

A complete RS-DSSC shows a short circuit current density (J_{sc}) of 14.8 mA/cm², open circuit voltage (V_{oc}) of 0.81 V, fill factor (FF) of 49.4% with power conversion efficiency (η) of 5.4% as shown in

figure 4.12. It is well known that the short-circuit current density is mainly determined by the transfer of total number of photo-generated electrons to the electrode. Although the ITO layer was sputtered onto the TiO₂, the observed results indicate that the RS-DSSC shows quite comparable values of J_{sc} to the conventional structure. However, the FF value is quite lower than the conventional structures. The J–V curve informs that the device has high series resistance and low shunt resistance. Since the ITO layer is prepared on rough TiO₂ nanoparticles, its conductivity through lateral direction might exist. In addition, the contact between ITO and TiO₂ nanoparticles needs to be investigated. Shunt resistance might be from ITO floating or TiO₂ nanoparticle penetration through supporting layer, which can cause shorts.

The chemical reactions of dye sensitized solar cells are commonly known by the researchers in this field. Here, even though we introduce a new supporting layer for the reversed form, the chemical reaction was not changed at the full circuit of DSSCs. Supporting layer was chemically stable and not react with the chemical molecules such as dye, iodine, and Pt. The electrochemical properties should be issued for this kind of concept, because the electrical resistance or electron kinetics can be varied through the influence of structure. In addition, in order to check the electron kinetics and investigate the interfacial properties,¹⁷⁵ electrochemical impedance spectroscopy (EIS) was employed which was performed under AM 1.5 front side illumination in an open-circuit voltage condition. Figure 4.13 shows the measured EIS and the fitting parameters for the impedance spectroscopy of RS-DSSC were summarized in Table 4.4.



J_{sc} (mA/cm ²)	V_{oc} (V)	FF (%)	η (%)	R_{sh} (Ω)	R_s (Ω)
14.8	0.744	49.4	5.4	2.14k	131.9

Figure 4.12 Photocurrent-voltage curve of the reverse structured cell.

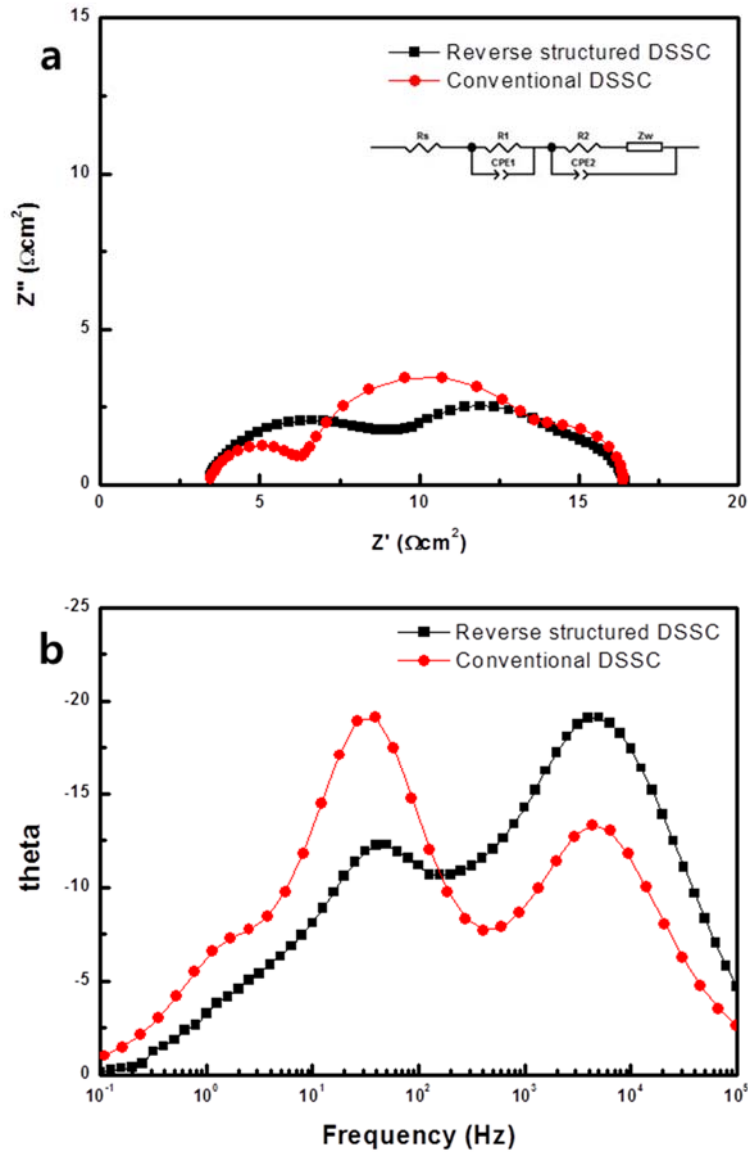


Figure 4.13 (a) Nyquist plot and (b) Bode phase plot of the electrochemical impedance spectroscopy of reverse structured DSSC. The equivalent circuit of the device is shown in the inset of (a).

The equivalent circuit of this type of cell is described in the inset of Figure 4.13.a. R_s , CPE, R_1 and R_2 represent series resistance in high frequency region, constant phase element which was equivalent electrical circuit component, and resistances respectively. In figure 4.13.a, the first semicircle at the high frequency is ascribed to the charge transfer at the interface between the counter electrode and

electrolyte, and the third semicircle is attributed mainly to the Nernst diffusion of I_3 within the electrolyte (R_{diff}). At the RS-DSSC structure, the supporting layer should be placed onto the Pt electrodes not only to make a room for electrolytes but also to form the photo-electrodes. Due to the direct contact of porous supporting layer and Pt electrode, the interface resistance can makes the larger first semicircle at the high frequency region than that of the conventional cells. Thus, the corresponding charge transfer resistance of RS-DSSC and conventional cells is $5.4 \Omega/cm^2$ and $3.1 \Omega/cm^2$ respectively. However, the charge transfer resistance of the RS-DSSC in the intermediate frequency region (R_{ct2}) and the low frequency region (R_{diff}) has the value of $6.1 \Omega/cm^2$ and $1.5 \Omega/cm^2$ respectively. These values are comparable to that of the conventional DSSC having R_{ct2} of $7.0 \Omega/cm^2$ and R_{diff} of $2.0 \Omega/cm^2$ and their semicircles are more or less similar in shape. These results were also supported by the Bode plots in figure 4.13.b. The fitted Bode plots display the frequency peaks of the various charge transfer processes at different interfaces. The electron recombination time could be calculated by $\tau_r = 1/(2\pi f_{max})$ equation, where f_{max} corresponds to the highest frequency value of the peak in the bode plot. The RS-DSSC and conventional cells gave the f_{max} value of 39.81 Hz and 39.26 Hz respectively and the corresponding τ_r value was calculated as 4.0 ms for the RS-DSSC and 4.05 ms for the conventional cell. The τ_r in RSDSSC is quite competitive with the conventional cell.

Table 4.4 Electrochemical impedance parameters of reverse structured cell

	R_{shunt}	R_{series}	R_s	R_{ct1}	R_{ct2}	R_{diff}	f_{max}
RS-DSSC	2.14k	131.9	3.4	5.4	6.1	1.5	50.1

To fabricate series connected tandem solar cell, I introduced an organic solar cells with inverted structure. The schematic structure of series connected tandem solar cell is presented in figure 4.14 (a) and a picture of the cell is shown in figure 4.14 (b). Using inverted organic solar cell (OSC) as upper cell, I stacked up onto the bottom cell which was made as reversely structured DSSC. At the OSC, the photo excited electrons go to the ITO side. At the RS-DSSC, sputtered ITO were connected to the PEDOT:PSS of OSC in order to make the series connected circuit. Photo-excited electrons of DSSC flow to the PEDOT:PSS and the hole of OSC successfully flow out. Besides, the electrons of OSC could extracted efficiently through the ITO substrate. Holes of DSSC could also be extracted through the Pt coated FTO substrate and whole circuit works in a series connection.

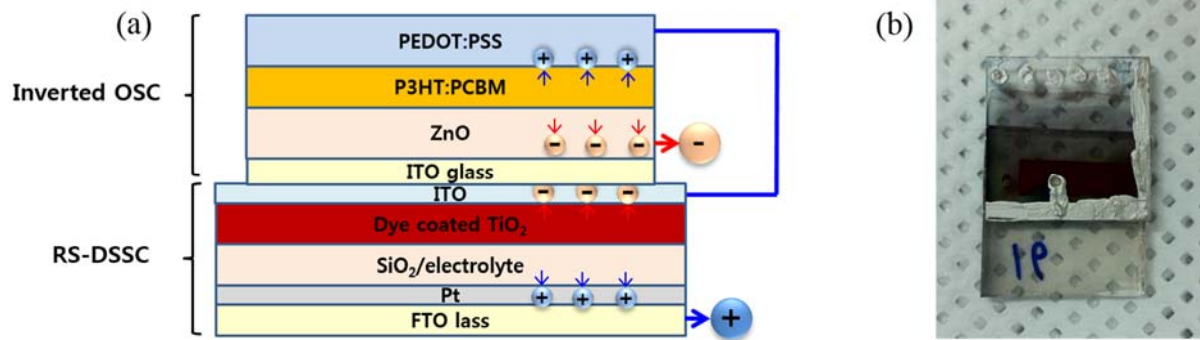


Figure 4.14. Schematic structure of the series connected tandem solar cell (a) and picture of the cell (b).

The photovoltaic parameters of series connected tandem cell and each single cells were extracted from the J-V curves in figure 4.15 and the cell performance parameters are summarized in table 4.5 Due to the properties of series connected tandem cell, the V_{oc} value was successfully increased over 1.2V. A single cell of inverted OSC shows J_{sc} of 5.6 mA/cm², V_{oc} of 0.551 V, FF of 0.415 with Eff of 1.3%. Another single cell of un-modified RS-DSSC shows J_{sc} , V_{oc} , FF and Eff values of 6.3 mA/cm², 0.647 V, 50.7 and 2.1% respectively. The series connected tandem cell showed a higher photovoltage of 1.21V with the conversion efficiency of 4.1%. Even though the cell performance was not good enough, this observation confirms that the suggested tandem system could be possible.

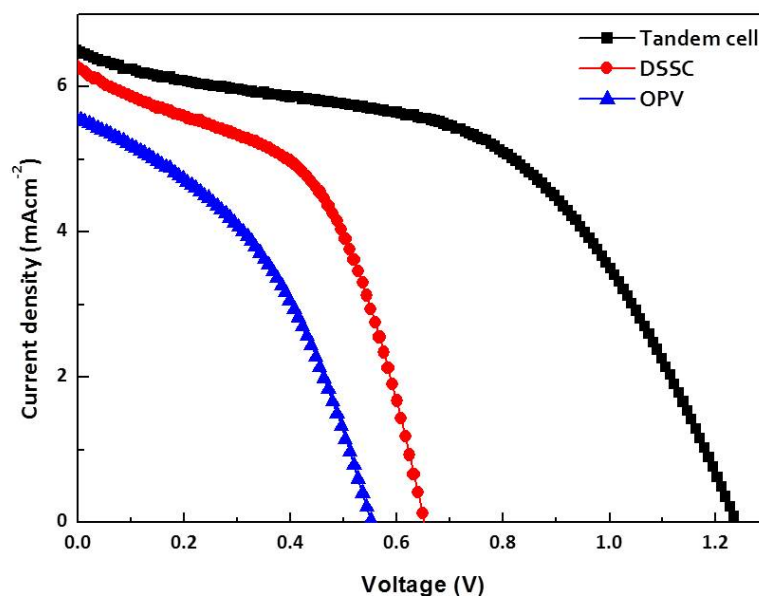


Figure 4.15. Photocurrent-voltage curves of the inverted OSC (single cell, blue triangle), RS-DSSC

(single cell, red circle), and series tandem cell (black square).

Table 4.5. Photovoltaic performances of the single cells and series connected tandem cell.

	S-Tandem	RS-DSSC	Inverted-OSC
V_{oc} (V)	1.2	0.647	0.551
J_{sc} (mA/cm ²)	6.5	6.3	5.6
FF (%)	50.7	50.8	41.5
η (%)	4.1	2.1	1.3
R_{shunt} (ohm)	1.96k	1.30k	1.59k
R_{series} (ohm)	319.29	164.11	236.58

4.5 Conclusion

In summary, I have successfully fabricated RS-DSSC onto one substrate by controlling each layer. Even though the nanoparticle beads have incorporated in the reversely assembled structure, dye and electrolytes molecules could penetrate into the inner pore and a power conversion efficiency of 5.4% was achieved for the RS-DSSC with a similar J_{sc} and V_{oc} values as of the conventional DSSCs. The interfacial properties and each electrochemical impedance parameters of RS-DSSC is comparable to the conventional DSSCs in order to convince the concept. Finally, this technique could be extended to produce devices in research, including a flexible or a tandem solar cell with other thin film solar cells such as Cu(In, Ga)Se₂ (CIGS) or organic photovoltaic devices.

Chapter 5. A study of TiO₂/carbon black composition as counter electrode materials for dye-sensitized solar cells

This chapter reproduced with permission from J. Lim, et al, Nanoscale Research Letters, 2013, 3, 227,

Copyright 2014 Springer Open Journal.

5.1 Background and introduction

Dye-sensitized solar cells (DSSCs) have attracted considerable attention as a viable alternative to conventional silicon-based photovoltaic cells⁵ because of their high conversion efficiency, environmental friendliness, low-production cost, and easy fabrication procedure.^{24, 35, 154, 176} A typical DSSC is comprised of a nanocrystalline semiconductor (TiO₂), redox mediator (I₃⁻/I⁻), and a counter electrode (CE) to collect the electrons and catalyze the redox couple regeneration.¹⁷⁷ Extensive researches have been conducted in order for each component to achieve highly efficient DSSCs with a modified TiO₂,¹⁷⁷ alternative materials,^{178, 179} and various structures.¹⁸⁰⁻¹⁸² Usually, Pt-coated fluorine-doped tin oxide (FTO) is used as a counter electrode owing to its superior catalytic activity.¹⁸³ However, there are researches reporting that Pt corrodes in an electrolyte containing iodide to generate PtI₄.^{33, 34} Besides, large solar module systems will benefit from materials that are abundantly available with high chemical stability. Therefore, it is necessary to develop alternative materials which must be inert and show good catalytic effect in the electrolyte.

A great deal of effort has been taken to replace the expensive Pt material with other cost effective materials such as cobalt sulfide (CoS),⁷⁰ titanium nitrides (TiN),¹⁸⁴⁻¹⁸⁶ and carbon derivatives.^{150, 187-189} Among these candidates, due to their low cost, abundance, and high catalytic activities with chemical stability against I₃⁻/I⁻ redox couples, cost effective carbon materials obtain increasing attention.¹⁹⁰⁻¹⁹³

Here, I focus on carbon black which is produced by combustion of heavy petroleum products with high surface areas. Compared to any other forms of carbon derivatives, carbon black does not require a delicate process to apply to counter electrodes. Note that carbon nanotubes and nanorods require multiple operations for the synthesis and application on counter electrode substrates. In this work, I demonstrate the properties of carbon black material with anatase TiO₂ in an attempt to replace the Pt counter electrode in DSSC applications. Forty-nanometer-sized TiO₂ nanoparticles were tested with various weight ratios of carbon black, and the effect was investigated by electrochemical impedance

spectroscopy and cyclic voltammetry analysis in detail.

5.2 Experimental

Carbon black

The carbon black chunk was purchased from Sigma- Aldrich (14029-U, St. Louis, MO, USA) and ground to make powder. Pulverized carbon black was sifted out with 80-unit mesh then annealed for 2 h at 500°C in a muffle furnace. The annealed carbon mass was ground again and passed through with 200- to 350-unit mesh for further heat treatment at 300°C for 2 h in order to remove the impurities. The final carbon black powder size was 80 nm.

Anatase TiO₂ nanocrystal synthesis

Titanium dioxide nanoparticles in anatase crystal form were synthesized by a modified Burnside method.¹⁹⁴ A 162-mL titanium (IV) isopropoxide (0.5 M, Sigma- Aldrich) was rapidly injected into 290 mL of distilled water (15.5 mol, J. T Baker, Avantor Performance Materials, Center Valley, PA, USA) under stirring, and the solution was vigorously stirred for a further 10 h. Addition of titanium (IV) isopropoxide in such an aqueous solution results in a white precipitate in the TiO_x form. The resultant colloid was filtered and washed thrice with 50 mL of deionized (DI) water. Then the filtrate was loaded into an autoclave with 30 mL of a 0.6 M tetramethylammonium hydroxide solution to form a white slurry. The pH of the colloidal solution after addition of the base was measured to be between 7 to approximately 8. The solution was heated to 120°C for 6 h in order to obtain a peptization, and then the peptized suspension was treated hydrothermally in the autoclave at a temperature range of 200, 220, and 240°C for 4.5 h. The colloids were centrifuged at 13,000 rpm for 40 min and the precipitate was dried for 1 day in a vacuum oven, then dissolved into the DI water (wt.% of DI water/TiO₂ = 20:1). Then, a clear white color precipitate was observed.

TiO₂/carbon black slurry preparation

The TiO₂ and carbon black (T/CB) slurry was prepared as follows: various amounts of carbon black powder (50, 100, 200, and 500 mg) were mixed with 40nm sizes of TiO₂ nanoparticles in various weight ratios (T/CB; 10:1, 5:1, 2.5:1, and 1:1). The mixture was dispersed by ultra-sonication (750 W, Sonics & Materials, Inc, Newtown, CT, USA) for 10 min. After the ultrasonic treatment, 100 µl of Triton X-100 (Sigma-Aldrich) was added to the mixture and further ultrasonic treatment was carried for 10 min.

Electrodes and cell fabrication

To clean a substrate, fluorine doped tin oxide substrate (Nippon Sheet Glass Co., Ltd, Pilkington TEC Glass-TEC) were washed in a detergent solution, DI water, an ethanol-acetone mixture solution (v/v=1/1), and 2-propanol in an ultrasonic bath for 10 min. Finally a treatment of UV-O₃ for 15 min to introduce a hydrophilic surface. Nanocrystalline TiO₂ paste (20 nm, ENB-Korea) was coated onto the

cleaned FTO glasses using a doctor blading method. The TiO₂-coated FTO glasses were aged at 60 °C for 1 h and annealed at 500 °C for 1 h to create a TiO₂ film. After the heat treatment, the substrate was immersed in 40 mM of an aqueous solution of TiCl₄ at 80°C for 30 min and rinsed with DI water and an ethanol-acetonitrile mixture solution (v/v = 1/1); this substrate were annealed again at 500°C for 1.5 h. After cooled it down, the TiO₂ coated substrate were immersed in 0.3mM (Bu₄N)₂[Ru(dcbpyH)₂(NCS)₂] (referred to as N719) dye in a mixture of acetonitrile and tert-butanol solvent (v/v = 1/1) with 0.075mM co-adsorption of dioneohexyl bis-(3,3-dimethyl-butyl)-phosphinic acid (DINHOP) for overnight at room temperature. To prepare counter electrodes, a 10mM H₂PtCl₆ solution in ethanol and T/CB slurry of various weight ratios were coated onto a cleaned FTO glass separately, followed by annealing at 500°C for 1 h in a tube furnace. The working electrode and the counter electrode were sandwiched together using a 50-μm thick Surlyn (DuPont) at 100°C for 10 s. An electrolyte containing a mixture of 0.6 M 1-hexyl-2,3-dimethyl-imidazolium iodide, 0.1 M guanidine thiocyanate, 0.03 M iodine, and 0.5 M 4-tert-butylpyridine in acetonitrile was injected, and final sealing completed the fabrication of the cell.

Characterization of dye-sensitized solar cell

In order to check the structure and properties of synthesized materials, X-ray diffraction (Normal XRD, Bruker), scanning electron microscopy (FE-SEM, Nano230, FEI co.), and thermogravimetric analysis (TGA, TA Instruments) were checked.

Photocurrent-voltage (J-V) curves of DSSCs were obtained by current-voltage characteristics measurements under AM 1.5G light of 100 mW/cm² (Oriel, Sol3A, class AAA). The intensity of the light was calibrated to 1 sun using a standard single crystalline Si-reference cell (PV Measurements, Inc.). The photovoltaic performance has been characterized by the V_{oc} , J_{sc} , fill factor (FF), and overall efficiency (η) values obtained from the J-V curve. Electrochemical impedance spectroscopy (EIS) and cyclic voltammogram (CV) were measured by electrochemical station (Solartron 1260 impedance/gain-phase analyzer).

5.3 Result and Discussion

As commonly, hydrothermally synthesized nanocrystalline TiO₂ shows anatase structure with good electrical properties and adhesion force to FTO substrate. In this work, I synthesized various TiO₂ materials with various hydrothermal temperature. In order to check the structure and properties, all the materials of synthesized TiO₂ was analyzed by X-ray diffraction (XRD) measurement and shown in figure 5.1.

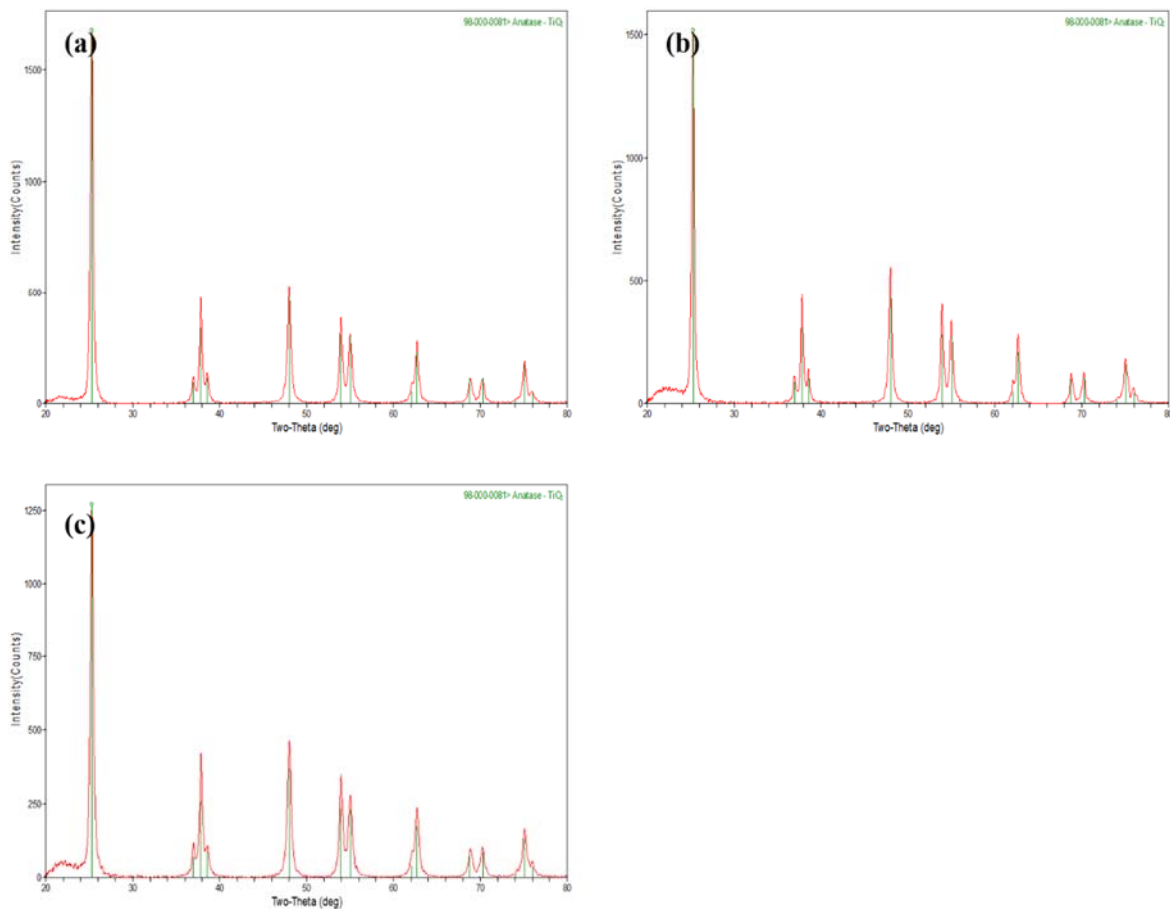


Figure 5.1. X-ray diffraction (XRD) patterns of synthesized TiO₂ particles. Autoclave temperature of (a) 200 °C, (b) 220 °C, and (c) 240 °C

Table 5.1 Synthesized TiO₂ size difference between autoclaving temperature with 200 °C, 220 °C, and 240 °C.

Autoclaving temp. (°C)	200	220	240
Particle size (nm)	30~35	40~45	50~55

These XRD patterns which were synthesized with different temperature from 200 °C to 240 °C show the different size of particles (see table 5.1). The peak intensity does not represent to the crystallites. These XRD patterns are perfectly matched to the anatase structured TiO₂ XRD peak and the rutile TiO₂ peak was not observed.

Burnside et al. reported that the different size of TiO₂ shows different electrical properties and surface statement¹⁹⁴. Even though the smaller particle has the better electrical properties than bigger particle, modification of thickness and maintaining high porosity condition is difficult. However, larger TiO₂

particle can easily organize stable and thick porous structure, less electrical properties it has. For this reason, I choose the size of 40nm particles for this experiment.

Figure 5.2 (a) represents surface morphologies of the grinded carbon black and the (b) synthesized TiO_2 nanoparticles. The sizes of these materials are 75 and 40 nm, respectively. The synthesized TiO_2 particles can easily be attached onto the substrate at 40nm size, and carbon black has a lot of active sites for catalysis with high porosity at approximately 75nm size. I introduced the mixture of both materials as a counter electrode.

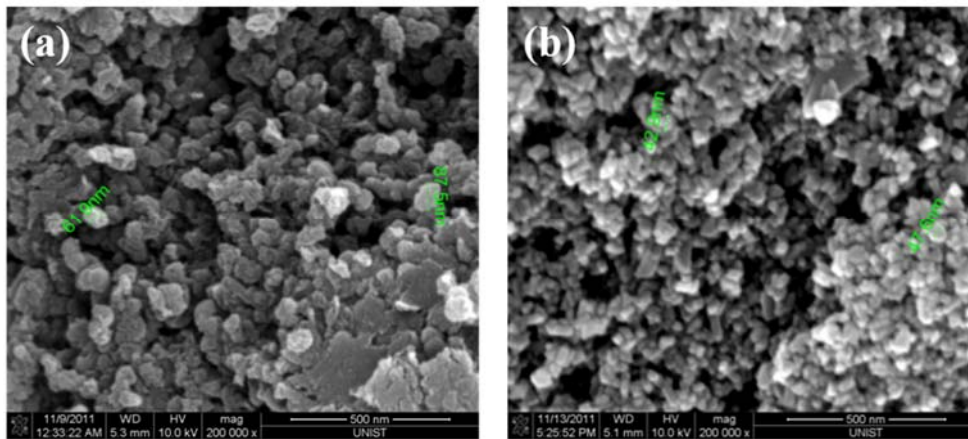


Figure 5.2 FE-SEM image of the (a) carbon black powder and (b) hydrothermally synthesized TiO_2 nanoparticles.

A thermogravimetric analysis (TGA) of carbon black under air and argon atmosphere are shown in figure 5.3. Until the temperature reaches at 350°C , weight of those samples show a very similar decrease for both atmosphere, which indicates that any organic residue on the surface evaporates. However, after the temperature of 350°C , passively due to the combustion, the carbon black in air condition showed drastic weight loss. Contrastively, in the argon atmosphere sample showed no noticeable weight loss until approximately 650°C . To avoid degradation, the temperature of thermal process was set at 500°C and an argon atmosphere was used and to remove all residues in the carbon black and improve the contact of TiO_2 .

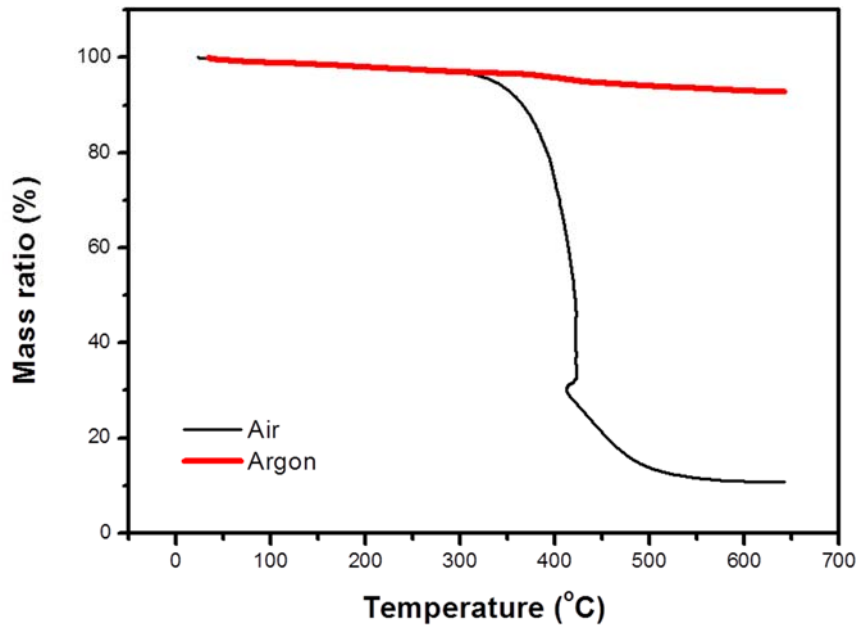


Figure 5.3 TGA in air and argon with the carbon black at a heating rate of 10°C/min.

For the counter electrode, the ratios of T/CB slurry were varied from 10:1, 5:1, and 2.5:1 and 1:1 weight ratio. Figure 5.4 and table 5.2 show the J-V curves for each ratio of T/CB counter electrode and the performance of these cells respectively. The reference Pt counter electrode cell shows 7.7% efficiency (η) with a 69.3% fill factor (FF), and the 5:1 ratio sample shows similar efficiency (7.4%) with a comparable FF (67.4%) and short-circuit current (J_{sc}) (15.5 mA/cm²). T/CB slurry counter electrode samples show similar open-circuit potential (V_{oc}) and FF, but the J_{sc} are much lower than the Pt or 5:1 ratio cases. When the amount of carbon black is low (10:1 ratio), the adhesion of T/CB slurry to the FTO is better. However, reduction of triiodide is not active due to the low surface area available for I₃⁻ reduction and it shows slightly lower J_{sc} than the 5:1 ratio sample. A large amount of carbon black (2.5:1, 1:1 ratios) has enough surface area of reduction, but the poor adhesion of FTO and carbon black makes it difficult to get high efficiency.^{34, 193, 195}

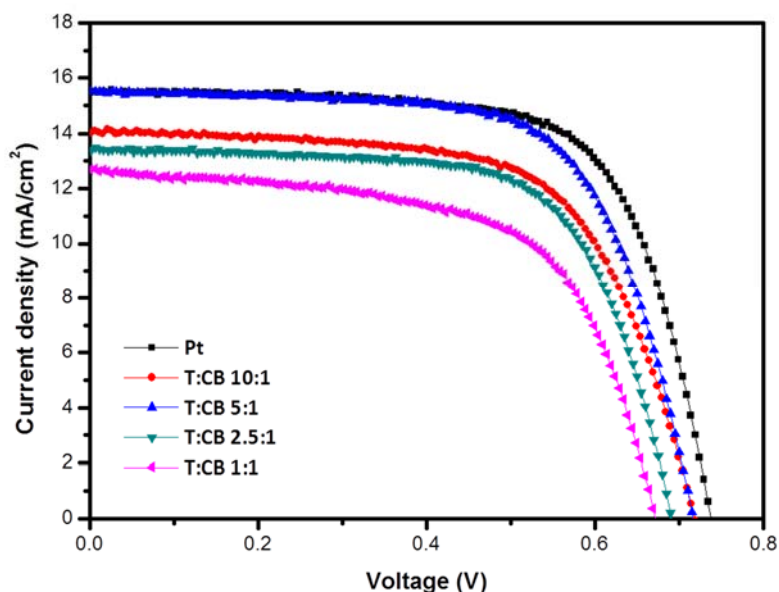


Figure 5.4 Photocurrent-voltage curves of the devices.

Table 5.2 Photovoltaic performance of Pt and TiO₂/carbon black composites as counter electrode

Composite	J_{sc} (mA/cm ²)	V_{oc} (V)	FF (%)	Eff (%)
Pt	15.5	0.73	69.3	7.7
T/CB (1:1)	12.6	0.66	61.3	5.1
T/CB (2.5:1)	13.5	0.69	68.7	6.5
T/CB (5:1)	15.5	0.71	67.4	7.4
T/CB (10:1)	14.1	0.71	64.6	6.6

To examine the interfacial electrochemical properties with ratios of T/CB, electrochemical impedance spectroscopies (EIS) of a symmetrical cell were analyzed. The Nyquist plots of symmetric cells with T/CB slurry ratios of 1:1, 2.5:1, 5:1, 10:1, and a conventional Pt-coated counter electrode are shown in figure 5.5. The first semicircle of the Pt-coated electrodes appears at 100,000 to approximately 100 Hz with only one spectrum of Pt electrode / electrolyte interface. Under 100 Hz, due to the electrolyte diffusion, Warburg impedance was obtained in the symmetric cell. For the T/CB counter electrodes, impedance spectra exhibit three separated semicircles, which correspond to resistances at the counter electrode/electrolyte interface R_{ct} , the TiO₂/carbon black interface, and the electrolyte diffusion Z_w .¹⁹⁶ The amount of carbon content is directly related to the R_{ct} value in turn of the number of catalytic sites.

On this account, the higher amount of carbon content should lead to the lower R_{ct} value.

Due to many catalytic sites for the reduction reaction, the R_{ct} value of T/CB = 5:1 composite shows lower than the T/CB = 10:1. The composites T/CB = 2.5:1 and T/CB = 1:1 have even more amount of carbon content than the other two composites (T/CB = 10:1 and T/CB = 5:1 ratios), however, it showed higher R_{ct} value than the T/CB = 5:1 due to their poor interconnection between TiO_2 and CB as well as the poor adherence property with the FTO surface. At the EIS, the electrolyte diffusion semicircle has a similar shape for all the T/CB composite cells because the diffusion in the electrolyte is unchangeable with the catalytic activity of the counter electrodes.

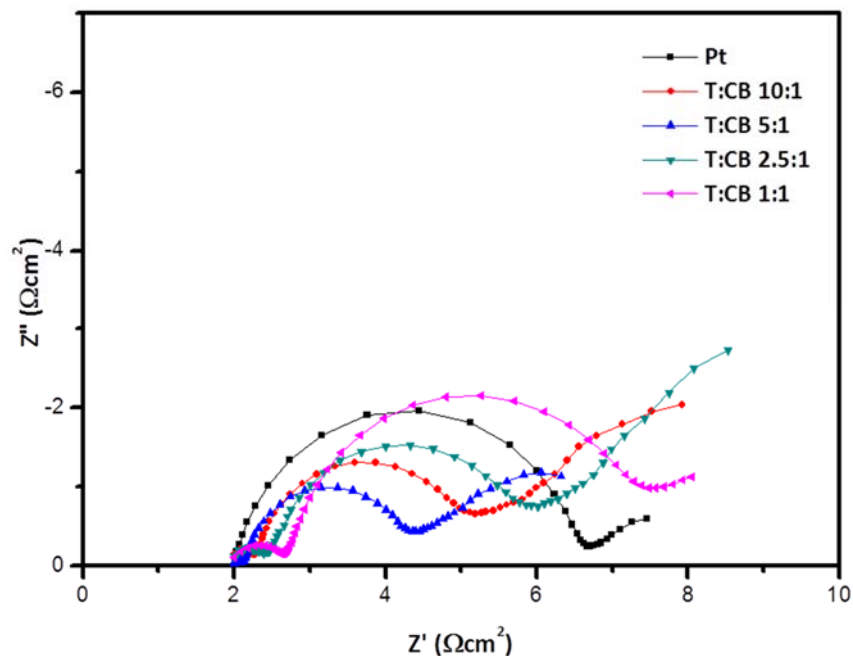


Figure 5.5 Nyquist plot of Pt reference cell and four different ratios of T/CB symmetrical cells.

To further elucidate the electrochemical properties, the best-performing counter electrode cell (T/CB = 5:1) were investigated by a 3 electrodes cyclic voltammetry (CV) test with a scan rate of 50 mV/s. At the 3 electrodes system, the best performed T/CB composite electrode, Pt gauze and Ag/AgCl reference electrode were used as working, counter, and reference electrode respectively. As shown in figure 5.6, the counter electrodes based on the Pt and best-performing T/CB composites show similar shapes in terms of redox peak position. In the CV data, two pairs of redox peaks were obtained. The positive side, known as anodic, refers to the oxidation of iodide and triiodide, and the negative (cathodic) side refers to the reduction of triiodide. The reduction/oxidation peaks for the Pt and the T/CB composites are

shown at -0.224 V/ 0.163 V and -0.394 V/ 0.333 V, respectively. Due to the R_{ct} between carbon black and electrolyte, the small degree of shift could be occurred. However, the T/CB composites exhibited comparable current density with the Pt electrode, and it indicates that the T/CB composites have higher intrinsic catalytic activity for redox reaction of iodide ions.

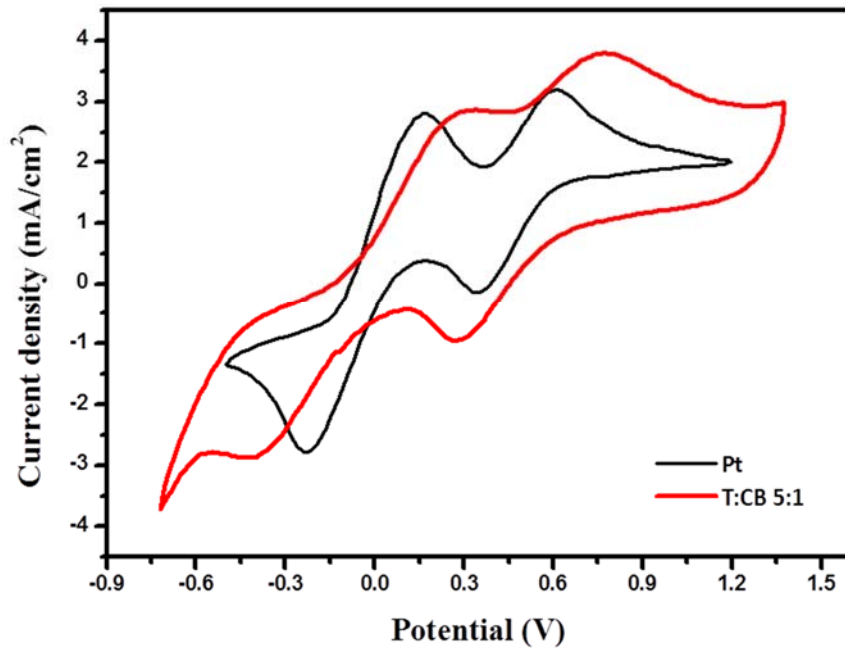


Figure 5.6 Cyclic voltammograms of Pt reference cell and optimized T/CB cell.

Finally, it should be noted that a key advance in this study is the integration of high-quality DSSC counter electrode device design for the reduction of triiodide in the DSSC system.

By using many techniques such as photocurrent-voltage analysis, CV, and EIS, I could confirm the excellent catalytic activities of the synthesized and optimized TiO_2 /carbon black composites, which are comparable to that of the Pt counter electrode.

5.4 Conclusion

In summary, I have been successfully made a cost effective counter electrode with carbon black. Different weight ratios of carbon black containing TiO_2 composites have been tested as the counter electrode material in order to analyze the catalytic performance of triiodide reduction reaction and finally, composites made of carbon black with hydrothermally synthesized 40-nm TiO_2 nanoparticles were used as catalyst of counter electrode.

The best performed condition at a ratio of TiO_2 and carbon black = 5:1 showed the overall efficiency of 7.4% while the well-known Pt counter electrode at the same condition shows 7.7% efficiency. The fill factors found to be around 68% which were strongly dependent on the loading amount of the carbon black powder. The fill factors were strongly dependent on the loading of the carbon black powder and found to be around 68%. Interfacial charge transfer and mass transport were characterized by cyclic voltammetry and electrochemical impedance spectroscopy. This technique of synthesizing nanostructures for high surface area along with optimum carbon black loading afforded an effective and simple way to replace the Pt-based counter electrode for DSSC. Overall, the TiO_2 /carbon black-based DSSC showed excellent cell efficiency that rivals cells with a Pt-based CE and exhibited remarkable electro catalytic activity. This work provides an intriguing way of structurally designing a low-cost, Pt-free, high-performance CE material for DSSCs.

Chapter 6. Cost-effective counter electrode of dye sensitized solar cells with carbon-coated silicon nanowires

This chapter submitted to ACS journal

6.1 Background and introduction

In this experiment, I present a unique process for fabricating carbon-covered silicon nanowires by chemical vapor deposition. Moreover, this study describes a systematic approach of carbon deposited silicon nanowire with respect to the loading amount in order to optimize the catalytic ability of tri iodide reduction for dye-sensitized solar cells. In order to replace the expensive Pt material with other cost effective counter electrode materials, vertically aligned silicon nanowire and deposited carbon was used. Changes in the electrical and morphological properties of the substrates have been studied using scanning electron microscopy, transmission electron microscopy, and Raman spectrometer. In particular, by using a cost effective counter electrode which was made by vertically aligned silicon nanowire and carbon catalyst, I obtained an energy conversion efficiency of 9.22% with a 5 minute carbon deposition Silicon nanowire sample. Electrochemical impedance spectroscopy and cyclic voltammetry studies were characterized.

6.2 Experimental

Fabrication of silicon nanowires

Commercially available (100) n-Si wafer was used as a starting material. The Si wafer were cut into 1.5 x 1.5 cm² size. In order to clean the substrate, Si wafer was washed with in an ultrasonic bath for 10 in using an ethanol, acetone, and 2-propanol sequentially. A treatment of UV-O₃ was administered for the duration of 20 mins. Cleaned Si substrate were immersed into the etching solution which contains 5M of HF, and 0.02M of AgNO₃ for 30 mins. After the etching process, Ag dendrite-covered Si substrate were rinsed with de-ionized water and diluted HNO₃ (30wt %) for 30mins. The nanowired-Si substrate were dried with N₂ gas at room temperature.

Deposition of carbon shell onto silicon nanowire

A nanowire-arrayed Si substrate were placed at the center of tubular CVD chamber. Once the temperature reached about 1075°C, a mixture gas of H₂ and CH₄ were introduced into the reactor with

a flow rate of 100 standard cc per minute (sccm).

Characterization of silicon nanowires and carbon coated-silicon nanowires

The silicon nanowires and carbon coated-silicon nanowires were characterized by scanning electron microscopy (SEM, Hitachi S-4300), transmission electron microscopy (TEM, JEOL, JEM-2100F), and Raman spectrometer (LabRam, ARAMIS IR2) with a 532 nm diode laser was used to characterize the quality of carbon shell on silicon nanowires.

DSSC fabrication

To clean a substrate, fluorine doped tin oxide substrate (Nippon Sheet Glass Co., Ltd, Pilkington TEC Glass-TEC) were washed in a detergent solution, DI water, an ethanol-acetone mixture solution (v/v=1/1), and 2-propanol in an ultrasonic bath for 10 min. Finally a treatment of UV-O₃ for 15 min. Nanocrystalline TiO₂ paste (20 nm, ENB-Korea) was coated onto the cleaned FTO glasses using a doctor blading method. The TiO₂-coated FTO glasses were aged at 60 °C for 1 h and annealed at 500 °C for 1 h to create a TiO₂ film. After the heat treatment, TiO₂ coated substrate were immersed in 0.3mM (Bu₄N)₂[Ru(dcbpyH)₂(NCS)₂] (referred to as N719) dye in a mixture of acetonitrile and tert-butanol solvent (v/v = 1/1) with 0.075mM co-adsorption of dineohexyl bis-(3,3-dimethyl-butyl)-phosphinic acid (DINHOP) for overnight at room temperature.

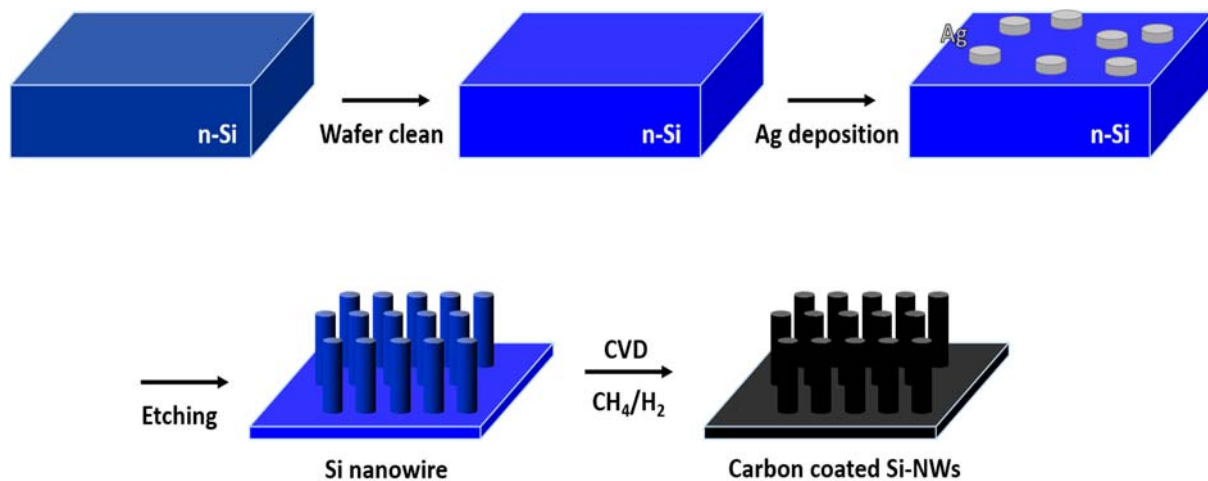
To prepare a Pt counter electrode of DSSC, 10 M H₂PtCl₆ solution in 2-propanol was coated onto a clean FTO glass and this was annealed at 450 °C for 30 min. To prepare a carbon coated-silicon nanowires as counter electrode of DSSC, the as-prepared samples were used as it is. A 50 μm-thick Surlyn film (DuPont) was placed over the prepared dye-coated TiO₂ electrode and the counter electrode was subsequently placed. By pressing the electrodes at 100°C for 3 sec, sealing of the cell was achieved. The electrolyte solution containing a mixture of 0.1 M guanidine thiocyanate, 0.5 M 4-tert-butylpyridine, 0.6 M 1-hexyl-2,3-dimethylimidazolium iodide, and 0.03 M iodine in acetonitrile was introduced into the system, and a final sealing completed the fabrication of the cell.

Characterization of dye-sensitized solar cell

Photocurrent-voltage (J-V) curves of DSSCs were obtained by current-voltage characteristics measurements under AM 1.5G light of 100 mW/cm² (ABET Technology, LS 150 simulator). The intensity of the light was calibrated to 1 sun using a standard single crystalline Si-reference cell (PV Measurements, Inc.). The photovoltaic performance has been characterized by the V_{oc} , J_{sc} , fill factor (FF), and overall efficiency (η) values obtained from the J-V curve. Electrochemical impedance spectroscopy (EIS) and cyclic voltammogram (CV) were measured using a symmetrical structured cell by electrochemical station (Bio-Logic science instruments, VSP, CLB-2000).

6.3 Result and discussion

A schematic representation of silicon nanowire (Si-NW) and carbon coated silicon nanowire (C-Si-NW) fabrication method is presented in figure 6.1. By using simple wet etching process, cleaned Si substrate could get a nanowire structure on the surface. Following the electroless metal deposition (EMD), cleaned Si wafer were dipped into the etching solution of diluted GF and AgNO_3 . After the etching process, excessed Ag dendrite was removed by diluted HNO_3 . In order to coat the carbon at the surface, chemical vapor deposition (CVD) process at 1075°C was performed with desired reaction time.



Scheme 6.1. Schematic diagram of silicon nanowire fabrication and carbon shell deposition.

The surface morphologies of the as prepared Si-NW sample's (without carbon deposition) cross-sectional view (a), upper-view (b), carbon deposited Si-NW sample's cross-sectional view (c), and upper-view (d) were represented in figure 6.1. In the as prepares Si-NW, the length and diameter were ca. $17\ \mu\text{m}$ and in the range of $220 - 500\ \text{nm}$, respectively. (see figure 6.2 (a) and (b)) However, compared to the as prepared Si-NW, the carbon coated Si-NW showed smoothen edges in figure 6.3 (c) and (d) which stand for the carbon shells were successfully deposited on the surfaces of the Si-NWs. At the upper-view, the tips of NWs were congregated in both samples, which is due to the mutual attraction between dangling bonds and electrostatic charges present on the surfaces of the silicon nanowires.

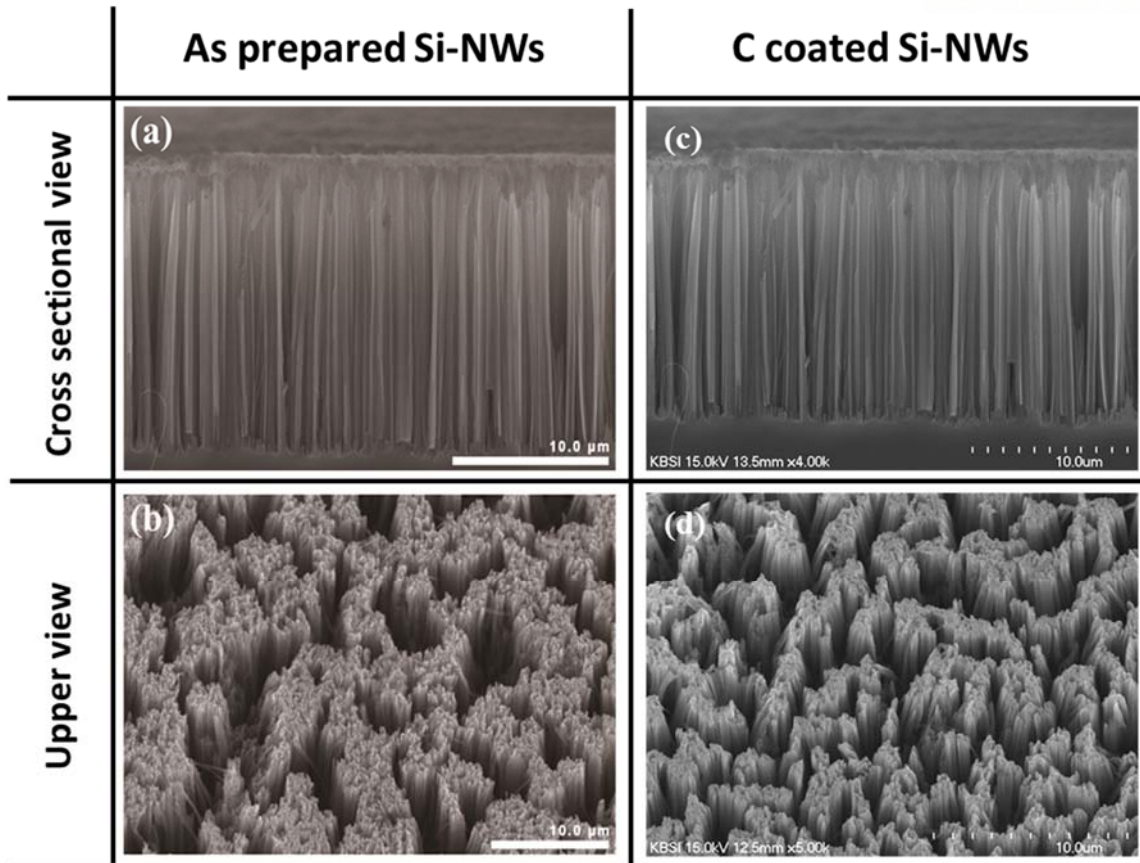


Figure 6.2. SEM images of vertically aligned as-prepared silicon nanowires cross-sectional (a), upper view (b), carbon coated-silicon nanowires cross-sectional view (c) and upper view (d) respectively.

Figure 6.3 shows the TEM images of carbon coated Si-NW with the deposition time of 1min, 3min, 5min, 7min, 11min and as-prepared Si-NW. At the 6.3 (a), as-prepared Si-NW does not show any carbon layer on the Si surface, however, figure 6.3 (b) – (f) represented the samples with deposition time of 1, 3, 5, 7, and 11 min respectively and it shows a gradually increasing tendency of amount of carbon with the deposition time scale.

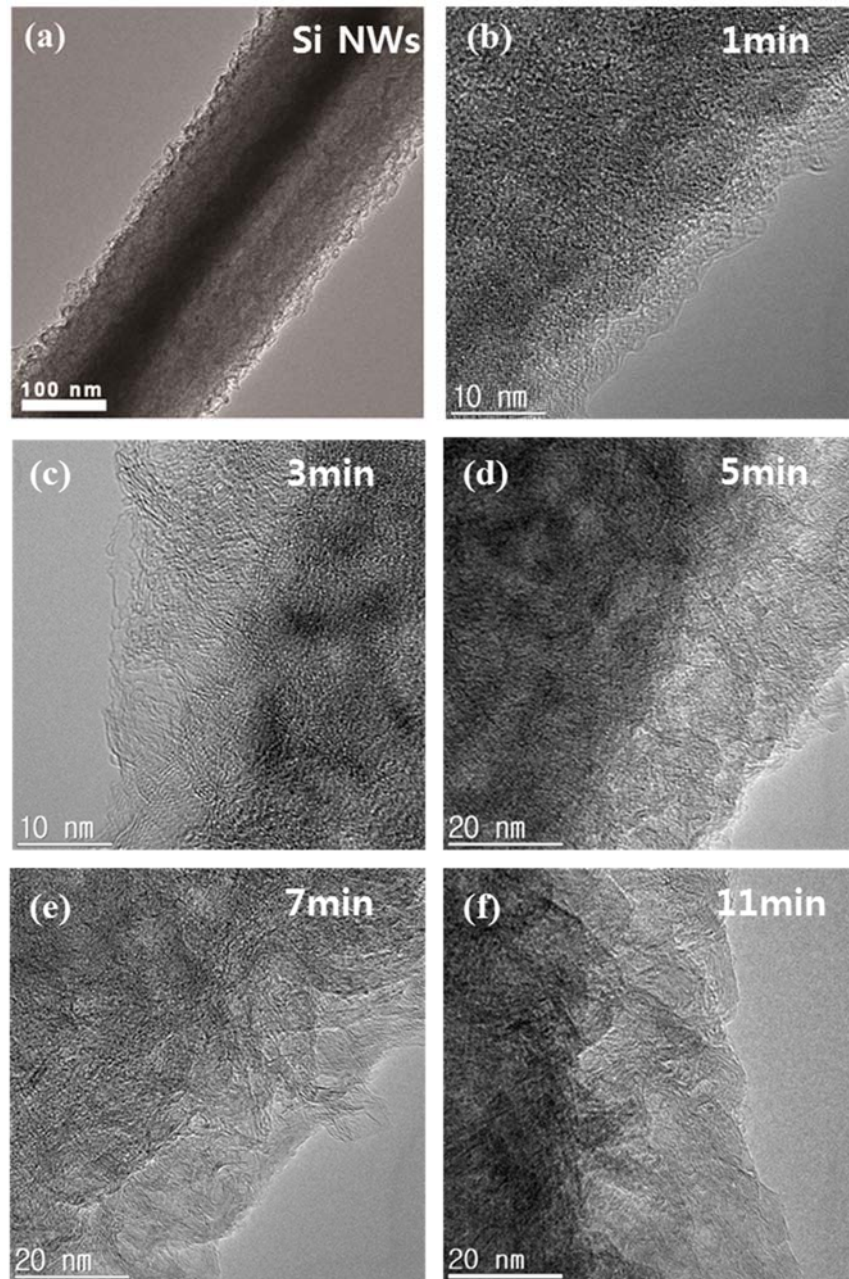


Figure 6.3. Low magnification TEM image of a silicon nanowire (a), HRTEM images of carbon shells deposited on silicon nanowire surface under different reaction times: 1, 3, 5, 7, and 11 min, respectively (b-f). The inter-distance of the carbon shell is about 0.34 nm.

The quality of the carbon shell and the degree of the defects were further investigated by Raman spectroscopy examining the intensities and ratios (I_D/I_G) among the D and G peaks in figure 6.4. The Raman spectra of all the samples were measured in the range of 400 – 2000 cm^{-1} using an excitation of 532 nm diode laser. A peak at around 520 cm^{-1} originates from the Si-Si vibrational mode, and peaks at

around 1350 and 1600 cm^{-1} correspond to the disordered band (D band) and graphitic band (G band) from the carbon shell, respectively. As the reaction time increases, the relative intensity of the D and G peaks increases with respect to the silicon peak. The I_D/I_G ratio obtained from the 1 min reacted sample is lowest (1.2), beyond which it is almost constant ($1.4 \sim 1.5$). The relatively low I_D/I_G ratio of the 1min reacted sample is probably originated from the thinner carbon shell than the others. The peak position and their I_D/I_G ratios are summarized in Table 6.1.

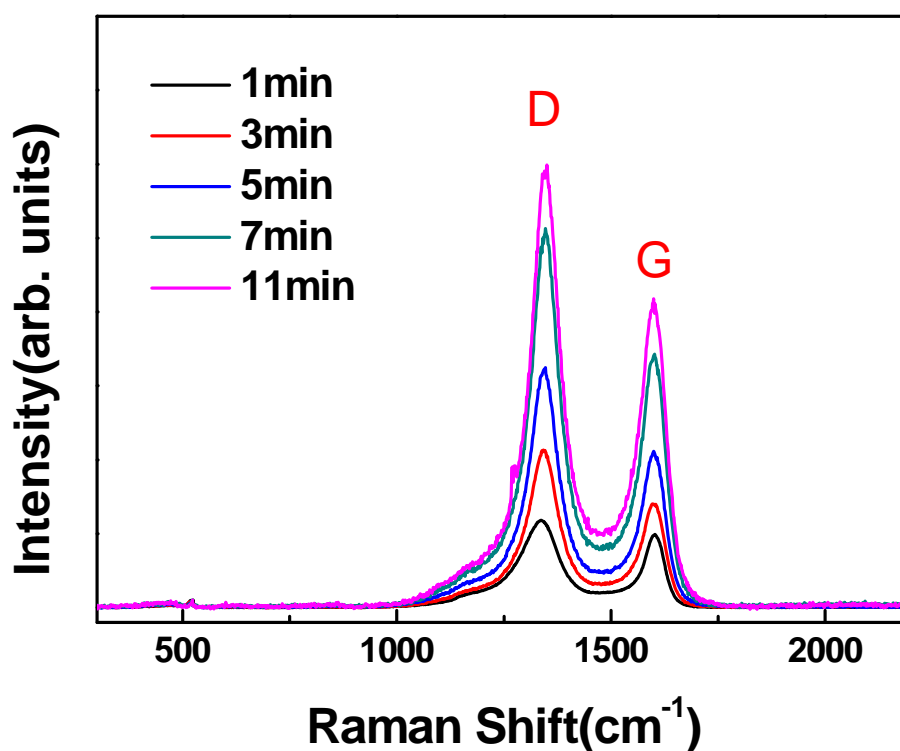


Figure 6.4. (a) Cross sectional compositional line profile of carbon coated-silicon nanowire in STEM and (b) Raman spectra of the carbon coated-silicon nanowires obtained under different reaction times. D and G peaks of the carbon shells were plotted with respect to the silicon peak (inset).

Table 6.1. Peak Position of the G and D bands and their I_D/I_G Ratios

	D band (cm^{-1})	G band (cm^{-1})	I_D/I_G
1min	1344	1600	1.2

3min	1344	1600	1.5
5min	1343	1600	1.5
7min	1346	1600	1.5
11min	1345	1600	1.4

In order to study the electrocatalytic performance for the reduction of I_3^-/Γ at the interface of counter electrode, cyclic voltammetry (CV) and electrochemical impedance spectroscopy (EIS) analysis were checked with the symmetric cell.

To elucidate the electrochemical properties, an EIS were employed which was performed in an open circuit voltage condition. Figure 6.5 shows the Nyquist plot of symmetrical cells with deposition time of 1min, 3min, 5min, 7min, 11min and a conventional Pt coated counter electrode. The first semicircle at the high frequency is ascribed to the charge transfer at the interface between the counter electrodes and electrolyte, and the second semicircle at the low frequency is associated mainly to the Nernst diffusion of I_3^- within the electrolyte. At the counter electrode, the charge transfer resistance (R_{ct}) value is directly related to the number of catalytic site. For this reason, 1 minute carbon deposited sample showed the highest internal resistance due to the small amount of catalytic carbon deposition as can be seen in figure 6.5 (a). In accordance with the deposition time, surface area of carbon coated silicon nanowire was gradually increased. Since the higher carbon contents could provide more catalytic site for the reduction of I_3^- , and we also observed that the R_{ct} value of 5minute deposited sample has the lowest among the other carbon coated silicon nanowire electrodes. The samples of 9 and 11 minute have even longer time of carbon deposition, however, the electro catalytic effect was decreased with over-reaction and could not get smaller R_{ct} values than 5 minute deposition. The low frequency semicircle which was related with electrolyte diffusion has a similar shape for all the cells because the diffusion in the electrolyte is invariant with the catalytic activity of the electrodes. (see figure 6.5 (b)).

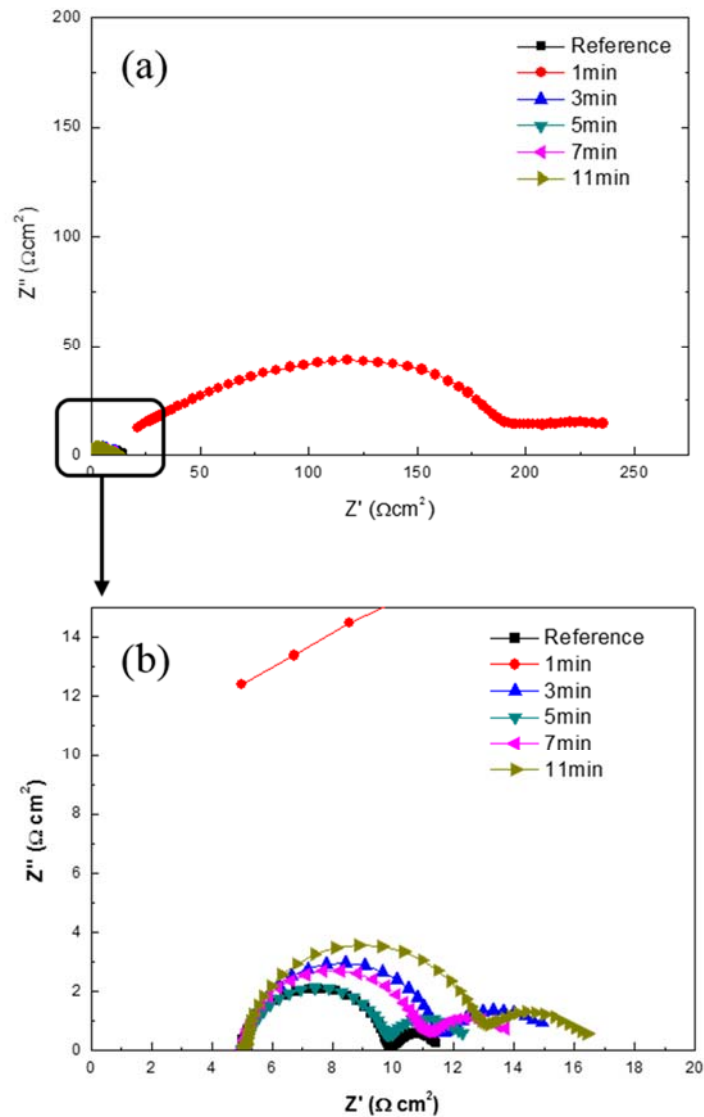


Figure 6.5. Nyquist plot of the electrochemical impedance spectroscopy with symmetrical counter electrodes (a) and zoomed view of Nyquist plot with well performed counter electrodes.

To further interpret the electrochemical properties, a CV analysis were employed. Figure 6.6 represents electrochemical behavior of symmetric cells of Pt and carbon deposited silicon nanowire samples with a scan rate of 100mV/s. All the counter electrodes except of those with 1min carbon deposition sample show proper catalytic effect for I_3^- reduction. Even though the Pt coated symmetrical cell shows the highest current density, 3 to 11 min carbon deposited silicon nanowire samples show comparable current density and catalytic effect. Moreover, the catalytic reaction were occurred faster than Pt and the slope is steeper. Current density saturation of carbon deposited silicon nanowire samples can be seen within

-0.2 to 0.2V while the Pt coated electrode shows at -0.5 to 0.5V. Furthermore, among the carbon deposited silicon nanowire samples, 5 minute carbon deposited sample shows the best current density and this result was well matched with the EIS analysis.

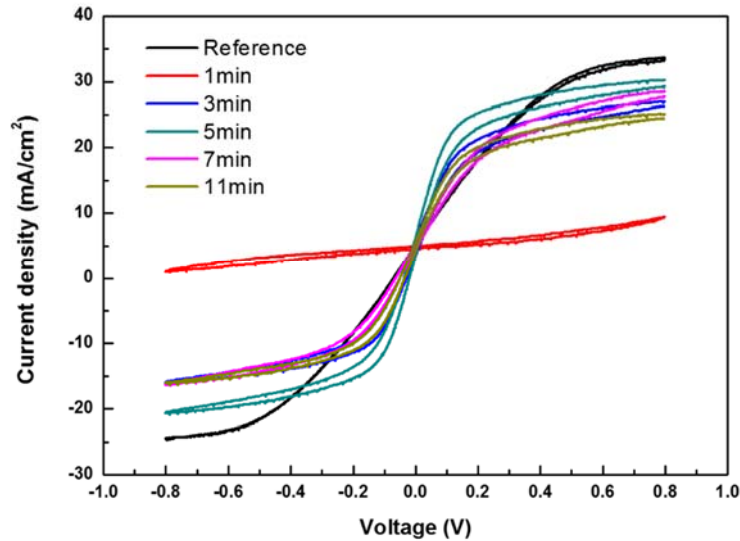


Figure 6.6. Cyclic voltammogram of symmetrical cell with Pt coated and carbon deposited silicon nanowire counter electrodes; scan rate 100mV/s.

The J-V curves of each counter electrode are shown in figure 6.7 and the photovoltaic performance of these cell were listed in table 6.2. The Pt coated reference cell shows J_{sc} of 17.96 mA/cm², V_{oc} of 0.81 V, FF of 67.03 with efficiency of 9.75%. As can be seen from CV analysis, due to the low current density of carbon deposited samples, the J_{sc} value of 5minute carbon deposited silicon nanowire sample shows lower current density than Pt coated cell with 16.91 mA/cm². However, other parameters show V_{oc} of 0.802V and FF of 67.89%. These values were quite comparable with Pt coated sample and finally the conversion efficiency of 5 minute carbon deposited silicon nanowire sample was 9.22%.

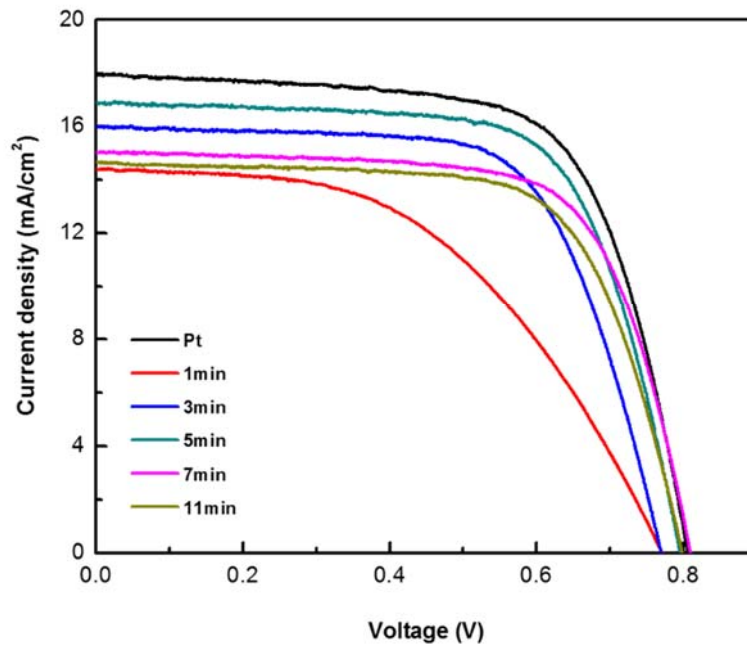


Figure 6.7. Photocurrent-voltage curves of the devices.

Table 6.2. Photovoltaic performance of the Pt and carbon deposited silicon nanowire counter electrodes.

Counter electrodes	J_{sc} (mA/cm ²)	V_{oc} (V)	FF (%)	Eff (%)
Pt (Reference)	17.96	0.810	67.03	9.75
1min	14.60	0.778	50.27	5.71
3min	16.02	0.777	66.12	8.23
5min	16.91	0.802	67.98	9.22
7min	15.54	0.818	68.66	8.73
11min	15.60	0.804	68.01	8.53

6.4 Conclusion

In summary, I have been successfully made a cost effective counter electrode with carbon deposited silicon nanowire. Different deposition time of carbon have been tested as the counter electrode material. In order to analyze the catalytic performance of triiodide reduction reaction, electrochemical and cyclic voltammetry were checked and finally, the best performed condition at a deposition time of 5 minute sample showed the overall efficiency of 9.22% while the well-known Pt counter electrode at the same

condition shows 9.75% efficiency. Overall, the carbon deposited silicon nanowire DSSC showed excellent cell efficiency that rivals cells with a Pt-based CE and exhibited remarkable electrocatalytic activity.

Chapter 7. Quasi-solid state electrolytes with silica nanomaterial for high efficiency dye-sensitized solar cells

This chapter reproduced with permission from J. Lim, et al, Rapid Communication in Photoscience, 2013, 2, 3, 85, Copyright 2014 Korean Society of Photoscience.

7.1 Background and introduction

A silica nanoparticles were synthesized with various silane coupling agents to make specific pathway of electrons and anti-recombination system by solidifying liquid electrolytes. In this study, we used an appropriate method of synthesis for activated silica nanoparticles and silane coupling agents with 3-(triethoxysilyl)propionitrile, Trimethoxy[3-(methylamino)propyl]silane, Triethoxyoctylsilane, and octadecyltrimethoxy silane. Dye-sensitized solar cells using solidified electrolytes with silica nanoparticles exhibit comparatively excellent efficiency, ranging from 2.3 to 7.0% under similar conditions

7.2 Result and discussion

For the past two decades, dye-sensitized solar cells (DSSCs) have been intensively studied because of their advantages such as low production cost, high conversion efficiency, environmental friendliness, and easy fabrication procedure.^{5, 16, 150, 154, 176, 197} A typical DSSC is comprised of TiO₂ working electrode with dye molecules on transparent conductive oxide (TCO) glass, platinum coated counter electrode, and a liquid electrolytes with redox couple (I₃⁻/I⁻) between the electrodes.^{198, 199} However, some of problems caused by these liquid electrolytes such as leakage, volatilization limit, long-term performance and practical use of these DSSCs. To solve these problems, many attempts have been made to replace the liquid electrolytes with gel or quasi-solid type.²⁰⁰⁻²⁰³ At this point of view, we adopted an activated silica nanoparticles with various silane groups to solidifying a liquid electrolytes and to enhance the stability of the solar cells by creating a pathway for ion transportation and prevent electron recombination at the interfaces. Figure 7.1 represents the synthetic route and molecular scheme of silica nanoparticles.

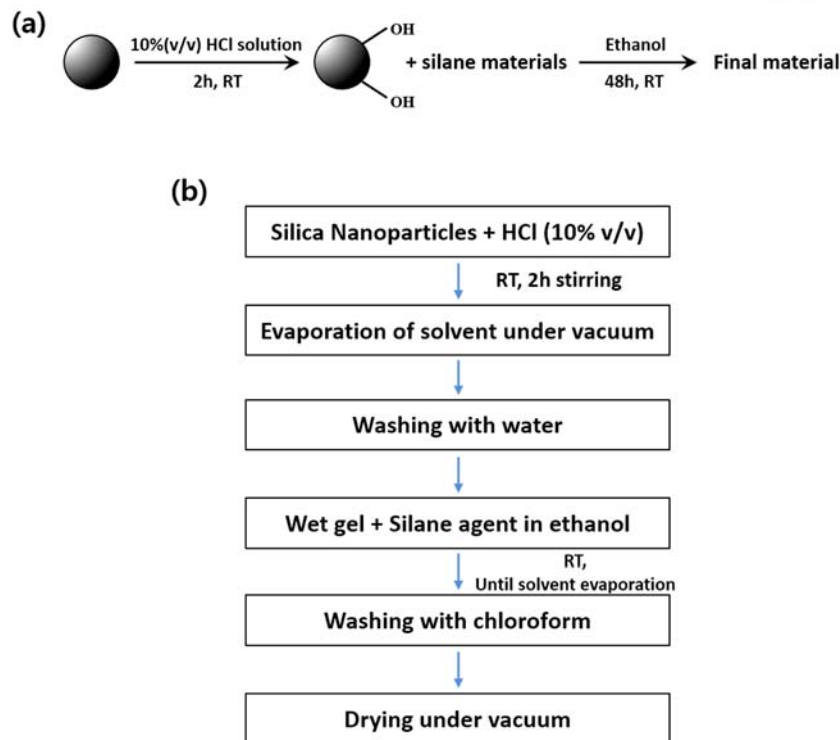
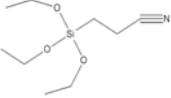
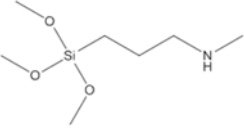
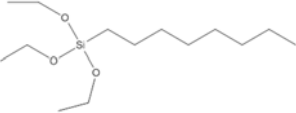
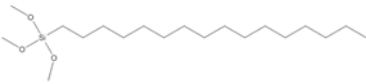


Figure 7.1 Scheme of synthetic route for silica nanomaterials (a) and process table (b).

Using acidic solution (10% v/v HCl), 12nm primary sized silica nanoparticles (Aerosil 200, Evonic) were activated by stirring 2h at room temperature. The activated silica was dried under vacuum and cleaned with DI water until the pH of wet-gel shows 4~5. 40ml of ethanol was used as solvent for wet-gel with 42mmol of silane coupling agents by drop-wise addition. The solution becomes a visible gel after stirring and was dried under vacuum. Unreacted alkoxy silane molecules were removed by chloroform. At the surface of silica which achieved silanol groups (-OH) under vacuum dry, various silane coupling agents were grafted with O-Si-O covalent bond in condition of specific chain which was used as precursor. Before the gelation of electrolyte, an liquid electrolyte solution was prepared containing a mixture of 0.6 M 1-hexyl-2,3-dimethyl-imidazolium iodide, 0.1 M Guanidine thiocyanate, 0.03 M iodine, and 0.5 M 4-tert-butylpyridine in acetonitrile was introduced into the system. By adding synthesized silica nanoparticles into liquid electrolytes, the solution becomes a visible quasi-solid state and can get the solidified electrolyte. Used silane coupling agents with their chemical structures are listed in table 7.1 and the picture of electrolytes is shown in figure 7.2.

Table 7.1 Silane reagent with their chemical structure.

No.	Silane reagent	Chemical structure
1	Reference	Liquid electrolyte
2	None-reagent (Silica only)	Quasi-solid state electrolyte
3	3-(triethoxysilyl)propionitrile (Si_EL 1)	
4	Trimethoxy[3-(methylamino)propyl]silane (Si_EL 2)	
5	Triethoxyoctylsilane (Si_EL 3)	
6	octadecyltrimethoxy silane (Si_EL 4)	

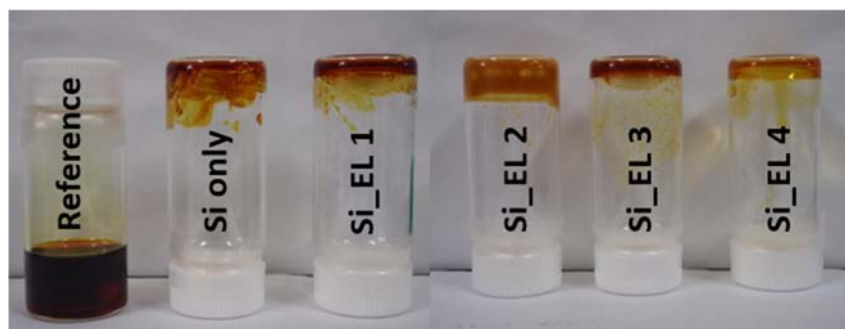


Figure 7.2 Liquid electrolyte and silica-added gel type electrolytes.

In order to prepare electrodes, nanocrystalline TiO_2 was coated onto the cleaned FTO glasses using a doctor blade and annealed at 500°C for 1.5h, then the substrate was immersed in dye solution for 24h. To prepare counter electrodes, H_2PtCl_6 solution in ethanol were coated onto a cleaned FTO glass with

a drop-wise coating and followed by annealing at 450°C. To introduce a liquid electrolytes into the system, a Surllyn film (DuPont) was placed in between the two electrodes to form a sandwich structure and liquid electrolyte were injected through a hole using a vacuum pump. The synthesized quasi-solid state electrolytes (Si_EL) were placed in the middle of the photoanode and both electrodes pressed together with clips. The fabricated DSSCs were kept at room temperature and characterized after 24h. The cells with Si_ELs show an efficiency of 7.7%, 5.3%, 7.0%, 6.7%, 2.3%, and 4.9% respectively as shown in figure 7.3 and their parameters are listed in table 7.2.

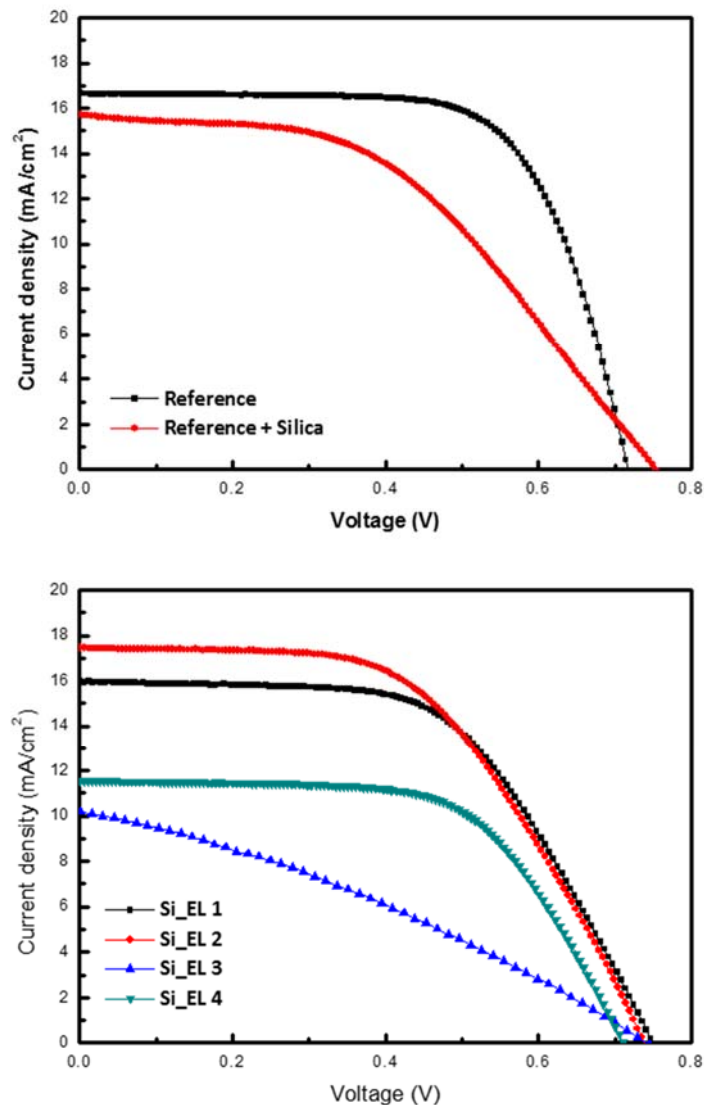


Figure 7.3 Photocurrent-voltage curves of the liquid electrolyte and silica electrolytes.

Table 7.2 Photovoltaic performance of the liquid electrolyte and silica electrolytes.

Electrolytes	V_{oc} (V)	J_{sc} (mA/cm²)	FF (%)	Eff (%)
Reference	0.71	16.7	64.6	7.7
(Silica only)	0.75	15.6	45.7	5.3
Si_EL 1	0.75	15.9	58.7	7.0
Si_EL 2	0.73	17.5	52.8	6.7
Si_EL 3	0.74	10.0	30.7	2.3
Si_EL 4	0.71	11.5	59.6	4.9

Figure 7.3 and table 7.2 show the corresponding current-voltage characteristics for liquid and various Si_EL under AM 1.5 irradiation. At 1 sun illumination, the open circuit voltage (V_{oc}) of 0.71 V and short circuit current (J_{sc}) of 16.7 mA/cm² were measured for the cell which prepared with liquid electrolyte. As reported in table 7.2, the gelled electrolyte by modified silica was surprisingly found that the photovoltaic of V_{oc} properties were improved. Despite a high V_{oc} value, the low J_{sc} and FF is an obstacle to get high efficiency. To overcome these double edges, increasing J_{sc} with similar FF is necessary for the quasi-solid state electrolytes cells. As shown in figure 7.3, even though the gelled electrolytes without a reagent could get higher V_{oc} , internal series resistance was increased by silica nanoparticles and the FF was dramatically decreased with 45.7%. At the modified silica, Si_EL 1 and Si_EL 2 have shown the comparatively high efficiency of 7.0% and 6.7% with the quasi-solid state electrolytes. The functional groups of silane reagents of 3-(triethoxysilyl)propionitrile and Trimethoxy[3-(methylamino)propyl]silane could attached the vacancy of TiO₂ surfaces where is not covered with dye molecules. These functional groups increased the electron density of TiO₂ surface and the electron recombination could be prevented from TiO₂ to electrolyte. In case of the Si_EL 2, by blocking the recombination, quasi-solid state electrolyte can reducing the electron leakage and J_{sc} can be increased with efficiency of 6.7%. However, the performance of DSSCs with the Si_EL4 and Si_EL5 electrolytes shown efficiency of 2.3% and 4.9% caused by long chain length of silane group which does not attached at the vacancy of TiO₂ surfaces and act as obstacle of electron transfer. The viscosity of gel electrolyte could not improve the photovoltaic properties. The solidified electrolytes can increase the stability of the cells by prevent the leakage, however, they could not improve other photovoltaic properties. Be so

much the worse it reduced the speed of electrons diffusion, the gelled electrolyte usually shown the low J_{sc} and FF than that of the liquid electrolyte. At this study, we have successfully synthesized the quasi-solid state electrolytes with various silane agents with proper chain length, which could increase the electron density and prevent the electron recombination by attachment with the TiO_2 surface. The difference of viscosity is almost the same at all the samples, and the only difference among those are the silane reagent.

7.3 Conclusion

In conclusion, we have successfully fabricated dye-sensitized solar cells with various quasi-solid state electrolytes. The simple method of solidifying electrolytes with different silane reagent-assisted silica nanoparticles were tested and well performed cells yield 7.0 and 6.7% efficiency at AM 1.5 condition with increased V_{oc} and J_{sc} . The aspect of FF requires further investigation but these result is very encouraging. Besides, the quasi-solid state electrolyte improved the cell stability with I^-/I_3^- redox couple and they will enable the fabrication of flexible, compact, laminated all solid-state devices free of leakage.

Chapter 8. Polymer hole transport materials for recombination in perovskite-sensitizer solar cell

8.1 Research overview

Inorganic-organic mesoscopic solar cells become a promising alternative to conventional solar cells. we describes a $\text{CH}_3\text{NH}_3\text{PbI}_3$ perovskite sensitized solid state solar cells with the use of different polymer hole transport materials such as 2,2',7,7'-tetrakis-(N,N-di-p-methoxyphenyl-amine)-9,9'-spirobifluorene (spiro-OMeTAD), poly(3-hexylthiophene-2,5-diyl) (P3HT), and Poly[[4,8-bis[(2-ethylhexyl)oxy]benzo[1,2-b:4,5-b']dithiophene-2,6-diyl]][3-fluoro-2-[(2-ethylhexyl)carbonyl]thieno[3,4-b]thiophenediyl]] (PTB7). The device made of spiro-OMeTAD based hole transport layer showed a highest efficiency of 6.9 %. Interestingly, PTB7 polymer which is believed as an electron donor material showed a dominant hole transport behavior in perovskite solar cell. A 200 nm thin layer of PTB7 showed comparatively good efficiency (5.5%) value to the conventional spiro-OMeTAD based device

8.2 Background and introduction

Thin film solar cells or solid state solar cells are a promising technology of energy conversion devices. Although highly efficient solar cells have already been commercialized based on silicon and semiconductor, the cost of materials and fabrication processes are still expensive. The semiconductor materials and fabrication processes of highly efficient solar cells are relies on vacuum deposition or/and thermal treatment, potentially increase the manufacturing cost and decrease the productivity. The third generation solar cells such as dye-sensitized solar cells,^{5, 16, 150, 154, 204} quantum dot solar cells,²⁰⁵⁻²⁰⁸ and organic solar cells²⁰⁹⁻²¹² are encouraged with various structure and material applications. However, the theoretical maximum efficiency performances were far above with those of solar cells due to the energy losses or low dielectric.²¹³ Recently, a new solution processable perovskite materials based on organolead trihalide ($\text{CH}_3\text{NH}_3\text{PbI}_3$) have been developed with very high efficiency in hybrid solid-state solar cells.²¹⁴ Using well-oriented organolead trihalide perovskite as the light absorber, scaffold layer of nanoporous titanium dioxide (TiO_2) or aluminum oxide (Al_2O_3) can be coated through a simple solution process.²¹⁴⁻²¹⁶ Some work focusing on a mixed halide ($\text{CH}_3\text{NH}_3\text{PbI}_{3-x}\text{Cl}_x$) perovskite with alumina scaffold layer, they found the fast electron transport.²¹⁶ Eperon et al. has reported on PCE of 11.4 % using the morphology controlled perovskite photoactive layer.²¹⁷ Carnie et al. simplifying a fabrication process of photoactive layer and achieving power conversion efficiency (PCE) of 7.16 %.²¹⁸ Heo et al. reported PCE of 12 % by replacing the hole transport materials from spiro-

OMeTAD to polytriarylamine (PTAA) polymer²¹⁹ and other researchers are represent two step deposition of perovskite materials for uniformly coated layer.^{220, 221} The one of essential qualification for high efficiency of solar cells is a balance of series and shunt resistance. However, because of the high conductivity of perovskite materials, demanding a thick layer of HTM to evade the imbalance or pinhole effect.^{222, 223} Due to these drawback, even though a most HTMs are less conductivity, thick layer of HTM was necessary with high series resistance. Herein, I present a combined organic hybrid solar cells using different HTMs with a fluorine doped tin oxide glass as the substrate, a synthesized $\text{CH}_3\text{NH}_3\text{PbI}_3$ perovskite as an electron donor, tested polymers with 2,2',7,7'-tetrakis-(N,N-di-p-methoxyphenyl-amine)-9,9'-spirobifluorene (spiro-OMeTAD), poly(3-hexylthiophene-2,5-diyl) (P3HT), and Poly[[4,8-bis[(2-ethylhexyl)oxy]benzo[1,2-b:4,5-b']dithiophene-2,6-diyl][3-fluoro-2-[(2-ethylhexyl)carbonyl]thieno[3,4-b]thiophenediyl]] (PTB7) as hole transport materials, and a sputtered gold grid as the electrode. A complete cell with spiro-OMeTAD shows J_{sc} of 13.9 mA/cm², V_{oc} of 0.82 V, FF of 60.2 with efficiency (η) of 6.9%. Another best performed PTB7 cells shows J_{sc} , V_{oc} , FF, and η values of 12.6mA/cm², 0.72V, 60.4 and 5.5% respectively.

8.3 Experimental

Perovskite materials

The methylammonium perovskite material ($\text{CH}_3\text{NH}_3\text{PbI}_3$) was synthesized as follow: A hydroiodic acid (30ml, 57wt. % in water, Aldrich) was mixed with methylamine (27.8ml, 0.273mol, 40% in methanol, TCI) at 0°C ice bath by stirring for 2 h. After stirr, the resulting solution was evaporated in vacuum oven and synthesized materials ($\text{CH}_3\text{NH}_3\text{I}$) were produced. The synthesized chemical was washed with diethyl ether three times and dried under vacuum for using without further purification; a white color powder was formed indicating successful synthesized. To prepare (CH_3NH_3) PbI_3 , the 1:1 molar ratio of Methylammonium iodide and lead(II) iodide was dissolved in anhydrous γ -butyrolactone at 60°C for overnight with stirring.

Solar cell fabrication

Fluorine doped tin oxide glasses (Pilkington, TEC-8, 8 Ω /sq) were washed with a detergent solution and then cleaned in an ultrasonic bath for 5 min using an ethanol–acetone solution (v/v = 1/1) and 2-propanol, in turn, and then underwent an oxygen plasma treatment was administered for the duration of 15min. A thin layer of dense TiO_2 blocking layer was formed through the RF sputter with 600Å of thickness. The mesoporous TiO_2 layer was introduced by spin coating (4500rpm, 40sec) by diluted TiO_2 paste (CCIC 18NT) terpeneol and the layer was annealed in air at 500°C for 1 h. The cooled TiO_2 films

were coated with perovskite by spin coater at 2500rpm for 40 seconds and annealed at 100°C for 20min.

For the hole transport, different hole transport materials (HTM) coated onto TiO₂ films using spin coater at 2500 rpm for 40 sec. To fabricate the counter electrode, 70nm Au electrode was deposited onto the cell by thermal evaporation.

Composition of HTM

The composition of HTM was 170mM 2,2',7,7'-tetrakis-(N,N-di-p-methoxyphenyl-amine)-9,9'-spirobifluorene (spiro-OMeTAD, Merk), 198mM 4-tert-butylpyridine (TBP, 96%, Aldrich) and 64mM bis(trifluoromethane) sulfonimide lithium salt (LiTFSI, 99.95%, Aldrich) in a mixture solvent of chlorobenzene and acetonitrile (1/0.1=v/v). 13 mg/ml solution of P3HT (Aldrich) were prepared in chlorobenzene. PTB7 (1-materials) solution was 12 mg/ml in chlorobenzene.

Characterization

The active area of the cell was measured by optical microscope (Olympus) and the thickness of mesoporous TiO₂ layer was checked by surface profilermeter (P-6, KLA-Tencor). The photovoltaic properties of the cells were measured using a Keithley 2400 digital source meter under the irradiation of a solar simulator (AM 1.5G, 100mW/cm², Sol3A, class AAA, Oriel) as a light source, which was calibrated by a certified standard reference cell (PV Measurement, Inc.). The performance has been characterized by the V_{oc} , J_{sc} , fill factor and overall efficiency obtained from J-V curve. The incident photon to current conversion efficiency spectra were measured using a PV measurement (PV measurement, Inc, QEX7 series) and cross-sectional morphology of the solid state solar cell were checked by a field-emission scanning electron microscopy (FE-SEM, Nano230, FEI co.).

8.4 Result and Discussion

Here, I report a new bilayer heterojunction with organic-inorganic materials onto the nanoporous TiO₂ architecture. The surface-decorated metal halide perovskite materials with the formula of (C_nH_{2n}+1NH₃)MX (M=Pb ;X=I, Br, Cl) were infiltrated within a TiO₂, act as function of the light absorber, and various organic materials of which function as the p-type hole transport materials (HTM).

Figure 8.1a shows the X-ray diffraction (XRD) peak of the crystalline structure of synthesized perovskite materials, taken from the powder, shows 6 sharp reflections peaks and the peaks were well matched with the previously published result with (110), (112), (230), (310), (224), and (314) crystal planes of the tetragonal perovskite structure. The inset of figure 8.1a shows a (C_nH_{2n}+1NH₃)MX structure of tetragonal perovskite material. I also prepared the perovskite film for the UV-vis spectroscopy. At the UV-vis spectra, the film was absorbs widely from visible until near infrared in figure 8.1b. For the maximum energy harvesting of solar cells, expand spectral response of the light

absorber could be the proper way and the expanded absorbance over the entire range of visible spectrum indicated the formation of $\text{CH}_3\text{NH}_3\text{PbI}_3$.

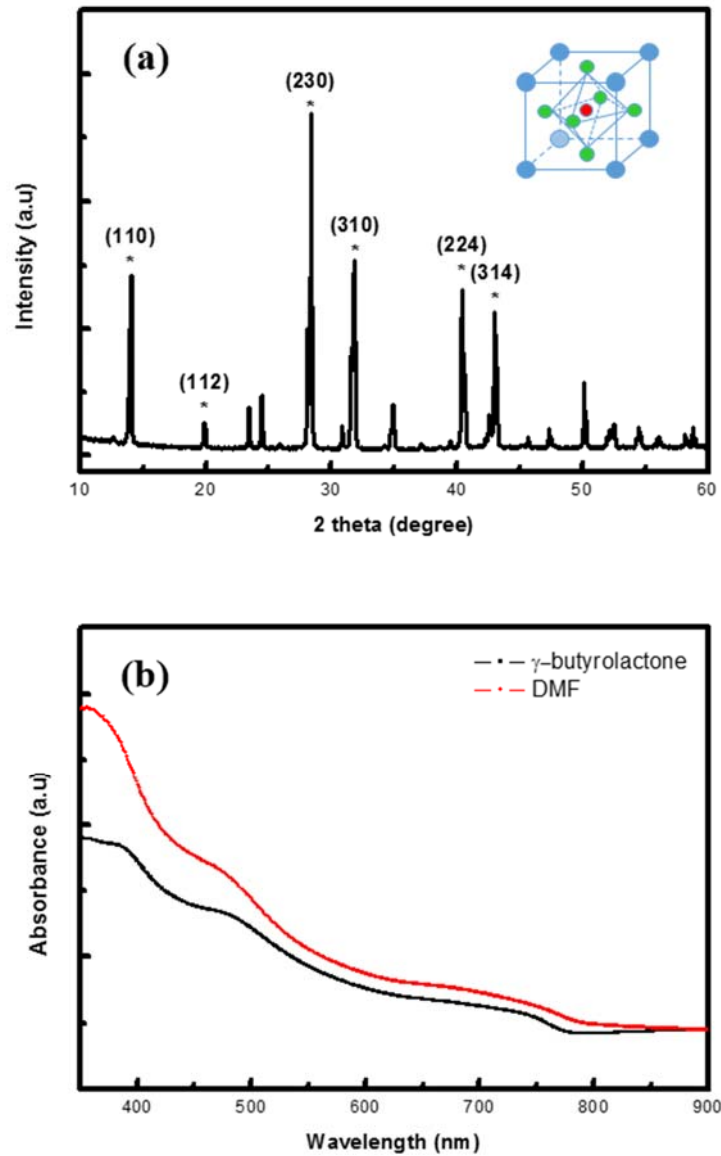


Figure 8.1 (a) X-ray diffraction of $\text{CH}_3\text{NH}_3\text{PbI}_3$ perovskite materials prepared as powder form and inset shows tetragonal structure of materials. (b) UV-visible spectrum prepared from γ -butyrolactone (GBL) and dimethylformamide (DMF).

Because of the high conductivity of perovskite materials, thick layer of HTM should be required to prevent pinhole effect. However, thick layer of HTM could cause high series resistance and interfere high efficiencies of full cell. Figure 8.2a shows schematic structure of tested organic materials as hole transport layer : 2,2',7,7'-tetrakis-(N,N-di-p-methoxyphenyl-amine)-9,9'-spirobifluorene (spiro-OMeTAD), poly(3-hexylthiophene-2,5-diyl) (P3HT), and Poly[[4,8-bis[(2-ethylhexyl)oxy]benzo[1,2-b:4,5-b']dithiophene-2,6-diyl][3-fluoro-2-[(2-ethylhexyl)carbonyl]thieno[3,4-b]thiophenediyl]] (PTB7) and as previously reported electronic properties are summarized in table 8.1. The energy diagrams of each components are shown in figure 8.2b with the HTM materials. As previously reported, spiro-OMeTAD was widely used as hole conductor in $\text{CH}_3\text{NH}_3\text{PbI}_3$ sensitizer solar cells while P3HT and PTB7 were used as electron donor and/or hole conductor in organic solar cells. Notably, even though the P3HT and PTB are usually used as electron donor in organic electronic devices, here I used it as hole transport materials.

Table 8.1 The levels of HOMO, LUMO, and hole mobility of HTM materials

	HOMO	LUMO	Hole mobility
Spiro-OMeTAD			$\sim 10^{-5} \text{ cm}^2/\text{V}\cdot\text{sec}$
P3HT	-5.1	-3.2	$\sim 10^{-1} \text{ cm}^2/\text{V}\cdot\text{sec}$
PTB7	-5.15	-3.31	$\sim 10^{-3} \text{ cm}^2/\text{V}\cdot\text{sec}$

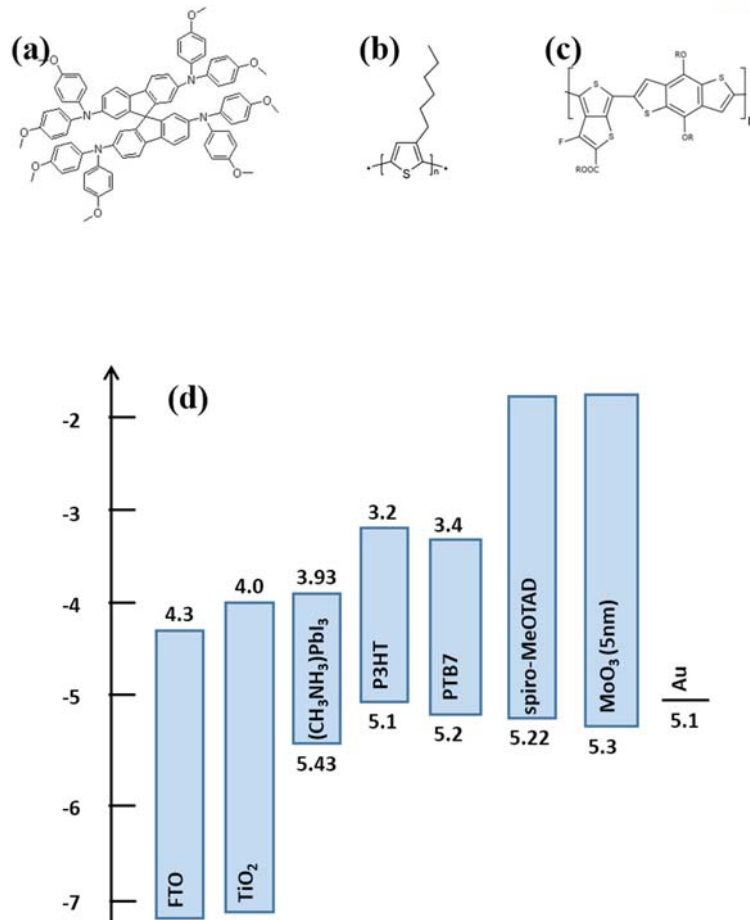


Figure 8.2 Molecular structure of hole conductor materials of (a) spiro-OMeTAD, (b) P3HT, and (c) PTB7. (d) Energy diagram of materials which was used in this study.

Figure 8.3a illustrate the energy levels of the system components and model of the charge separation processes and figure 8.3b shows the schematic device configuration in this study. In figure 8.2a, the tested HTM materials are energetically matched with perovskite sensitizer and energy level of the TiO₂/sensitizer/HTM are well positioned for electron injection to TiO₂ and hole conductor to tested HTMs. Schematic device along with the cross sectional layer was shown in figure 8.3b. In order to protect the electron recombination, thin TiO₂ layer, called the “compact layer” was deposited onto transparent conducting oxide (TCO). Mesoporous TiO₂ with metal-halide-based perovskite sensitizer as an active layer, HTM, and Au electrode was deposited in sequence. I took scanning electron microscope (SEM) images of the cross-sectional surface morphology of representative full cell in figure 8.3c. The thickness of spiro-OMeTAD, P3HT, and PTB7 was 420, xxx, and xxx nm respectively. Each of these materials was used as the hole conductor in solar cells with CH₃NH₃PbI₃-coated TiO₂ layer,

and characterized under 1-sun illumination.

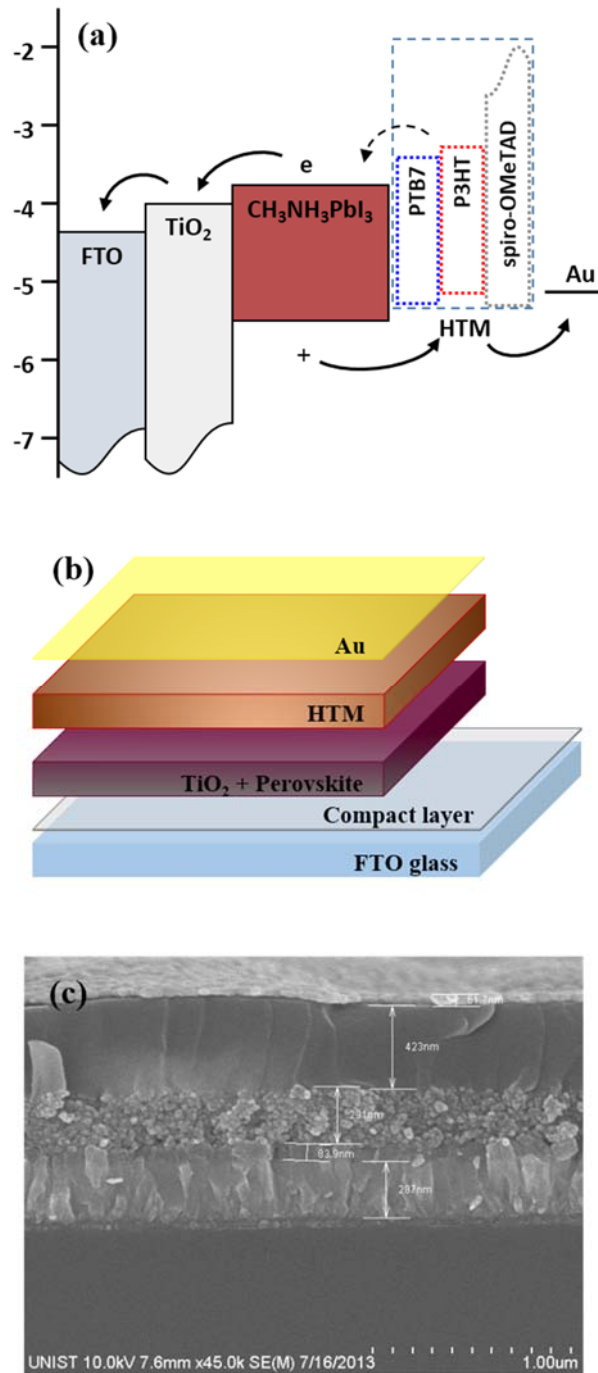


Figure 8.3 (a) Schematic of energy alignment of the different components. (b) Structure of the device architecture and (c) SEM image of the architecture.

The photovoltaic parameters for all three devices were extracted from the J-V curves in figure 8.4 and the cell performance parameters are summarized in table 8.2. For comparison, without HTM (black, circle) sample was prepared. A metal-halide perovskite sensitized cell without HTM shows J_{sc} of 4.5 mA/cm², V_{oc} of 0.38V, FF of 44.7 with efficient (η) of 0.8%. spiro-OMeTAD (red, circle) shows the hole conductor properties with J_{sc} of 13.9 mA/cm², V_{oc} of 0.82V, FF of 60.2 with efficient (η) of 6.9%. Notably, even though P3HT are usually used as hole conductor in organic solar cells, it does not show a high efficiency with other parameters (see the parameters in Table 8.2). Although the organic solar cells used PTB7 as electron donor, PTB7 are used as hole conductor at this study. The best device of PTB7 cell exhibits J_{sc} of 12.6 mA/cm², V_{oc} of 0.72V, FF of 60.4, and η of 5.5% by demonstrating a good charge separation kinetics. Even though the spiro-OMeTAD shows the highest efficiency among these, P3HT and PTB7 can be used as hole transport materials with thin layer. Since these materials shows light absorption in UV range and electron donor properties, it can be supposed to function as current generation with role of hole transporter. To confirm the electron contribution of polymers, the quantum efficiency of the cells were given in figure 8.5.

Table 8.2 Photovoltaic performance of the cells with various HTM.

	Jsc (mA/cm²)	Voc (V)	FF (%)	Eff (%)
-	4.5	0.38	44.7	0.8
OMeTAD	13.9	0.82	60.2	6.9
P3HT	12.5	0.51	50.6	3.2
PTB7	12.6	0.72	60.4	5.5

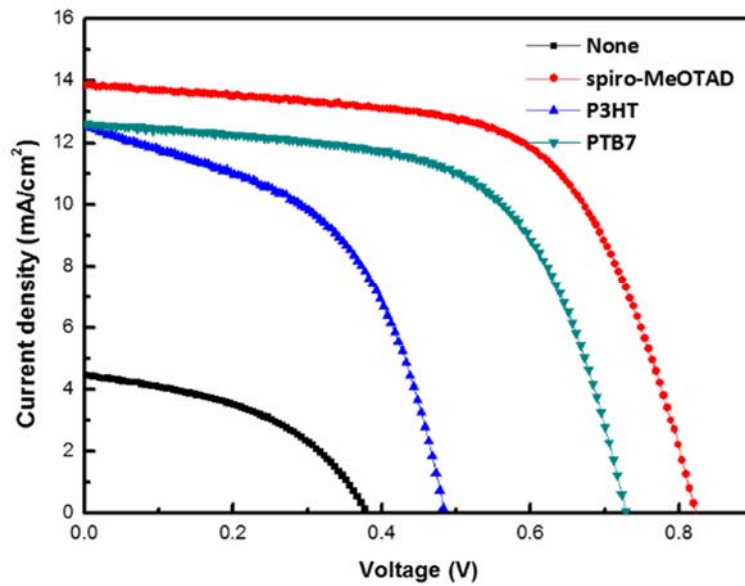


Figure 8.4 Photocurrent-voltage curves of the without HTM sample (black, circle), spiro-OMeTAD sample (red, circle), P3HT sample (blue, triangle), and PTB7 sample (cyan, triangle).

The incident photon to current conversion efficiency (IPCE) spectrum of the cells indicates that the devices show a spectral response from the near infrared to visible region with the maximum photoresponse in 450 nm and the broad peak extended. This IPCE spectra was well matched with UV-vis absorbance of synthesized perovskite film at figure 8.1b. However, polymer based HTM cells does not show any other photoresponse by polymer as electron donor at this IPCE and this observation demonstrate that only synthesized $\text{CH}_3\text{NH}_3\text{PbI}_3$ perovskite can be act as the light absorber. At this aspect, all the materials which were used as hole transport materials just act as the hole transport for recombination in perovskite solar cells.

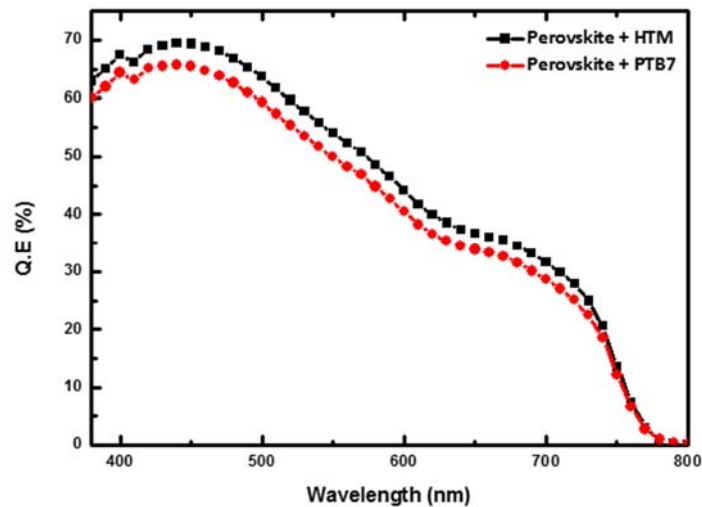


Figure 8.5 Incident photon to current conversion efficiency (IPCE) of the perovskite solar cells. Perovskite with spiro-OMeTAD (black, square), and perovskite with PTB7 (red, circle).

8.5 Conclusion

To conclude, I demonstrated the solar cells with synthesized $\text{CH}_3\text{NH}_3\text{PbI}_3$ perovskite solid-state solar cells using organic hole transport materials. Among the HTMs (spiro-OMeTAD, P3HT, and PTB7), spiro-OMeTAD cells show the best efficiency with 6.9 % under AM 1.5G. PTB7 which was used as electron donor at organic solar cells shows the hole transfer properties with the relatively good efficiency of 5.5%. The role of hole transport materials is accept holes and transport them to electrode. In this study, energetically well matched organic material candidates can be used for the same purpose and shown an efficiency alike. These result will lead to more cost-efficient organic-inorganic hybrid solar cells in the future.

Chapter 9. Summary

I have reported several panchromatic strategies with novel fabrication methods. By using newly suggested techniques, the parallel connected panchromatic dye sensitized solar cell (DSSC) have been successfully fabricated. The higher value of J_{sc} of the panchromatic cell confirms the parallel tandem effect and quantum efficiency of panchromatic cells is higher than those of single cells. Furthermore, the IPCE spectra revealed the panchromatic properties. Even though the values of V_{oc} were modified by the different back reaction of electrons, the properties of parallel tandem cell was clearly shown. Not only for the parallel tandem, I also reported series connected tandem cell by using reversely fabricated DSSC. By controlling each layer, I have successfully fabricated reverse structured DSSC. With this reverse structured DSSC, I introduce an inverted organic solar cells as an upper cell. According to the series tandem properties, the cell showed increased V_{oc} value than those of single cells. Furthermore, this suggested technique could be extended to produce devices in research with other thin film solar cells.

I also demonstrated the cost effective counter electrodes with carbon black / TiO_2 slurry and carbon deposited silicon nanowire counter electrodes. Both of the counter electrode were characterized by cyclic voltammetry and electrochemical impedance spectroscopy. Interface charge transfer and mass transport were analyzed at the chapter, and fabricated DSSC showed excellent cell efficiency that rivals cells with a Pt-based counter electrode and exhibited remarkable electro catalytic activity. Moreover, in order to increase a stability of DSSC, I have successfully solidified liquid electrolyte using silane reagent-assisted silica nanoparticle. Besides, the quasi-solid state electrolyte improved the cell stability with I^-/I_3^- redox couple and they could be lead the fabrication of flexible, compact, laminated all solid-state devices with free of leakage. Finally, I demonstrated the solar cells with synthesized $\text{CH}_3\text{NH}_3\text{PbI}_3$ perovskite solid-state solar cells using organic hole transport materials. By using various hole conductor such as spiro-OMeTAD, P3HT, and PTB7, energy band of hole conductor were matched for the cost efficient organic-inorganic perovskite solar cell.

Chapter 10. References

1. Becquerel, A. E. Recherches sur les effets de la radiation chimique de la lumiere solaire au moyen des courants electriques. *C. R. Acad. Sci.* 1839, 9.
2. Park, N. G.; Van De Lagemaat, J.; Frank, A. J. Comparison of dye-sensitized rutile- and anatase-based TiO₂ solar cells. *J. Phys. Chem. B* 2000, 104, 8989-8994.
3. Memming, R. PHOTOCHEMICAL AND ELECTROCHEMICAL PROCESSES OF EXCITED DYES AT SEMICONDUCTOR AND METAL ELECTRODES*. *Photochem. Photobiol.* 1972, 16, 325-333.
4. Matsumura, M.; Nomura, Y.; Tsubomura, H. Dye-sensitization on the photocurrent at zinc oxide electrode in aqueous electrolyte solution. *Bull. Chem. Soc. Jpn.* 1977, 50, 2533-2537.
5. O'Regan, B.; Grätzel, M. A low-cost, high-efficiency solar cell based on dye-sensitized colloidal TiO₂ films. *Nature* 1991, 353, 737-740.
6. Sun, P.; Zhang, X.; Wang, C.; Wei, Y.; Wang, L.; Liu, Y. Rutile TiO₂ nanowire array infiltrated with anatase nanoparticles as photoanode for dye-sensitized solar cells: Enhanced cell performance via the rutile-anatase heterojunction. *J. Mater. Chem. A* 2013, 1, 3309-3314.
7. Jyoti, D.; Mohan, D.; Dhar, R. Investigation of transport and optical properties of mesoporous anatase and rutile TiO₂ films for application in dye-sensitized solar cells. *Mod. Phys. Lett. B* 2012, 26.
8. Park, J. T.; Patel, R.; Jeon, H.; Kim, D. J.; Shin, J. S.; Hak Kim, J. Facile fabrication of vertically aligned TiO₂ nanorods with high density and rutile/anatase phases on transparent conducting glasses: High efficiency dye-sensitized solar cells. *J. Mater. Chem.* 2012, 22, 6131-6138.
9. Li, G.; Richter, C. P.; Milot, R. L.; Cai, L.; Schmuttenmaer, C. A.; Crabtree, R. H.; Brudvig, G. W.; Batista, V. S. Synergistic effect between anatase and rutile TiO₂ nanoparticles in dye-sensitized solar cells. *Dalton Trans.* 2009, 10078-10085.
10. Landmann, M.; Rauls, E.; Schmidt, W. G. The electronic structure and optical response of rutile, anatase and brookite TiO₂. *J. Phys.: Condens. Matter* 2012, 24.
11. Martinson, A. B. F.; Elam, J. W.; Hupp, J. T.; Pellin, M. J. ZnO nanotube based dye-sensitized solar cells. *Nano Lett.* 2007, 7, 2183-2187.
12. Mor, G. K.; Shankar, K.; Paulose, M.; Varghese, O. K.; Grimes, C. A. Use of highly-ordered TiO₂ nanotube arrays in dye-sensitized solar cells. *Nano Lett.* 2006, 6, 215-218.
13. Jennings, J. R.; Ghicov, A.; Peter, L. M.; Schmuki, P.; Walker, A. B. Dye-sensitized solar cells based on oriented TiO₂ nanotube arrays: Transport, trapping, and transfer of electrons. *J. Am. Chem. Soc.* 2008, 130, 13364-13372.
14. Roy, P.; Berger, S.; Schmuki, P. TiO₂ nanotubes: Synthesis and applications. *Angew. Chem. Int. Ed.* 2011, 50, 2904-2939.
15. So, S.; Lee, K.; Schmuki, P. High-Aspect-Ratio Dye-Sensitized Solar Cells Based on Robust,

Fast-Growing TiO₂ Nanotubes. *Chem. Eur. J.* 2013, 19, 2966-2970.

16. Law, M.; Greene, L. E.; Johnson, J. C.; Saykally, R.; Yang, P. Nanowire dye-sensitized solar cells. *Nat. Mater.* 2005, 4, 455-459.
17. Liu, B.; Aydil, E. S. Growth of oriented single-crystalline rutile TiO₂ nanorods on transparent conducting substrates for dye-sensitized solar cells. *J. Am. Chem. Soc.* 2009, 131, 3985-3990.
18. Feng, X.; Shankar, K.; Varghese, O. K.; Paulose, M.; Latempa, T. J.; Grimes, C. A. Vertically aligned single crystal TiO₂ nanowire arrays grown directly on transparent conducting oxide coated glass: Synthesis details and applications. *Nano Lett.* 2008, 8, 3781-3786.
19. Zhang, Q.; Dandeneau, C. S.; Zhou, X.; Cao, C. ZnO nanostructures for dye-sensitized solar cells. *Adv. Mater.* 2009, 21, 4087-4108.
20. Shankar, K.; Basham, J. I.; Allam, N. K.; Varghese, O. K.; Mor, G. K.; Feng, X.; Paulose, M.; Seabold, J. A.; Choi, K. S.; Grimes, C. A. Recent advances in the use of TiO₂ nanotube and nanowire arrays for oxidative photoelectrochemistry. *J. Phys. Chem. C* 2009, 113, 6327-6359.
21. Oh, J. K.; Lee, J. K.; Kim, H. S.; Han, S. B.; Park, K. W. TiO₂ branched nanostructure electrodes synthesized by seeding method for dye-sensitized solar cells. *Chem. Mater.* 2010, 22, 1114-1118.
22. Wu, W. Q.; Lei, B. X.; Rao, H. S.; Xu, Y. F.; Wang, Y. F.; Su, C. Y.; Kuang, D. B. Hydrothermal fabrication of hierarchically anatase TiO₂ nanowire arrays on FTO glass for dye-sensitized solar cells. *Sci. Rep.* 2013, 3.
23. Baxter, J. B.; Aydil, E. S. Nanowire-based dye-sensitized solar cells. *Appl. Phys. Lett.* 2005, 86, 1-3.
24. Nazeeruddin, M. K.; Kay, A.; Rodicio, I.; Humphry-Baker, R.; Müller, E.; Liska, P.; Vlachopoulos, N.; Grätzel, M. Conversion of light to electricity by cis-X₂bis(2,2'-bipyridyl-4,4'-dicarboxylate)ruthenium(II) charge-transfer sensitizers (X = Cl⁻, Br⁻, I⁻, CN⁻, and SCN⁻) on nanocrystalline TiO₂ electrodes. *J. Am. Chem. Soc.* 1993, 115, 6382-6390.
25. Scholl, M.; Ding, S.; Lee, C. W.; Grubbs, R. H. Synthesis and activity of a new generation of ruthenium-based olefin metathesis catalysts coordinated with 1,3-dimesityl-4,5-dihydroimidazol-2-ylidene ligands. *Org. Lett.* 1999, 1, 953-956.
26. Yella, A.; Lee, H. W.; Tsao, H. N.; Yi, C.; Chandiran, A. K.; Nazeeruddin, M. K.; Diau, E. W. G.; Yeh, C. Y.; Zakeeruddin, S. M.; Grätzel, M. Porphyrin-sensitized solar cells with cobalt (II/III)-based redox electrolyte exceed 12 percent efficiency. *Science* 2011, 334, 629-634.
27. Mishra, A.; Fischer, M. K. R.; Buerle, P. Metal-Free organic dyes for dye-sensitized solar cells: From structure: Property relationships to design rules. *Angew. Chem. Int. Ed.* 2009, 48, 2474-2499.
28. Horiuchi, T.; Miura, H.; Sumioka, K.; Uchida, S. High efficiency of dye-sensitized solar cells based on metal-free indoline dyes. *J. Am. Chem. Soc.* 2004, 126, 12218-12219.
29. Ito, S.; Zakeeruddin, S. M.; Humphry-Baker, R.; Liska, P.; Charvet, R.; Comte, P.; Nazeeruddin, M. K.; Péchy, P.; Takata, M.; Miura, H.; Uchida, S.; Grätzel, M. High-efficiency organic-dye-sensitized

- solar cells controlled by nanocrystalline-TiO₂ electrode thickness. *Adv. Mater.* 2006, 18, 1202-1205.
30. Koumura, N.; Wang, Z. S.; Mori, S.; Miyashita, M.; Suzuki, E.; Hara, K. Alkyl-functionalized organic dyes for efficient molecular photovoltaics. *J. Am. Chem. Soc.* 2006, 128, 14256-14257.
 31. Hao, S.; Wu, J.; Huang, Y.; Lin, J. Natural dyes as photosensitizers for dye-sensitized solar cell. *Sol. Energy* 2006, 80, 209-216.
 32. Polo, A. S.; Itokazu, M. K.; Murakami Iha, N. Y. Metal complex sensitizers in dye-sensitized solar cells. *Coord. Chem. Rev.* 2004, 248, 1343-1361.
 33. Olsen, E.; Hagen, G.; Eric Lindquist, S. Dissolution of platinum in methoxy propionitrile containing LiI/I₂. *Sol. Energ. Mat. Sol. C.* 2000, 63, 267-273.
 34. Murakami, T. N.; Ito, S.; Wang, Q.; Nazeeruddin, M. K.; Bessho, T.; Cesar, I.; Liska, P.; Humphry-Baker, R.; Comte, P.; Péchy, P.; Grätzel, M. Highly efficient dye-sensitized solar cells based on carbon black counter electrodes. *J. Electrochem. Soc.* 2006, 153, A2255-A2261.
 35. Hagfeldt, A.; Grätzel, M. Molecular photovoltaics. *Acc. Chem. Res.* 2000, 33, 269-277.
 36. Baxter, J. B.; Walker, A. M.; Van Ommering, K.; Aydil, E. S. Synthesis and characterization of ZnO nanowires and their integration into dye-sensitized solar cells. *Nanotechnology* 2006, 17, S304-S312.
 37. De Angelis, F.; Fantacci, S.; Mosconi, E.; Nazeeruddin, M. K.; Grätzel, M. Absorption spectra and excited state energy levels of the N719 dye on TiO₂ in dye-sensitized solar cell models. *J. Phys. Chem. C* 2011, 115, 8825-8831.
 38. K. Nazeeruddin, M.; Pechy, P.; Gratzel, M. Efficient panchromatic sensitization of nanocrystalline TiO₂ films by a black dye based on a trithiocyanato-ruthenium complex. *Chem. Commun.* 1997, 1705-1706.
 39. Islam, A.; Sugihara, H.; Yanagida, M.; Hara, K.; Fujihashi, G.; Tachibana, Y.; Katoh, R.; Murata, S.; Arakawa, H. Efficient panchromatic sensitization of nanocrystalline TiO₂ films by β-diketonato ruthenium polypyridyl complexes. *New. J. Chem.* 2002, 26, 966-968.
 40. Yamaguchi, T.; Uchida, Y.; Agatsuma, S.; Arakawa, H. Series-connected tandem dye-sensitized solar cell for improving efficiency to more than 10%. *Sol. Energ. Mat. Sol. C.* 2009, 93, 733-736.
 41. Yanagida, M.; Onozawa-Komatsuzaki, N.; Kurashige, M.; Sayama, K.; Sugihara, H. Optimization of tandem-structured dye-sensitized solar cell. *Sol. Energ. Mat. Sol. C.* 2010, 94, 297-302.
 42. Ehret, A.; Stuhl, L.; Spitler, M. T. Spectral Sensitization of TiO₂ Nanocrystalline Electrodes with Aggregated Cyanine Dyes. *J. Phys. Chem. B* 2001, 105, 9960-9965.
 43. Deng, H.; Lu, Z.; Mao, H.; Shen, Y. Cosensitization and photoelectric conversion of a nanostructured TiO₂ electrode with tetrasulfonated porphyrins. *J. Chem. Soc. Faraday Trans.* 1998, 94, 659-663.
 44. Deng, H.; Zhang, H.; Liang, B.; Lu, Z. Improvement in photoelectric conversion of a

nanostructured TiO₂ electrode cosensitized with phthalocyanine and porphyrin. *Jpn. J. Appl. Phys., Part 2* 1998, 37, L132-L135.

45. Inakazu, F.; Noma, Y.; Ogomi, Y.; Hayase, S. Dye-sensitized solar cells consisting of dye-bilayer structure stained with two dyes for harvesting light of wide range of wavelength. *Appl. Phys. Lett.* 2008, 93.

46. Noma, Y.; Iizuka, K.; Ogomi, Y.; Pandey, S. S.; Hayase, S. Preparation of double dye-layer structure of dye-sensitized solar cells from cocktail solutions for harvesting light in wide range of wavelengths. *Jpn. J. Appl. Phys.* 2009, 48.

47. Clifford, J. N.; Palomares, E.; Nazeeruddin, M. K.; Thampi, R.; Grätzel, M.; Durrant, J. R. Multistep Electron Transfer Processes on Dye Co-sensitized Nanocrystalline TiO₂ Films. *J. Am. Chem. Soc.* 2004, 126, 5670-5671.

48. Dürr, M.; Schmid, A.; Obermaier, M.; Rosselli, S.; Yasuda, A.; Nelles, G. Low-temperature fabrication of dye-sensitized solar cells by transfer of composite porous layers. *Nat. Mater.* 2005, 4, 607-611.

49. Choi, H.; Kim, S.; Kang, S. O.; Ko, J.; Kang, M.-S.; Clifford, J. N.; Forneli, A.; Palomares, E.; Nazeeruddin, M. K.; Grätzel, M. Stepwise Cosensitization of Nanocrystalline TiO₂ Films Utilizing Al₂O₃ Layers in Dye-Sensitized Solar Cells. *Angew. Chem. Int. Ed.* 2008, 47, 8259-8263.

50. Lee, K.; Park, S. W.; Ko, M. J.; Kim, K.; Park, N. G. Selective positioning of organic dyes in a mesoporous inorganic oxide film. *Nat. Mater.* 2009, 8, 665-671.

51. Miao, Q.; Wu, L.; Cui, J.; Huang, M.; Ma, T. A new type of dye-sensitized solar cell with a multilayered photoanode prepared by a film-transfer technique. *Advanced Materials* 2011, 23, 2764-2768.

52. Huang, F.; Chen, D.; Cao, L.; Caruso, R. A.; Cheng, Y.-B. Flexible dye-sensitized solar cells containing multiple dyes in discrete layers. *Energy Environ. Sci.* 2011, 4, 2803-2806.

53. Yang, G. J.; Fan, S. Q.; Li, C. J.; Li, C. X. Layer-by-layer fabrication of multiple-dye-sensitized TiO₂ films for dye-sensitized solar cells by vacuum cold spray. *Nanosci. Nanotechnol. Lett.* 2011, 3, 483-486.

54. Lan, C.-M.; Wu, H.-P.; Pan, T.-Y.; Chang, C.-W.; Chao, W.-S.; Chen, C.-T.; Wang, C.-L.; Lin, C.-Y.; Diau, E. W.-G. Enhanced photovoltaic performance with co-sensitization of porphyrin and an organic dye in dye-sensitized solar cells. *Energy Environ. Sci.* 2012, 5, 6460-6464.

55. Huang, F.; Chen, D.; Cao, L.; Caruso, R. A.; Cheng, Y. B. Flexible dye-sensitized solar cells containing multiple dyes in discrete layers. *Energy Environ. Sci.* 2011, 4, 2803-2806.

56. Kuang, D.; Walter, P.; Nüesch, F.; Kim, S.; Ko, J.; Comte, P.; Zakeeruddin, S. M.; Nazeeruddin, M. K.; Grätzel, M. Co-sensitization of Organic Dyes for Efficient Ionic Liquid Electrolyte-Based Dye-Sensitized Solar Cells. *Langmuir* 2007, 23, 10906-10909.

57. Yum, J. H.; Jang, S. R.; Walter, P.; Geiger, T.; Nüesch, F.; Kim, S.; Ko, J.; Grätzel, M.; Nazeeruddin, M. K. Efficient co-sensitization of nanocrystalline TiO₂ films by organic sensitizers. *Chem. Commun.*

2007, 4680-4682.

58. Wang, Y.; Wu, M.; Lin, X.; Shi, Z.; Hagfeldt, A.; Ma, T. Several highly efficient catalysts for Pt-free and FTO-free counter electrodes of dye-sensitized solar cells. *J. Mater. Chem.* 2012, 22, 4009-4014.
59. Wu, M.; Lin, X.; Wang, Y.; Wang, L.; Guo, W.; Qi, D.; Peng, X.; Hagfeldt, A.; Grätzel, M.; Ma, T. Economical Pt-free catalysts for counter electrodes of dye-sensitized solar cells. *J. Am. Chem. Soc.* 2012, 134, 3419-3428.
60. Xu, H.; Zhang, X.; Zhang, C.; Liu, Z.; Zhou, X.; Pang, S.; Chen, X.; Dong, S.; Zhang, Z.; Zhang, L.; Han, P.; Wang, X.; Cui, G. Nanostructured titanium nitride/PEDOT:PSS composite films as counter electrodes of dye-sensitized solar cells. *ACS Appl. Mater. Inter.* 2012, 4, 1087-1092.
61. Zhang, X.; Chen, X.; Dong, S.; Liu, Z.; Zhou, X.; Yao, J.; Pang, S.; Xu, H.; Zhang, Z.; Li, L.; Cui, G. Hierarchical micro/nano-structured titanium nitride spheres as a high-performance counter electrode for a dye-sensitized solar cell. *J. Mater. Chem.* 2012, 22, 6067-6071.
62. Yun, S.; Zhou, H.; Wang, L.; Zhang, H.; Ma, T. Economical hafnium oxygen nitride binary/ternary nanocomposite counter electrode catalysts for high-efficiency dye-sensitized solar cells. *J. Mater. Chem. A* 2013, 1, 1341-1348.
63. Zhang, X.; Chen, X.; Zhang, K.; Pang, S.; Zhou, X.; Xu, H.; Dong, S.; Han, P.; Zhang, Z.; Zhang, C.; Cui, G. Transition-metal nitride nanoparticles embedded in N-doped reduced graphene oxide: Superior synergistic electrocatalytic materials for the counter electrodes of dye-sensitized solar cells. *J. Mater. Chem. A* 2013, 1, 3340-3346.
64. Jang, J. S.; Ham, D. J.; Ramasamy, E.; Lee, J.; Lee, J. S. Platinum-free tungsten carbides as an efficient counter electrode for dye sensitized solar cells. *Chem. Commun.* 2010, 46, 8600-8602.
65. Ko, A. R.; Oh, J. K.; Lee, Y. W.; Han, S. B.; Park, K. W. Characterizations of tungsten carbide as a non-Pt counter electrode in dye-sensitized solar cells. *Mater. Lett.* 2011, 65, 2220-2223.
66. Wu, M.; Lin, X.; Hagfeldt, A.; Ma, T. Low-cost molybdenum carbide and tungsten carbide counter electrodes for dye-sensitized solar cells. *Angew. Chem. Int. Ed.* 2011, 50, 3520-3524.
67. Wu, M.; Mu, L.; Wang, Y.; Lin, Y. N.; Guo, H.; Ma, T. One-step synthesis of nano-scaled tungsten oxides and carbides for dye-sensitized solar cells as counter electrode catalysts. *J. Mater. Chem. A* 2013, 1, 7519-7524.
68. Yun, S.; Wang, L.; Zhao, C.; Wang, Y.; Ma, T. A new type of low-cost counter electrode catalyst based on platinum nanoparticles loaded onto silicon carbide (Pt/SiC) for dye-sensitized solar cells. *PCCP* 2013, 15, 4286-4290.
69. Yun, S.; Zhang, H.; Pu, H.; Chen, J.; Hagfeldt, A.; Ma, T. Metal oxide/carbide/carbon nanocomposites: In situ synthesis, characterization, calculation, and their application as an efficient counter electrode catalyst for dye-sensitized solar cells. *Adv. Energy Mater.* 2013, 3, 1407-1412.
70. Wang, M.; Anghel, A. M.; Marsan, B.; Ha, N. L. C.; Pootrakulchote, N.; Zakeeruddin, S. M.; Grätzel, M. CoS supersedes Pt as efficient electrocatalyst for triiodide reduction in dye-sensitized

solar cells. *J. Am. Chem. Soc.* 2009, 131, 15976-15977.

71. Li, L.; Yang, X.; Zhao, J.; Gao, J.; Hagfeldt, A.; Sun, L. Efficient organic dye sensitized solar cells based on modified sulfide/polysulfide electrolyte. *J. Mater. Chem.* 2011, 21, 5573-5575.
72. Xin, X.; He, M.; Han, W.; Jung, J.; Lin, Z. Low-cost copper zinc tin sulfide counter electrodes for high-efficiency dye-sensitized solar cells. *Angew. Chem. Int. Ed.* 2011, 50, 11739-11742.
73. Burschka, J.; Brault, V.; Ahmad, S.; Breau, L.; Nazeeruddin, M. K.; Marsan, B.; Zakeeruddin, S. M.; Grätzel, M. Influence of the counter electrode on the photovoltaic performance of dye-sensitized solar cells using a disulfide/thiolate redox electrolyte. *Energy Environ. Sci.* 2012, 5, 6089-6097.
74. Wu, M.; Ma, T. Platinum-free catalysts as counter electrodes in dye-sensitized solar cells. *ChemSusChem* 2012, 5, 1343-1357.
75. Zhang, L.; Mulmudi, H. K.; Batabyal, S. K.; Lam, Y. M.; Mhaisalkar, S. G. Metal/metal sulfide functionalized single-walled carbon nanotubes: FTO-free counter electrodes for dye sensitized solar cells. *PCCP* 2012, 14, 9906-9911.
76. Bi, H.; Zhao, W.; Sun, S.; Cui, H.; Lin, T.; Huang, F.; Xie, X.; Jiang, M. Graphene films decorated with metal sulfide nanoparticles for use as counter electrodes of dye-sensitized solar cells. *Carbon* 2013, 61, 116-123.
77. Tai, S. Y.; Chang, C. F.; Liu, W. C.; Liao, J. H.; Lin, J. Y. Optically transparent counter electrode for dye-sensitized solar cells based on cobalt sulfide nanosheet arrays. *Electrochim. Acta* 2013, 107, 66-70.
78. Zhao, W.; Zhu, X.; Bi, H.; Cui, H.; Sun, S.; Huang, F. Novel two-step synthesis of NiS nanoplatelet arrays as efficient counter electrodes for dye-sensitized solar cells. *J. Power Sources* 2013, 242, 28-32.
79. Ji, I. A.; Choi, H. M.; Bang, J. H. Metal selenide films as the counter electrode in dye-sensitized solar cell. *Mater. Lett.* 2014, 123, 51-54.
80. Novoselov, K. S.; Geim, A. K.; Morozov, S. V.; Jiang, D.; Zhang, Y.; Dubonos, S. V.; Grigorieva, I. V.; Firsov, A. A. Electric Field Effect in Atomically Thin Carbon Films. *Science* 2004, 306, 666-669.
81. Du, X.; Skachko, I.; Barker, A.; Andrei, E. Y. Approaching ballistic transport in suspended graphene. *Nat. Nanotechnol.* 2008, 3, 491-495.
82. Unarunotai, S.; Murata, Y.; Chialvo, C. E.; Mason, N.; Petrov, I.; Nuzzo, R. G.; Moore, J. S.; Rogers, J. A. Conjugated Carbon Monolayer Membranes: Methods for Synthesis and Integration. *Adv. Mater.* 2010, 22, 1072-1077.
83. Nair, R. R.; Blake, P.; Grigorenko, A. N.; Novoselov, K. S.; Booth, T. J.; Stauber, T.; Peres, N. M. R.; Geim, A. K. Fine Structure Constant Defines Visual Transparency of Graphene. *Science* 2008, 320, 1308.
84. Peigney, A.; Laurent, C.; Flahaut, E.; Bacsá, R. R.; Rousset, A. Specific surface area of carbon nanotubes and bundles of carbon nanotubes. *Carbon* 2001, 39, 507-514.
85. Deng, J.-h.; Zheng, R.-t.; Zhao, Y.; Cheng, G.-a. Vapor-Solid Growth of Few-Layer Graphene

Using Radio Frequency Sputtering Deposition and Its Application on Field Emission. *ACS Nano* 2012, 6, 3727-3733.

86. Hu, Y. H.; Wang, H.; Hu, B. Thinnest Two-Dimensional Nanomaterial—Graphene for Solar Energy. *ChemSusChem* 2010, 3, 782-796.

87. Sun, Y.; Wu, Q.; Shi, G. Graphene based new energy materials. *Energy Environ. Sci.* 2011, 4, 1113-1132.

88. Sun, Y.; Hu, X.; Luo, W.; Huang, Y. Self-Assembled Hierarchical MoO₂/Graphene Nanoarchitectures and Their Application as a High-Performance Anode Material for Lithium-Ion Batteries. *ACS Nano* 2011, 5, 7100-7107.

89. Mishra, A. K.; Ramaprabhu, S. Functionalized Graphene-Based Nanocomposites for Supercapacitor Application. *J. Phys. Chem. C* 2011, 115, 14006-14013.

90. Radich, J. G.; Dwyer, R.; Kamat, P. V. Cu₂S Reduced Graphene Oxide Composite for High-Efficiency Quantum Dot Solar Cells. Overcoming the Redox Limitations of S²⁻/Sn²⁻ at the Counter Electrode. *J. Phys. Chem. Lett.* 2011, 2, 2453-2460.

91. Kaniyoor, A.; Ramaprabhu, S. Thermally exfoliated graphene based counter electrode for low cost dye sensitized solar cells. *J. Appl. Phys.* 2011, 109, -.

92. Yen, M.-Y.; Hsieh, C.-K.; Teng, C.-C.; Hsiao, M.-C.; Liu, P.-I.; Ma, C.-C. M.; Tsai, M.-C.; Tsai, C.-H.; Lin, Y.-R.; Chou, T.-Y. Metal-free, nitrogen-doped graphene used as a novel catalyst for dye-sensitized solar cell counter electrodes. *RSC Adv.* 2012, 2, 2725-2728.

93. Wang, H.; Hu, Y. H. Graphene as a counter electrode material for dye-sensitized solar cells. *Energy Environ. Sci.* 2012, 5, 8182-8188.

94. Tjoa, V.; Chua, J.; Pramana, S. S.; Wei, J.; Mhaisalkar, S. G.; Mathews, N. Facile Photochemical Synthesis of Graphene-Pt Nanoparticle Composite for Counter Electrode in Dye Sensitized Solar Cell. *ACS Appl. Mater. Inter.* 2012, 4, 3447-3452.

95. Roy-Mayhew, J. D.; Boschloo, G.; Hagfeldt, A.; Aksay, I. A. Functionalized Graphene Sheets as a Versatile Replacement for Platinum in Dye-Sensitized Solar Cells. *ACS Appl. Mater. Inter.* 2012, 4, 2794-2800.

96. Kaniyoor, A.; Ramaprabhu, S. Soft functionalization of graphene for enhanced tri-iodide reduction in dye sensitized solar cells. *J. Mater. Chem.* 2012, 22, 8377-8384.

97. Jang, S.-Y.; Kim, Y.-G.; Kim, D. Y.; Kim, H.-G.; Jo, S. M. Electrostatically Sprayed Thin Films of Aqueous Dispersible Graphene Nanosheets: Highly Efficient Cathodes for Dye-Sensitized Solar Cells. *ACS Appl. Mater. Inter.* 2012, 4, 3500-3507.

98. Hsieh, C. T.; Yang, B. H.; Lin, J. Y. One- and two-dimensional carbon nanomaterials as counter electrodes for dye-sensitized solar cells. *Carbon* 2011, 49, 3092-3097.

99. Han, J.; Kim, H.; Kim, D. Y.; Jo, S. M.; Jang, S.-Y. Water-Soluble Polyelectrolyte-Grafted Multiwalled Carbon Nanotube Thin Films for Efficient Counter Electrode of Dye-Sensitized Solar Cells. *ACS Nano* 2010, 4, 3503-3509.

100. Dong, P.; Pint, C. L.; Hailey, M.; Mirri, F.; Zhan, Y.; Zhang, J.; Pasquali, M.; Hauge, R. H.; Verduzco, R.; Jiang, M.; Lin, H.; Lou, J. Vertically Aligned Single-Walled Carbon Nanotubes as Low-cost and High Electrocatalytic Counter Electrode for Dye-Sensitized Solar Cells. *ACS Appl. Mater. Inter.* 2011, 3, 3157-3161.
101. Siroroj, S.; Pimanpang, S.; Towannang, M.; Maiaugree, W.; Phumying, S.; Jarernboon, W.; Amornkitbamrung, V. High performance dye-sensitized solar cell based on hydrothermally deposited multiwall carbon nanotube counter electrode. *Appl. Phys. Lett.* 2012, 100, -.
102. Cha, S. I.; Koo, B. K.; Seo, S. H.; Lee, D. Y. Pt-free transparent counter electrodes for dye-sensitized solar cells prepared from carbon nanotube micro-balls. *J. Mater. Chem.* 2010, 20, 659-662.
103. Lee, W. J.; Ramasamy, E.; Lee, D. Y.; Song, J. S. Efficient Dye-Sensitized Solar Cells with Catalytic Multiwall Carbon Nanotube Counter Electrodes. *ACS Appl. Mater. Inter.* 2009, 1, 1145-1149.
104. Mei, X.; Jen Cho, S.; Fan, B.; Ouyang, J. High-performance dye-sensitized solar cells with gel-coated binder-free carbon nanotube films as counter electrode. *Nanotechnology* 2010, 21.
105. Lee, K. S.; Lee, W. J.; Park, N.-G.; Kim, S. O.; Park, J. H. Transferred vertically aligned N-doped carbon nanotube arrays: use in dye-sensitized solar cells as counter electrodes. *Chem. Commun.* 2011, 47, 4264-4266.
106. Yang, Z.; Chen, T.; He, R.; Guan, G.; Li, H.; Qiu, L.; Peng, H. Aligned Carbon Nanotube Sheets for the Electrodes of Organic Solar Cells. *Adv. Mater.* 2011, 23, 5436-5439.
107. Veerappan, G.; Bojan, K.; Rhee, S. W. Amorphous carbon as a flexible counter electrode for low cost and efficient dye sensitized solar cell. *Renew. Energ.* 2012, 41, 383-388.
108. Sudhagar, P.; Ramasamy, E.; Cho, W. H.; Lee, J.; Kang, Y. S. Robust mesocellular carbon foam counter electrode for quantum-dot sensitized solar cells. *Electrochem. Commun.* 2011, 13, 34-37.
109. Kang, D.-Y.; Lee, Y.; Cho, C.-Y.; Moon, J. H. Inverse Opal Carbons for Counter Electrode of Dye-Sensitized Solar Cells. *Langmuir* 2012, 28, 7033-7038.
110. Jiang, Q. W.; Li, G. R.; Wang, F.; Gao, X. P. Highly ordered mesoporous carbon arrays from natural wood materials as counter electrode for dye-sensitized solar cells. *Electrochem. Commun.* 2010, 12, 924-927.
111. Ramasamy, E.; Chun, J.; Lee, J. Soft-template synthesized ordered mesoporous carbon counter electrodes for dye-sensitized solar cells. *Carbon* 2010, 48, 4563-4565.
112. Zhao, B.; Huang, H.; Jiang, P.; Zhao, H.; Huang, X.; Shen, P.; Wu, D.; Fu, R.; Tan, S. Flexible Counter Electrodes Based on Mesoporous Carbon Aerogel for High-Performance Dye-Sensitized Solar Cells. *J. Phys. Chem. C* 2011, 115, 22615-22621.
113. Balis, N.; Makris, T.; Dracopoulos, V.; Stergiopoulos, T.; Lianos, P. Quasi-Solid-State Dye-Sensitized Solar Cells made with poly(3,4-ethylenedioxythiophene)-functionalized counter-electrodes. *J. Power Sources* 2011.
114. Pringle, J. M.; Armel, V.; MacFarlane, D. R. Electrodeposited PEDOT-on-plastic cathodes for dye-sensitized solar cells. *Chem. Commun.* 2010, 46, 5367-5369.

115. Chen, J. G.; Wei, H. Y.; Ho, K. C. Using modified poly(3,4-ethylene dioxythiophene): Poly(styrene sulfonate) film as a counter electrode in dye-sensitized solar cells. *Sol. Energ. Mat. Sol. C.* 2007, 91, 1472-1477.
116. Li, Z.; Ye, B.; Hu, X.; Ma, X.; Zhang, X.; Deng, Y. Facile electropolymerized-PANI as counter electrode for low cost dye-sensitized solar cell. *Electrochem. Commun.* 2009, 11, 1768-1771.
117. Huang, K.-C.; Hu, C.-W.; Tseng, C.-Y.; Liu, C.-Y.; Yeh, M.-H.; Wei, H.-Y.; Wang, C.-C.; Vittal, R.; Chu, C.-W.; Ho, K.-C. A counter electrode based on hollow spherical particles of polyaniline for a dye-sensitized solar cell. *J. Mater. Chem.* 2012, 22, 14727-14733.
118. Cho, S.; Hwang, S. H.; Kim, C.; Jang, J. Polyaniline porous counter-electrodes for high performance dye-sensitized solar cells. *J. Mater. Chem.* 2012, 22, 12164-12171.
119. Peng, S.; Zhu, P.; Wu, Y.; Mhaisalkar, S. G.; Ramakrishna, S. Electrospun conductive polyaniline-poly(lactic acid) composite nanofibers as counter electrodes for rigid and flexible dye-sensitized solar cells. *RSC Adv.* 2012, 2, 652-657.
120. Tai, Q.; Chen, B.; Guo, F.; Xu, S.; Hu, H.; Sebo, B.; Zhao, X. Z. In situ prepared transparent polyaniline electrode and its application in bifacial dye-sensitized solar cells. *ACS Nano* 2011, 5, 3795-3799.
121. Kim, J.-Y.; Lee, K. J.; Kang, S. H.; Shin, J.; Sung, Y.-E. Enhanced Photovoltaic Properties of a Cobalt Bipyridyl Redox Electrolyte in Dye-Sensitized Solar Cells Employing Vertically Aligned TiO₂ Nanotube Electrodes. *J. Phys. Chem. C* 2011, 115, 19979-19985.
122. Lee, K.-M.; Hsu, C.-Y.; Chen, P.-Y.; Ikegami, M.; Miyasaka, T.; Ho, K.-C. Highly porous PProDOT-Et₂ film as counter electrode for plastic dye-sensitized solar cells. *PCCP* 2009, 11, 3375-3379.
123. Jeon, S. S.; Kim, C.; Ko, J.; Im, S. S. Spherical polypyrrole nanoparticles as a highly efficient counter electrode for dye-sensitized solar cells. *J. Mater. Chem.* 2011, 21, 8146-8151.
124. Wu, J.; Li, Q.; Fan, L.; Lan, Z.; Li, P.; Lin, J.; Hao, S. High-performance polypyrrole nanoparticles counter electrode for dye-sensitized solar cells. *J. Power Sources* 2008, 181, 172-176.
125. Tian, H.; Yu, Z.; Hagfeldt, A.; Kloo, L.; Sun, L. Organic redox couples and organic counter electrode for efficient organic dye-sensitized solar cells. *J. Am. Chem. Soc.* 2011, 133, 9413-9422.
126. Burschka, J.; Brault, V.; Ahmad, S.; Breau, L.; Nazeeruddin, M. K.; Marsan, B.; Zakeeruddin, S. M.; Grätzel, M. Influence of the counter electrode on the photovoltaic performance of dye-sensitized solar cells using a disulfide/thiolate redox electrolyte. *Energy Environ. Sci.* 2012, 5, 6089-6097.
127. Ahmad, S.; Yum, J.-H.; Butt, H.-J.; Nazeeruddin, M. K.; Grätzel, M. Efficient Platinum-Free Counter Electrodes for Dye-Sensitized Solar Cell Applications. *ChemPhysChem* 2010, 11, 2814-2819.
128. Yum, J. H.; Baranoff, E.; Kessler, F.; Moehl, T.; Ahmad, S.; Bessho, T.; Marchioro, A.; Ghadiri, E.; Moser, J. E.; Yi, C.; Nazeeruddin, M. K.; Grätzel, M. A cobalt complex redox shuttle for dye-sensitized solar cells with high open-circuit potentials. *Nat. Commun.* 2012, 3.
129. Shi, C.; Zhu, A. M.; Yang, X. F.; Au, C. T. On the catalytic nature of VN, Mo₂N, and W₂N nitrides for NO reduction with hydrogen. *Appl. Catal. A - Gen.* 2004, 276, 223-230.

130. Furimsky, E. Metal carbides and nitrides as potential catalysts for hydroprocessing. *Appl. Catal. A - Gen.* 2003, 240, 1-28.
131. Jiang, Q. W.; Li, G. R.; Gao, X. P. Highly ordered TiN nanotube arrays as counter electrodes for dye-sensitized solar cells. *Chem. Commun.* 2009, 6720-6722.
132. Li, G.-r.; Wang, F.; Jiang, Q.-w.; Gao, X.-p.; Shen, P.-w. Carbon Nanotubes with Titanium Nitride as a Low-Cost Counter-Electrode Material for Dye-Sensitized Solar Cells. *Angew. Chem. Int. Ed.* 2010, 49, 3653-3656.
133. Wu, M.; Zhang, Q.; Xiao, J.; Ma, C.; Lin, X.; Miao, C.; He, Y.; Gao, Y.; Hagfeldt, A.; Ma, T. Two flexible counter electrodes based on molybdenum and tungsten nitrides for dye-sensitized solar cells. *J. Mater. Chem.* 2011, 21, 10761-10766.
134. Jiang, Q. W.; Li, G. R.; Liu, S.; Gao, X. P. Surface-Nitrided Nickel with Bifunctional Structure As Low-Cost Counter Electrode for Dye-Sensitized Solar Cells. *J. Phys. Chem. C* 2010, 114, 13397-13401.
135. Li, G. R.; Wang, F.; Song, J.; Xiong, F. Y.; Gao, X. P. TiN-conductive carbon black composite as counter electrode for dye-sensitized solar cells. *Electrochim. Acta* 2012, 65, 216-220.
136. Ramasamy, E.; Jo, C.; Anthonysamy, A.; Jeong, I.; Kim, J. K.; Lee, J. Soft-Template Simple Synthesis of Ordered Mesoporous Titanium Nitride-Carbon Nanocomposite for High Performance Dye-Sensitized Solar Cell Counter Electrodes. *Chem. Mater.* 2012, 24, 1575-1582.
137. Deng, H.; Mao, H.; Lu, Z.; Li, J.; Xu, H. Cosensitization of a nanostructured TiO₂ electrode with tetrasulfonated gallium phthalocyanine and tetrasulfonated zinc porphyrin. *J. Photochem. Photobiol., A* 1997, 110, 47-52.
138. Balasingam, S. K.; Lee, M.; Kang, M. G.; Jun, Y. Improvement of dye-sensitized solar cells toward the broader light harvesting of the solar spectrum. *Chem. Commun.* 2013, 49, 1471-1487.
139. Ehret, A.; Stuhl, L.; Spitler, M. T. Spectral sensitization of TiO₂ nanocrystalline electrodes with aggregated cyanine dyes. *Journal of Physical Chemistry B* 2001, 105, 9960-9965.
140. Ogura, R. Y.; Nakane, S.; Morooka, M.; Orihashi, M.; Suzuki, Y.; Noda, K. High-performance dye-sensitized solar cell with a multiple dye system. *Appl. Phys. Lett.* 2009, 94.
141. Zhao, W.; Jun Hou, Y.; Song Wang, X.; Wen Zhang, B.; Cao, Y.; Yang, R.; Bo Wang, W.; Rui Xiao, X. Study on squarylium cyanine dyes for photoelectric conversion. *Sol. Energ. Mat. Sol. C* 1999, 58, 173-183.
142. Choi, H.; Kim, S.; Kang, S. O.; Ko, J.; Kang, M. S.; Clifford, J. N.; Forneli, A.; Palomares, E.; Nazeeruddin, M. K.; Grätzel, M. Stepwise cosensitization of nanocrystalline TiO₂ films utilizing Al₂O₃ layers in dye-sensitized solar cells. *Angew. Chem. Int. Ed.* 2008, 47, 8259-8263.
143. Lan, C. M.; Wu, H. P.; Pan, T. Y.; Chang, C. W.; Chao, W. S.; Chen, C. T.; Wang, C. L.; Lin, C. Y.; Diao, E. W. G. Enhanced photovoltaic performance with co-sensitization of porphyrin and an organic dye in dye-sensitized solar cells. *Energy Environ. Sci.* 2012, 5, 6460-6464.
144. Dürr, M.; Bamedi, A.; Yasuda, A.; Nelles, G. Tandem dye-sensitized solar cell for improved

power conversion efficiencies. *Appl. Phys. Lett.* 2004, 84, 3397-3399.

145. Lee, B. K.; Kim, J. J. Enhanced efficiency of dye-sensitized solar cells by UV-O₃ treatment of TiO₂ layer. *Curr. Appl Phys.* 2009, 9, 404-408.

146. Wu, F.; Yue, W.; Cui, Q.; Liu, C.; Qiu, Z.; Shen, W.; Zhang, H.; Wang, M. Performance correlated with device layout and illumination area in solar cells based on polymer and aligned ZnO nanorods. *Sol. Energy* 2012, 86, 1459-1469.

147. Koo, H.-J.; Kim, K.; Park, N.-G.; Hwang, S.; Park, C.; Kim, C. Fabrication of heterosensitizer-junction dye-sensitized solar cells. *Appl. Phys. Lett.* 2008, 92, -.

148. Jang, Y. H.; Xin, X.; Byun, M.; Jang, Y. J.; Lin, Z.; Kim, D. H. An unconventional route to high-efficiency dye-sensitized solar cells via embedding graphitic thin films into TiO₂ nanoparticle photoanode. *Nano Lett.* 2012, 12, 479-485.

149. Yang, N.; Zhai, J.; Wang, D.; Chen, Y.; Jiang, L. Two-dimensional graphene bridges enhanced photoinduced charge transport in dye-sensitized solar cells. *ACS Nano* 2010, 4, 887-894.

150. Jo, Y.; Cheon, J. Y.; Yu, J.; Jeong, H. Y.; Han, C. H.; Jun, Y.; Joo, S. H. Highly interconnected ordered mesoporous carbon-carbon nanotube nanocomposites: Pt-free, highly efficient, and durable counter electrodes for dye-sensitized solar cells. *Chem. Commun.* 2012, 48, 8057-8059.

151. Kavan, L.; Yum, J. H.; Grätzel, M. Optically transparent cathode for dye-sensitized solar cells based on graphene nanoplatelets. *ACS Nano* 2011, 5, 165-172.

152. Lim, J.; Ryu, S. Y.; Kim, J.; Jun, Y. A study of TiO₂/carbon black composition as counter electrode materials for dye-sensitized solar cells. *Nanoscale Res. Lett.* 2013, 8, 1-5.

153. Wu, H. P.; Ou, Z. W.; Pan, T. Y.; Lan, C. M.; Huang, W. K.; Lee, H. W.; Reddy, N. M.; Chen, C. T.; Chao, W. S.; Yeh, C. Y.; Diau, E. W. G. Molecular engineering of cocktail co-sensitization for efficient panchromatic porphyrin-sensitized solar cells. *Energy Environ. Sci.* 2012, 5, 9843-9848.

154. Lim, J.; Lee, M.; Balasingam, S. K.; Kim, J.; Kim, D.; Jun, Y. Fabrication of panchromatic dye-sensitized solar cells using pre-dye coated TiO₂ nanoparticles by a simple dip coating technique. *RSC Adv.* 2013, 3, 4801-4805.

155. Wu, M. S.; Tsai, C. H.; Jow, J. J.; Wei, T. C. Enhanced performance of dye-sensitized solar cell via surface modification of mesoporous TiO₂ photoanode with electrodeposited thin TiO₂ layer. *Electrochim. Acta* 2011, 56, 8906-8911.

156. Jo, Y.; Jung, C. L.; Lim, J.; Kim, B. H.; Han, C. H.; Kim, J.; Kim, S.; Kim, D.; Jun, Y. A novel dye coating method for N719 dye-sensitized solar cells. *Electrochim. Acta* 2012, 66, 121-125.

157. Wang, H.; Liu, Y.; Xu, H.; Dong, X.; Shen, H.; Wang, Y.; Yang, H. An investigation on the novel structure of dye-sensitized solar cell with integrated photoanode. *Renew. Energ.* 2009, 34, 1635-1638.

158. Goto, K.; Kawashima, T.; Tanabe, N. Heat-resisting TCO films for PV cells. *Sol. Energ. Mat. Sol. C.* 2006, 90, 3251-3260.

159. Sima, C.; Grigoriu, C.; Antohe, S. Comparison of the dye-sensitized solar cells performances

based on transparent conductive ITO and FTO. *Thin Solid Films* 2010, 519, 595-597.

160. Zumeta, I.; Ayllón, J. A.; González, B.; Domenech, X.; Vigil, E. TiO₂ films obtained by microwave-activated chemical-bath deposition used to improve TiO₂-conducting glass contact. *Sol. Energ. Mat. Sol. C.* 2009, 93, 1728-1732.
161. Miyasaka, T.; Kijitori, Y. Low-temperature fabrication of dye-sensitized plastic electrodes by electrophoretic preparation of mesoporous TiO₂ layers. *J. Electrochem. Soc.* 2004, 151, A1767-A1773.
162. Yoo, B.; Kim, K.; Lee, S. H.; Kim, W. M.; Park, N.-G. ITO/ATO/TiO₂ triple-layered transparent conducting substrates for dye-sensitized solar cells. *Sol. Energ. Mat. Sol. C.* 2008, 92, 873-877.
163. Park, J. H.; Jun, Y.; Yun, H. G.; Lee, S. Y.; Kang, M. G. Fabrication of an efficient dye-sensitized solar cell with stainless steel substrate. *J. Electrochem. Soc.* 2008, 155, F145-F149.
164. Su, Z.; Yan, C.; Tang, D.; Sun, K.; Han, Z.; Liu, F.; Lai, Y.; Li, J.; Liu, Y. Fabrication of Cu₂ZnSnS₄ nanowires and nanotubes based on AAO templates. *CrystEngComm* 2012, 14, 782-785.
165. Chang, J. K.; Liao, C. M.; Chen, C. H.; Tsai, W. T. Effect of electrolyte composition on hydration resistance of anodized aluminum oxide. *J. Power Sources* 2004, 138, 301-308.
166. Luo, Z.; Peng, A.; Fu, H.; Ma, Y.; Yao, J.; Loo, B. H. An application of AAO template: Orderly assembled organic molecules for surface-enhanced Raman scattering. *J. Mater. Chem.* 2008, 18, 133-138.
167. Taşaltın, N.; Öztürk, S.; Kilinç, N.; Yüzer, H.; Öztürk, Z. Z. Simple fabrication of hexagonally well-ordered AAO template on silicon substrate in two dimensions. *Appl. Phys. A - Mater.* 2009, 95, 781-787.
168. Park, S. H.; Kim, S.; Lee, D. J.; Yun, S.; Khim, Z. G.; Kim, K. B. Selective wet-chemical etching of the barrier layer during formation of porous anodic aluminum oxide template. *J. Electrochem. Soc.* 2009, 156, K181-K185.
169. Lillo, M.; Losic, D. Pore opening detection for controlled dissolution of barrier oxide layer and fabrication of nanoporous alumina with through-hole morphology. *J. Membr. Sci.* 2009, 327, 11-17.
170. Zaraska, L.; Sulka, G. D.; Szeremeta, J.; Jaskuła, M. Porous anodic alumina formed by anodization of aluminum alloy (AA1050) and high purity aluminum. *Electrochim. Acta* 2010, 55, 4377-4386.
171. Liu, P.; Singh, V. P.; Rajaputra, S. Barrier layer non-uniformity effects in anodized aluminum oxide nanopores on ITO substrates. *Nanotechnology* 2010, 21.
172. Masuda, H.; Fukuda, K. Ordered metal nanohole arrays made by a two-step replication of honeycomb structures of anodic alumina. *Science* 1995, 268, 1466-1468.
173. Shin, S. S.; Kim, J. S.; Suk, J. H.; Lee, K. D.; Kim, D. W.; Park, J. H.; Cho, I. S.; Hong, K. S.; Kim, J. Y. Improved Quantum Efficiency of Highly Efficient Perovskite BaSnO₃-Based Dye-Sensitized Solar Cells. *ACS Nano* 2013, 7, 1027-1035.
174. Kim, D. W.; Shin, S. S.; Lee, S.; Cho, I. S.; Kim, D. H.; Lee, C. W.; Jung, H. S.; Hong, K. S. BaSnO₃

- Perovskite nanoparticles for high efficiency dye-sensitized solar cells. *ChemSusChem* 2013, 6, 449-454.
175. Ito, S.; Zakeeruddin, S. M.; Comte, P.; Liska, P.; Kuang, D.; Grätzel, M. Bifacial dye-sensitized solar cells based on an ionic liquid electrolyte. *Nature Photon.* 2008, 2, 693-698.
176. Grätzel, M. Photoelectrochemical cells. *Nature* 2001, 414, 338-344.
177. Wu, J.; Hao, S.; Lan, Z.; Lin, J.; Huang, M.; Huang, Y.; Li, P.; Yin, S.; Sato, T. An all-solid-state dye-sensitized solar cell-based poly(N-alkyl-4-vinyl- pyridine iodide) electrolyte with efficiency of 5.64%. *J. Am. Chem. Soc.* 2008, 130, 11568-11569.
178. Ramkumar, S.; Anandan, S. Synthesis of bianchored metal free organic dyes for dye sensitized solar cells. *Dyes Pigm.* 2013, 97, 397-404.
179. Fan, J.; Hao, Y.; Cabot, A.; Johansson, E. M. J.; Boschloo, G.; Hagfeldt, A. Cobalt(II/III) redox electrolyte in ZnO nanowire-based dye-sensitized solar cells. *ACS Appl. Mater. Inter.* 2013, 5, 1902-1906.
180. Kao, M. C.; Chen, H. Z.; Young, S. L.; Lin, C. C.; Kung, C. Y. Structure and photovoltaic properties of ZnO nanowire for dye-sensitized solar cells. *Nanoscale Res. Lett.* 2012, 7, 1-16.
181. Chiu, P. K.; Cho, W. H.; Chen, H. P.; Hsiao, C. N.; Yang, J. R. Study of a sandwich structure of transparent conducting oxide films prepared by electron beam evaporation at room temperature. *Nanoscale Res. Lett.* 2012, 7.
182. Powar, S.; Wu, Q.; Weidener, M.; Nattestad, A.; Hu, Z.; Mishra, A.; Bäuerle, P.; Spiccia, L.; Cheng, Y. B.; Bach, U. Improved photocurrents for p-type dye-sensitized solar cells using nanostructured nickel(ii) oxide microballs. *Energy Environ. Sci.* 2012, 5, 8896-8900.
183. Murakami, T. N.; Grätzel, M. Counter electrodes for DSC: Application of functional materials as catalysts. *Inorg. Chim. Acta* 2008, 361, 572-580.
184. Kamiya, K.; Nishijima, T.; Tanaka, K. Nitridation of the Sol-Gel-Derived Titanium Oxide Films by Heating in Ammonia Gas. *J. Am. Ceram. Soc.* 1990, 73, 2750-2752.
185. Choi, D.; Kumta, P. N. Synthesis of nanostructured TiN using a two-step transition metal halide approach. *J. Am. Ceram. Soc.* 2005, 88, 2030-2035.
186. Kaskel, S.; Schlichte, K.; Kratzke, T. Catalytic properties of high surface area titanium nitride materials. *J. Mol. Catal. A: Chem.* 2004, 208, 291-298.
187. Zhang, D. W.; Li, X. D.; Chen, S.; Tao, F.; Sun, Z.; Yin, X. J.; Huang, S. M. Fabrication of double-walled carbon nanotube counter electrodes for dye-sensitized solar cells. *J. Solid State Electrochem.* 2010, 14, 1541-1546.
188. Lee, W. J.; Ramasamy, E.; Lee, D. Y.; Song, J. S. Efficient dye-sensitized solar cells with catalytic multiwall carbon nanotube counter electrodes. *ACS Applied Materials and Interfaces* 2009, 1, 1145-1149.
189. Novoselov, K. S.; Geim, A. K.; Morozov, S. V.; Jiang, D.; Zhang, Y.; Dubonos, S. V.; Grigorieva, I. V.; Firsov, A. A. Electric field in atomically thin carbon films. *Science* 2004, 306, 666-669.

190. Ramasamy, E.; Lee, W. J.; Lee, D. Y.; Song, J. S. Nanocarbon counterelectrode for dye sensitized solar cells. *Appl. Phys. Lett.* 2007, 90.
191. Ramasamy, E.; Lee, W. J.; Lee, D. Y.; Song, J. S. Spray coated multi-wall carbon nanotube counter electrode for tri-iodide (I_3^-) reduction in dye-sensitized solar cells. *Electrochem. Commun.* 2008, 10, 1087-1089.
192. Wang, G.; Xing, W.; Zhuo, S. Application of mesoporous carbon to counter electrode for dye-sensitized solar cells. *J. Power Sources* 2009, 194, 568-573.
193. Joshi, P.; Xie, Y.; Ropp, M.; Galipeau, D.; Bailey, S.; Qiao, Q. Dye-sensitized solar cells based on low cost nanoscale carbon/TiO₂ composite counter electrode. *Energy Environ. Sci.* 2009, 2, 426-429.
194. Burnside, S. D.; Shklover, V.; Barbé, C.; Comte, P.; Arendse, F.; Brooks, K.; Grätzel, M. Self-Organization of TiO₂ Nanoparticles in Thin Films. *Chem. Mater.* 1998, 10, 2419-2425.
195. Hu, H.; Chen, B. L.; Bu, C. H.; Tai, Q. D.; Guo, F.; Xu, S.; Xu, J. H.; Zhao, X. Z. Stability study of carbon-based counter electrodes in dye-sensitized solar cells. *Electrochim. Acta* 2011, 56, 8463-8466.
196. Wang, Q.; Moser, J. E.; Grätzel, M. Electrochemical impedance spectroscopic analysis of dye-sensitized solar cells. *J. Phys. Chem. B* 2005, 109, 14945-14953.
197. Jung, C.-I.; Lim, J.; Park, J.-H.; Kim, K.-H.; Han, C.-H.; Jun, Y. High performance dye sensitized solar cells by adding titanate co-adsorbant. *RSC Adv.* 2013, 3, 20488-20491.
198. Lee, H.-S.; Bae, S.-H.; Jo, Y.; Kim, K.-J.; Jun, Y.; Han, C.-H. A high temperature stable electrolyte system for dye-sensitized solar cells. *Electrochim. Acta* 2010, 55, 7159-7165.
199. Jeon, S.; Jo, Y.; Kim, K.-J.; Jun, Y.; Han, C.-H. High Performance Dye-Sensitized Solar Cells with Alkylpyridinium Iodide Salts in Electrolytes. *ACS Appl. Mater. Inter.* 2011, 3, 512-516.
200. Kubo, W.; Kitamura, T.; Hanabusa, K.; Wada, Y.; Yanagida, S. Quasi-solid-state dye-sensitized solar cells using room temperature molten salts and a low molecular weight gelator. *Chem. Commun.* 2002, 374-375.
201. Kawano, R.; Watanabe, M. Equilibrium potentials and charge transport of an I^-/I_3^- redox couple in an ionic liquid. *Chem. Commun.* 2003, 330-331.
202. Wang, P.; Zakeeruddin, S. M.; Moser, J. E.; Nazeeruddin, M. K.; Sekiguchi, T.; Grätzel, M. A stable quasi-solid-state dye-sensitized solar cell with an amphiphilic ruthenium sensitizer and polymer gel electrolyte. *Nat. Mater.* 2003, 2, 402-407.
203. Cerneaux, S.; Zakeeruddin, S. M.; Pringle, J. M.; Cheng, Y. B.; Grätzel, M.; Spiccia, L. Novel Nano-Structured Silica-Based Electrolytes Containing Quaternary Ammonium Iodide Moieties. *Adv. Funct. Mater.* 2007, 17, 3200-3206.
204. Bach, U.; Lupo, D.; Comte, P.; Moser, J. E.; Weissörtel, F.; Salbeck, J.; Spreitzer, H.; Grätzel, M. Solid-state dye-sensitized mesoporous TiO₂ solar cells with high photon-to-electron conversion efficiencies. *Nature* 1998, 395, 583-585.
205. McDonald, S. A.; Konstantatos, G.; Zhang, S.; Cyr, P. W.; Klem, E. J. D.; Levina, L.; Sargent, E.

- H. Solution-processed PbS quantum dot infrared photodetectors and photovoltaics. *Nat. Mater.* 2005, 4, 138-142.
206. Milliron, D.; Hughes, S. M.; Cui, Y.; Manna, L.; Li, J.; Wang, L. W.; Alivisatos, A. P. Colloidal nanocrystal heterostructures with linear and branched topology. *Nature* 2004, 430, 190-195.
207. Nozik, A. J. Quantum dot solar cells. *Physica E: Low-dimensional Systems and Nanostructures* 2002, 14, 115-120.
208. Robel, I.; Subramanian, V.; Kuno, M.; Kamat, P. V. Quantum Dot Solar Cells. Harvesting Light Energy with CdSe Nanocrystals Molecularly Linked to Mesoscopic TiO₂ Films. *J. Am. Chem. Soc.* 2006, 128, 2385-2393.
209. Günes, S.; Neugebauer, H.; Sariciftci, N. S. Conjugated polymer-based organic solar cells. *Chem. Rev.* 2007, 107, 1324-1338.
210. Huynh, W. U.; Dittmer, J. J.; Alivisatos, A. P. Hybrid Nanorod-Polymer Solar Cells. *Science* 2002, 295, 2425-2427.
211. Scharber, M. C.; Mühlbacher, D.; Koppe, M.; Denk, P.; Waldauf, C.; Heeger, A. J.; Brabec, C. J. Design Rules for Donors in Bulk-Heterojunction Solar Cells—Towards 10 % Energy-Conversion Efficiency. *Adv. Mater.* 2006, 18, 789-794.
212. Thompson, B. C.; Fréchet, J. M. J. Polymer–Fullerene Composite Solar Cells. *Angew. Chem. Int. Ed.* 2008, 47, 58-77.
213. Snaith, H. J. Estimating the Maximum Attainable Efficiency in Dye-Sensitized Solar Cells. *Adv. Funct. Mater.* 2010, 20, 13-19.
214. Kojima, A.; Teshima, K.; Shirai, Y.; Miyasaka, T. Organometal Halide Perovskites as Visible-Light Sensitizers for Photovoltaic Cells. *J. Am. Chem. Soc.* 2009, 131, 6050-6051.
215. Kim, H. S.; Lee, C. R.; Im, J. H.; Lee, K. B.; Moehl, T.; Marchioro, A.; Moon, S. J.; Humphry-Baker, R.; Yum, J. H.; Moser, J. E.; Grätzel, M.; Park, N. G. Lead iodide perovskite sensitized all-solid-state submicron thin film mesoscopic solar cell with efficiency exceeding 9%. *Sci. Rep.* 2012, 2.
216. Lee, M. M.; Teuscher, J.; Miyasaka, T.; Murakami, T. N.; Snaith, H. J. Efficient Hybrid Solar Cells Based on Meso-Superstructured Organometal Halide Perovskites. *Science* 2012, 338, 643-647.
217. Eperon, G. E.; Burlakov, V. M.; Docampo, P.; Goriely, A.; Snaith, H. J. Morphological Control for High Performance, Solution-Processed Planar Heterojunction Perovskite Solar Cells. *Adv. Funct. Mater.* 2014, 24, 151-157.
218. Carnie, M. J.; Charbonneau, C.; Davies, M. L.; Troughton, J.; Watson, T. M.; Wojciechowski, K.; Snaith, H.; Worsley, D. A. A one-step low temperature processing route for organolead halide perovskite solar cells. *Chem. Commun.* 2013, 49, 7893-7895.
219. Heo, J. H.; Im, S. H.; Noh, J. H.; Mandal, T. N.; Lim, C. S.; Chang, J. A.; Lee, Y. H.; Kim, H. J.; Sarkar, A.; Nazeeruddin, M. K.; Grätzel, M.; Seok, S. I. Efficient inorganic-organic hybrid heterojunction solar cells containing perovskite compound and polymeric hole conductors. *Nature Photon.* 2013, 7, 486-491.

220. Burschka, J.; Pellet, N.; Moon, S. J.; Humphry-Baker, R.; Gao, P.; Nazeeruddin, M. K.; Grätzel, M. Sequential deposition as a route to high-performance perovskite-sensitized solar cells. *Nature* 2013, 499, 316-319.
221. Bi, D.; Moon, S.-J.; Haggman, L.; Boschloo, G.; Yang, L.; Johansson, E. M. J.; Nazeeruddin, M. K.; Gratzel, M.; Hagfeldt, A. Using a two-step deposition technique to prepare perovskite (CH₃NH₃PbI₃) for thin film solar cells based on ZrO₂ and TiO₂ mesostructures. *RSC Adv* 2013, 3, 18762-18766.
222. Bi, D.; Yang, L.; Boschloo, G.; Hagfeldt, A.; Johansson, E. M. J. Effect of Different Hole Transport Materials on Recombination in CH₃NH₃PbI₃ Perovskite-Sensitized Mesoscopic Solar Cells. *J. Phys. Chem. Lett.* 2013, 4, 1532-1536.
223. Edri, E.; Kirmayer, S.; Cahen, D.; Hodes, G. High Open-Circuit Voltage Solar Cells Based on Organic-Inorganic Lead Bromide Perovskite. *J. Phys. Chem. Lett.* 2013, 4, 897-902.

Acknowledgement

First of all I would like to thank god for what he has done. Since very beginning of my degree in UNIST, I have received many help from other, and I could successfully finished my Ph.D. course.

All of my research project would not be possible without the support of many people. Foremost among them, I would like to sincerely thank my advisor, Prof. Yongseok Jun to give me encouragement and compliment. Moreover, his guidance and patience during the course enabled me to be a Ph.D.

I also thankful to my committee members, Prof. Jin Young Kim, Prof. Sung You Hong, Prof. Tae-Hyuk Kwon, and Dr. Dongsuk Kim, who deserve my deepest gratefulness for their help and support in providing professional discussions.

I would like to express gratefulness to all the members of SOLARINNO, Yimhyun Jo, Cho-long Jung, Suresh Kannan B, Minoh Lee, Jae young Park, Seong young Kong, Woo-yeol Choi, and Yohan Ko. Also Dr. Yong Ju Yun, NGEL team members and our alumni, Heejin, Hyun-A, and Jeonghun deserve my gratitude.

Finally, I wish to express my love and gratitude to my beloved parents and family; for their understanding and love, through the duration of my degree. Without help from everyone, I couldn't have completed my Ph. D degree successfully.

I sincerely thank everyone once again.

감사의 글

먼저 무사히 박사학위를 마칠 수 있게 이끌어 주신 하나님께 감사를 드립니다.

학위 시작을 위해 채 완공되지도 않은 학교에 설레어 하며 들어섰었는데, 이제 그 시간들의 끝에 다가와 있습니다. 지난 5년간의 학위 과정 중에 있었던 많은 일들이 스쳐 지나갑니다. 그 동안 무수한 도움과 힘을 준 모든 분들께 짧게나마 이 지면을 빌어 감사인사를 드리고자 합니다.

먼저 박사과정 동안 부족한 저를 이끌어 주시고, 바쁘신 중에도 항상 시간 내어 제자의 이야기에 귀 기울여 주시며 때로는 엄하게, 때로는 어질게 지도 해 주신 전용석 교수님께 깊은 감사의 인사를 드리고 싶습니다. 그리고 박사 학위 심사를 하면서 아낌없는 조언과 지도로 지지해 주신 홍성유 교수님, 김진영 교수님, 권태혁 교수님, 김동석 박사님께도 감사의 말씀을 전합니다.

박사과정 동안 여러 가지 면에서 동고동락 했던 UNIST 및 건국대학교의 모든 연구실 분들께도 감사의 인사를 전합니다. 쉴 새 없는 긴장감을 안겨주는 임현이형, 도도한 초롱이, 유토피아맨 민오, 순둥이 Suresh, 조용하고 강한 우열이, 좌충우돌 성영이, 목소리 큰 요한이, 재영이 형, 또 많은 가르침을 주신 윤용주 박사님과 우리 졸업생들 희진이, 정훈이형, 현아까지. 모두들 너무 감사합니다. 앞으로도 서로 잘 이끌어 주고 당겨줘서 Solarinno 를 빛내 주시기 바랍니다. 같은 오피스 에서 함께 생활 했던 NGEL 멤버들, 한 집에서 같이 살림을 살았던 태희와 동우, 힘들고 스트레스 받을 때 잠시나마 같이 일탈을 할 수 있었던 보람이형과 서진이 형, 또 다른 모든 UNIST 및 건국대 친구들 모두모두 감사 드립니다.

마지막으로 아들이 어떤 선택을 하든, 어떤 결정을 하든 그저 믿고 응원해 주시며 뒤에서 든든히 지켜 봐 주신 세상에 하나뿐인 아버지와 어머니, 안락한 숙식을 제공해 준 형과 형수님께 거듭 감사의 말씀을 전합니다. 가족의 지원과 사랑이 있었기에 이 자리까지 올 수 있었습니다. 또 지난 5년간 한결같이 옆에서 변함없는 응원을 보내 준 그녀에게도 감사의 말을 전합니다. 앞으로 어느 곳에 나아가셔도 가족들에게, 선후배에게 부끄러움 보이지 않는 박사가 되도록 노력 하겠습니다.

다시 한번 모든 분들께 감사 드립니다.